



# This is to certify that the

#### thesis entitled

Texture Evolution During High Rate Superplastic Elongation In Mechanically Alloyed Aluminum

presented by Jin, Zhe

has been accepted towards fulfillment of the requirements for

M.S. degree in Materials Science

Major professor

Date 8-4-91

**O**-7639

MSU is an Affirmative Action/Equal Opportunity Institution

# LIBRARY Michigan State University

PLACE IN RETURN BOX to remove this checkout from your record. TO AVOID FINES return on or before date due.

TO AVOID FINES return on or before date due.			
DATE DUE	DATE DUE	DATE DUE	
061			

MSU Is An Affirmative Action/Equal Opportunity Institution
ctclrctdstedue.pm3-p.1

# TEXTURE EVOLUTION DURING HIGH RATE SUPERPLASTIC ELONGATION IN MECHANICALLY ALLOYED ALUMINUM

Ву

Zhe Jin

# A THESIS

Submitted to
Michigan State University
in partial fulfillment of the requirements
for the degree of

MASTER OF SCIENCE

Department of Metallurgy, Mechanics and Materials Science

#### ABSTRACT

TEXTURE EVOLUTION DURING HIGH RATE SUPERPLASTIC
ELONGATION IN MECHANICALLY ALLOYED ALUMINUM

By

Zhe Jin

Texture analysis as a structure parameter is a very powerful analytical tool for studying deformation behavior due to its capability of isolating the individual contributions from the various mechanisms, such as dislocation slip, twinning, grain boundary sliding, grain rotation, and recrystallization. The texture evolution in the superplastically deformed specimens of IN90211 is investigated as a function of strain using the three dimensional crystal orientation distribution functions (CODFs). At the lower strain rates (1/sec and 77/sec), the textures are mainly concentrated along two fibres,  $\alpha$ -fibre (<101> parallel to ND) and  $\{102\}$ <uvw> (<102> parallel to ND). At the higher strain rate (330/sec), the textures are mainly composed of two fibres, {203}<uvw> and a skeleton line (<001> orientation is tilted from ND towards TD by about 30°). The results indicate that at small strains the specimen deforms by grain boundary sliding and single slip, at large strain the deformation is dominated by grain boundray sliding, multiple slip and recrystallization. However, at the highest strain rate, there is no evidence of recrystallization.

Copyright by

Zhe Jin

1991

#### ACKNOWLEDGEMENTS

The author would like to express his sincere appreciation to his advisor, Professor Tom Bieler for his continuous guidance and support during this work. The author enjoyed the time closely working with him.

The author very grateful for the financial support from Michigan State University through an All-University Research Initiation Grant.

# TABLE OF CONTENTS

F	age
ABSTRACT	ii
LIST OF FIGURES	viii
LIST OF TABLES	xiii
CHAPTER 1. TEXTURE AND SUPERPLASTICITY	1
1.1. Deformation Texture	1
1.1.1. Slip	2
1.1.2. Stacking Fault Energy	10
1.1.3. Mechanical Twinning	10
1.1.4. Micro-Banding	16
1.1.5. Shear-Banding	17
1.2. Recrystallization Texture	19
1.2.1. Oriented Growth	20
1.2.2. Oriented Nucleation	23
1.2.3. Nucleation Sites	25
a. Nucleation in Grain Interiors	25
b. Nucleation at Grain Boundaries	27
c. Transition Bands	28
d. Influences of Particles	29
1.2.4. {100}<001> Cube Tuxture	31
1.3. Grain Growth	32
1 4 Superplasticity	31

		Page
	1.4.1. Concept of Superplasticity	34
	1.4.2. Mechanical Behavior of Superplasticity	37
	1.4.3. Microstructural Behavior of Superplasticity.	41
	1.4.4. Mechanisms of Superplastic Deformation	51
	a. GBS with Diffusion Accommodation	51
	b. GBS with Dislocation Motion Accommodation.	55
	c. Dislocation Slip	59
1.5.	Relationship Between Texture and Superplastic	
	Deformation	59
	1.5.1. Texture Effects on Superplasticity	59
	1.5.2. Superplastic Deformation Effects on	
	Texture	65
1.6.	Representation of An Orientation	67
	1.6.1. Introduction to Rotation System	68
	a. Euler Angles	68
	b. Rotation Axis and Angle	70
	1.6.2. Representation of the Orientation	70
	a. Representation of the Orientation in the Po	ole
	Figure	70
	b. Representation of the Orientation in the	
	Inverse Pole Figure	71
	c. Representation by Miller Indcies	73
	d. Matrix Representation	73
	e. Orientation Distribution Function	74
	f. Relationship Between Euler Angles and Mille	r
	Indices	76

	Page
CHAPTER 2. EXPERIMENTAL PROCEDURES	81
CHAPTER 3. RESULTS	83
3.1. Specimen Deformed at $\dot{\epsilon}=1/\text{sec}$ and T=425°C	83
3.2. Specimen Deformed at $\dot{\epsilon}=77/\text{sec}$ and $T=475^{\circ}\text{C}$	93
3.3. Specimen Deformed at $\epsilon$ =330/sec and T=475°C	100
CHAPTER 4. ANALYSIS AND DISCUSSION	107
4.1. Deformation at Relative Low Strain Rate	107
4.1.1. Grain Boundary Sliding	107
4.1.2. Slip	110
4.1.3. Recrystallization	112
4.2. Deformation at High Strain Rate	113
CHAPTER 5. CONCLUSIONS	115
APPENDIX A POLE FIGURES OF IN90211	116
APPENDIX B INVERSE POLE FIGURES OF IN90211	133
LIST OF REFERENCES	149

# LIST OF FIGURES

Figure Number		Page
Fig.1.1	Stereographic projections showing deviation of an effective stress axis Te from the actual stress axis Ta. (a) Shear stress contours. (b) Lines of maximum descent from the point of maximum resolved shear stress F	. 2
Fig.1.2	Lattice rotations for {111}<110> slip. (a) The smallest allowed shear (within the confines of minimum work) is maximized. (b) The largest allowed shear is maximized. (After Bishop )	. 6
Fig.1.3	Texture rotations predicted by Bishop for (a) copper and (b) 70/30 brass	. 7
Fig.1.4	Computer-plotted lattice rotations obtained for {111}<110> slip in which the activities of colinear pairs have been maximized within the confines of minimum work.  (Axisymmetric tension 5% strain)	. 9
Fig.1.5	Hard-sphere model of [011] slip via [121] (leading) and [112] (trailing) partials.  (a) The partials are unextended. (b) The partials are extended	. 9
Fig.1.6	Computer-plotted lattice rotations for {111}<112> intrinsic foulting, according to minimum work criterion. (Axisymmetric tension 5% strain)	. 11
Fig.1.7	Orientation factors for $\{111\}<110>$ slip (full lines) and $\{111\}<112>$ twinning (dashed lines) under rolling (assuming a plane stress state) and relative twin orientation factor $\mu$ (dashed dotted line). (a) Along the $\alpha$ fibre, <110> parallel ND. (b) Along the $\beta$ fibre, <110> tilted 60° from NT towards RD. (c) Along the $\tau$ fibre, <110> parallel TD	. 13
Fig.1.8	Orientation paths due to mechanical twinning of $\{112\}<111>$ and subsequent deformation presented in the $\phi_2=45^\circ$ section of the Euler space	. 15
	or the parer shace	. 10

Figure Number		Page
Fig.1.9	Schematic representation of nucleation sequence of recrystallized grains during annealing of cold rolled steel	. 26
Fig.1.10	Variation of some important texture components during typical box-annealing cycle	. 27
Fig.1.11	The strain rate dependence of (a) the flow stress and the strain rate sensitivity for the Mg-Al alloy, grain size 10.6 $\mu$ m deformed at 350°C	. 37
Fig.1.12	Strain rate sensitivity versus strain rate for Sn-5%Bi samples of varying Sn grain size	. 39
Fig.1.13	The dependence of the strain-rate sensitivity index on strain rate at different temperatures for aluminium-copper eutectic specimens	. 39
Fig.1.14	Microstructure of Sn-5%Bi alloy strained 1000% at room temperiture. (a) Cross section. (b) Longitudinal section, tensile as vertical	
Fig.1.15	Changes in surface appearance of same area in specimen with increasing strain at $\dot{\epsilon}=6.7 \times 10^{-3}  \text{min}^{-1}$ in vacuum 2x10 mmHg. Deformed (a) 9%, (b) 35%, (c) 64%, (d) 96%	. 44
Fig.1.16	The value of the vertical component of the grain boundary sliding versus boundary angle with the tensile axis. (a) $\dot{\epsilon}=1.6 \times 10^{-4}$ sec (region I), (b) $\dot{\epsilon}=8.3 \times 10^{-1}$ sec (region II), (c) $\dot{\epsilon}=4.1 \times 10^{-1}$ sec (region III).	. 45
Fig.1.17	Appearence of internal marker line translations in specimens deformed at $\dot{\epsilon}=6.7 \times 10^{-3}$ min Deformed (a) 30%, (b) 60%, (c) 100%, (d) 200%	. 47
Fig.1.18	Relative frequency of rotation of internal marker lines to stress axis in specimens deformed 60%. (a) At $\epsilon_A = 2 \times 10^{-3} \text{min}^{-1}$ , (b) $\epsilon_B = 6.7 \times 10^{-3} \text{min}^{-1}$ , (c) at $\epsilon_C = 1.1 \times 10^{-1} \text{min}^{-1}$	. 48

Figure Nu	mber F	age
Fig.1.19	Relative frequency of rotation of internal marker lines to stress axis in specimens deformed at $\dot{\epsilon}=6.7 \times 10^{-3}$ min . (a) Deformed 30%, (b) deformed 60%, (c) deformed 100%, (d) deformed 200%	48
Fig.1.20	Densities of dislocations in twin boundaries as a function of strain for regions I-III	50
Fig.1.21	The unit step of the deformation process	52
Fig.1.22	The accommodation strains required when grains move from the initial to the intermediate states	53
Fig.1.23	The trajectories of grain centers in the emulsion, where a switching event has occured	55
Fig.1.24	GBS and its accommodation to give deformation in region II of superplasticity	56
Fig.1.25	Slip accommodation of grain boundary sliding	57
Fig.1.26	Slip accommodation from grain boundary ledges	58
Fig.1.27	Variation of m with strain rate and with direction of straining	60
Fig.1.28	Elongation at fracture as a function of angle of the tensile axis to the rolling direction at three strain rates for aluminum-bronze sheet tested at 800°C	61
Fig.1.29	Elongation as a function of strain rate	63
Fig.1.30	True stress / true strain curves on extention with $\dot{\epsilon}$ =2.8x10 sec at 250°C for different states of the alloy	63
Fig.1.31	Strain rate sensitivity as a function of strain rate (a) at 250°C, (b) at 150°C.  1. Quenching, rolling at 250°C, annealing at 350°C for 5h, water quenching. 2. Quenching, 96.6% rolling at 20°C, annealing at 350°C for 5h, quenching. 3. Quenching, 96.6% rolling at 20%. 4. Quenching, rolling to 96.6% at 250°C	64

Figure Number		Page
Fig.1.32	The sample fixed coordinate system Kand the crystal fixed coordinate system KB in the sheet	68
Fig.1.33	Definition of the Euler angles ${\varphi_1}^{\phi {\varphi_2}} \dots$	69
Fig.1.34	On the definition of the Euler angles $\Psi  heta \Phi \dots \dots$	69
Fig.1.35	Representation of a rotation by the rotation axis d and the appropriate rotation angle $\omega$	71
Fig.1.36	The orientation of some crystal directions in pole figures	72
Fig.1.37	The orientation of the specimen directions in inverse pole figure	72
Fig.1.38	Relationships between the angles $\varphi_1, \phi, \varphi_2$ and $\psi, \theta, \phi$	80
Fig.3.1	Some ideal components in $\Phi=0^{\circ}$ section	83
Fig.3.2	Complete CODF of $\hat{\epsilon}=1$ sec <sup>-1</sup> and T=425°C (a)-(f)	85
Fig.3.3	The $\phi$ =0° section of CODF vs. strain	91
Fig.3.4	Orientation density vs. $\Psi$ and strain	93
Fig.3.5	Complete CODF of $\dot{\epsilon}$ =77 sec <sup>-1</sup> and T=475°C (a)-(b)	94
Fig.3.6	Orientation density vs. $\Psi$ and strain	101
Fig.3.7	Complete CODF of $\dot{\epsilon}$ =330 sec <sup>-1</sup> and T=475°C (a)-(b)	102
Fig.3.8	Orientation density vs. $\Psi$ and strain	106
Fig.4.1	Texture components vs. true strain	108
Fig.4.2	Schematic diagram showing sliding of platelet-shaped grains during superplastic elongation	108
Fig.A.1	(111),(200),(220) pole figures of specimen deformed at $\dot{\epsilon}=1/\text{sec}$ and $T=425^{\circ}\text{C}$	117
Fig.A.2	(111),(200),(220) pole figures of specimen deformed at $\dot{\epsilon}=77/\text{sec}$ and $T=475^{\circ}\text{C}$	123

# LIST OF TABLES

Table	Numb	per I	Page
Table		Contribution of grain boundary sliding to the total axial strain $(\epsilon_{gb}/\epsilon_{t})$ in regions I, II and III	46
Table	2.2	Composition (wt%) of IN90211	81

#### CHAPTER 1

#### TEXTURE AND SUPERPLASTICITY

Texture is defined simply as a condition in which the distribution of crystals is nonrandom, that is, the orientations of all the grains in a polycrystalline aggregate tend to cluster, to a greater or lesser degree, about some particular orientations, or an aggregate has a preferred orientation. Like crystal structure and lattice defects, texture is also a fundamental parameter characterizing polycrystalline materials. It links the anisotropic properties of single crystals and those of the polycrystalline materials.

The formation of texture can be classified into four parts: deformation texture, recrystallization texture, cast texture and transformation texture. In the following sections, we will discuss the deformation texture and recrystallization texture only.

#### 1.1. Deformation Texture

Deformation texture is produced by forming processes, such as wire drawing, sheet rolling and torsion. It is due to the tendency of the grains in a polycrystalline

aggregate to rotate during plastic deformation. Each grain undergoes slip and rotation in a complex way that is determined by the imposed stress and by the slip and rotation of adjoining grains. The result is a preferred, nonrandom orientation.

# 1.1.1. Slip

It is well known that the deformation textures are developed as a result of lattice rotation brought on by crystallographic shear during plastic deformation. When an unconstrained crystal is loaded with an applied stress  $T_a$ , the effective stress axis  $T_e$  on the crystal will move away from the initial applied stress  $T_a$  by crystal slip. In the unit triangle of a stereographic projection of crystal,  $T_e$  moves towards the boundary of the unit triangle under the single slip system, see Fig.1.1; when duplex slip

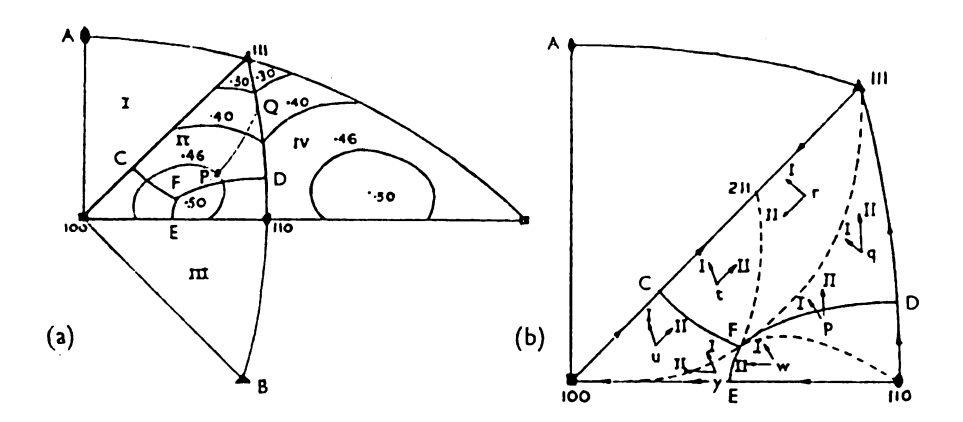


Fig.1.1 Stereographic projections showing deviation of an effective stress axis Te from the actual stress axis Ta. (a) Shear stress contours. (b) Lines of maximum descent from the point of maximum resolved shear stress F.

system is operative, T<sub>e</sub> lies on a boundary of the unit triangle; when four, six and eight slip systems operate, Te lies at <110>,<111> and <100> directions respectively, because the Schmid factor is equal among all equivalent systems.

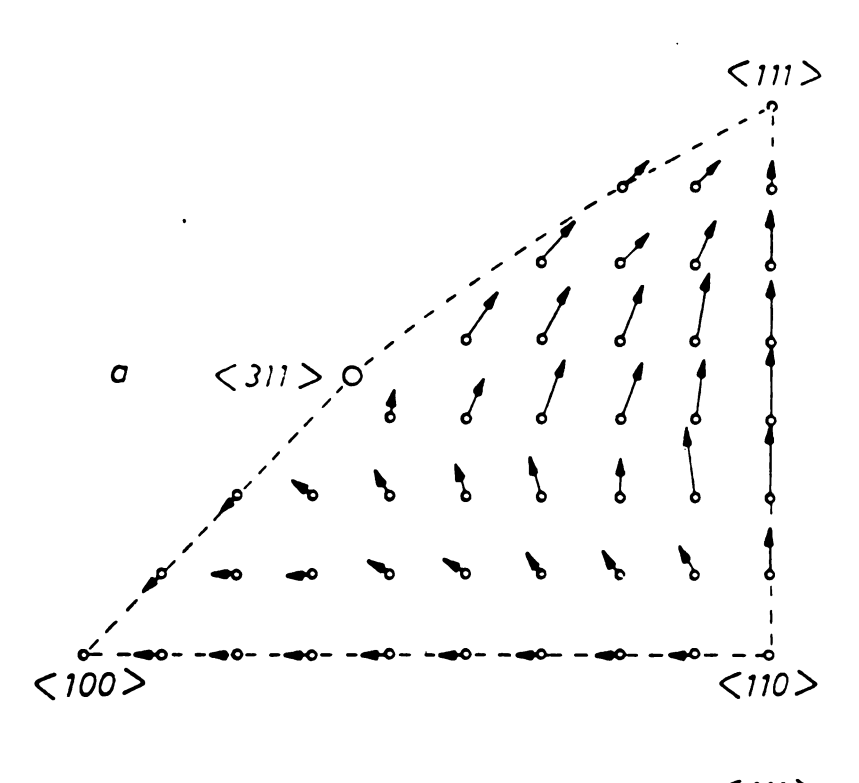
In polycrystalline materials, most of the grains will be unable to deform by single slip or change their shape freely because of constraints from each other. If applied stress Ta is at P in Fig.1 , a slip should occur when Ta=Tc/cosχcosλ, where Tc is critical resolved shear stress, cosxcos\(\lambda\) is Schmid factor. But the build up of constraints causes Te to move from Ta by moving down the line of maximum rate of change of cosχcosλ towards Q. Upon reaching Q, Te is equal on two slip systems, but two systems are insufficient to allow deformation in a polycrystalline aggregate and Te axis will continue to rotate along the symmetry boundary to <111>. At the point <111>, the value of resolved shear stress is a minimum and any increase in Ta will cause the grain to yield by slipping on six equally favoured slip systems. For other initial orientation of Ta, Te will rotate to <110> if Ta is within the region II or to <100> if Ta is in III .

In the orientations <100>,<110> and <111>, there is a multiplicity of slip systems available and since all slip systems are symmetrically disposed, no rotation of the

grain relative to Ta occurs and consequently there would be no development of preferred orientation. So the texture arises from single or duplex slip rotations of grains. In tension, Slip rotation cause grain to rotate so that the movement of Te axis is towards the operative slip direction and a texture with <112>,<111> and <100> directions is parallel to tensile axis. In compression, Ta axis moves towards the slip plane normal and a <110>,<100> texture occurs. In rolling, the texture is constituted with the orientations which satisfy mutually the requirements of a tensile stress parallel to the rolling direction and a compressive stress parallel to the sheet normal, that is,the orientations with the spread from {110}<112> to {311}<112> as well as {110}<111> and {110}<001> [2].

According to the theory of Taylor<sup>[5]</sup>, the slip in a grain embedded in a polycrystalline aggregate requires at least five independent slip systems in order to accommodate five independent strains. Taylor assumed that among all combinations of (five) slip systems which are capable of satisfying the imposed strain, the active combination is the one for which the sum of the glide shears is a minimum. Bihop and Hill<sup>[4]</sup> strengthened Taylor's theory by showing that the shear stress reaches the critical level for slip on the active slip systems chosen by Taylor without exceeding it on the inactive slip systems. This theory provides strain continuity across grain boundaries by

assuming that each grain deforms in the same way as the aggregate, that is, although deformation is known to be macroscopically and microscopically inhomogeous, it is sufficient for a statistical problem such as texture development to assume homogeneous deformation. From Bishop and Hill's principle of maximum work [4] , the stress system required to impose the arbitrary strain can be found and hence the slip systems can be determined. There are only five stress systems which give rise to polyslip in single crystals and these crystals give either six or eight available slip systems, so that either one or three are redundant in each grain. The choice of the five systems from six or from eight depends on whether or not the material exhibits "overshoot". According to Bishop's theory, metals which exhibit an alloy texture have overshoot and those having the pure metal texture don't show overshoot. The overshoot is due to the hardening of the latent slip system being greater than that of the active system. When there is latent hardening, the most extensively operated system will harden least and hence the situation is represented by maximizing the largest shear. But if the hardening of the latent slip system (latent hardening) equals the hardening of the active slip system (active hardening), then the combination is chosen such that the smallest glide shear is as large as possible [12.13]. Fig.1.2 shows these two cases under a



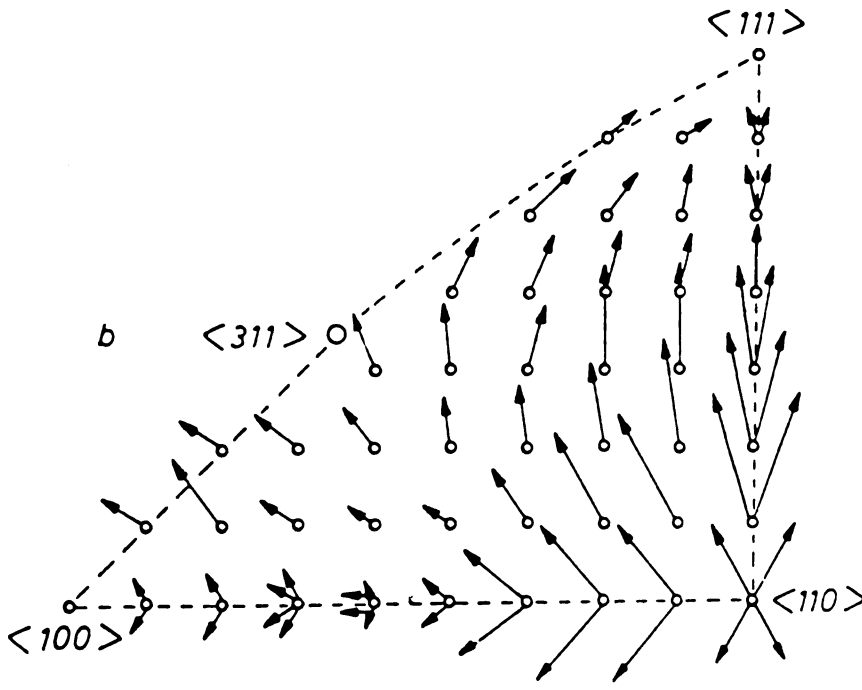


Fig.1.2 Lattice rotaions for {111}<110> slip. (a) The smallest allowed shear (within the confines of minimum work) is maximized. (b) The largest allowed shear is maximized. (After Bishop

tension applied stress. In Fig.2a, both <111> and <100> are stable for a metal where latent and active hardenings are equal; but in Fig. 2b, the <100> texture is unstable and rotates towards <111> orientation if latent hardening is larger than active hardening. The rotations for compression are the reverse of those for tension. In the case that latent and active hardenings are equal, a <110> texture will spread towards <113> (Fig.1.3a); If latent hardening is larger than active hardenings, the

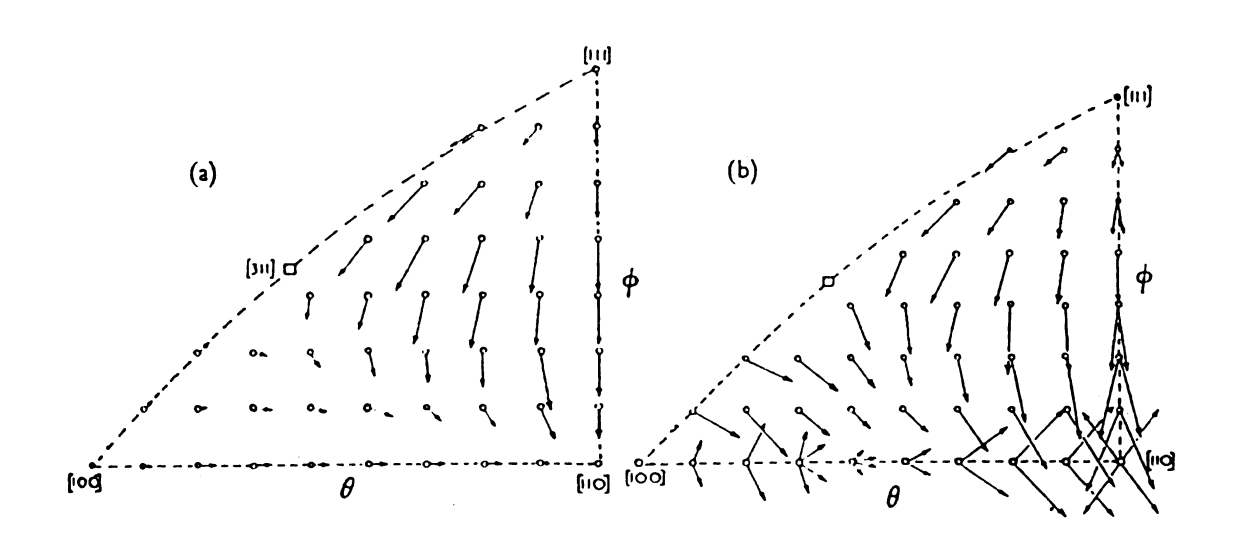


Fig.1.3 Texture rotations predicted by Bishop for (a) copper and (b) 70/30 brass.

rotation is more directly towards <110> (Fig.1.3b) [12]. The experiments done by Ramaswami [14] and Kocks [15] have shown that prior slip on one system hardens all other systems more than itself except a coplanar system where the hardening is about equal. So there is a tendency for

hardening on non-coplanar systems to increase with decreasing stacking fault energy of metals. Comparing Fig.2 with Fig.1 shows latent hardening (coplanar slip) mechanism also favors an increase of the <111> texture.

But latent hardening mechanism can not explain the phenomenon that silver (pure metal) has a alloy type texture even though Smallman<sup>[7]</sup> suggested that trace of dissolved oxygen was responsible for the alloy behaviour. Calnan and Smallman later rejected this theory.

cross-slip usually occurs in high stacking fault energy materials and at high deformation temperature [9,10,11]. This mechanism implies that for the multiple slip situation in constrained deformation, all {111} <110> slip system pairs that share a common slip direction (colinear slip) are favored. At large applied stress, it is also possible that the materials undergo cross-slip, but a low stacking fault energy material still chooses other slip combinations wherever they are available. Fig.1.4 shows the predicted rotations based on cross-slip mechanism. As compared with Fig.1, it may be seen that those crystals within the previous region II are biased toward the <111>, thus partially accounting for the drop in the <100> component for high stacking fault energy metals.

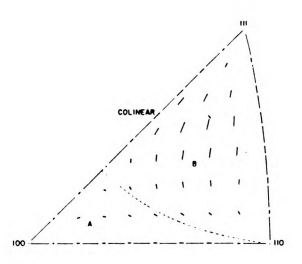


Fig.1.4 Computer-plotted lattice rotations obtained for (111)<110> slip in which the activities of colinear pairs have been maximized within the confines of minimum work. (Axisymmetric tension 5% strain)

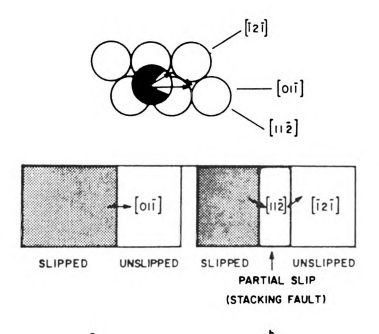


Fig.1.5 Hard-sphere model of  $[01\overline{1}]$  slip via  $[\overline{1}2\overline{1}]$  (leading) and  $[11\overline{2}]$  (trailing) partials. (a) The partials are unextended. (b) The partials are extended.

### 1.1.2. Stacking Fault Energy

For materials of low stacking fault energy, a {111}<110> dislocation is normally split into two shockly partial dislocations of the {111}<112> type connected by a ribbon of stacking fault. Usually, the separated partial dislocations move in zigzags. Two steps of slip of separated partial dislocations are equal to one step of normal dislocation, i.e.,  $[12\overline{1}]+[11\overline{2}]=[01\overline{1}]$ , see Fig.1.5. However, if the partial dislocations are widely separated, the effective slip direction of partial dislocation is. shifted from <110> to <112>, that is, the leading partial dislocation, [121], in Fig.1.5, moves ahead creating a strip of intrinsic faulting, while the trailing partial dislocation, [112], is pinned behind. The slip movement would then be equivalent to (111)[121] in which case the lattice rotation and hence the texture development would be altered from the usual (111)<110> slip pattern. The rotation by this mechanism is shown in Fig.1.6 for tension stress. <100> component is no longer stable and intrinsic faulting favors a strong <111> wire texture for very low stacking fault energy materials.

#### 1.1.3. Mechanical Twinning

Since the orientation of a twin differs drastically from that of the matrix, the mechanical twinning is

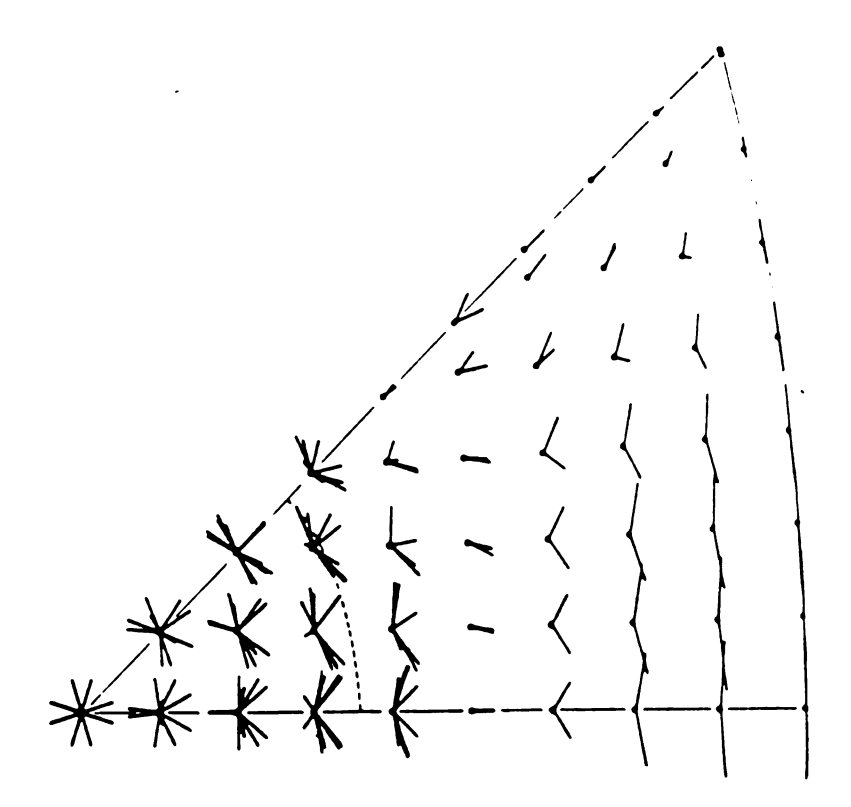


Fig.1.6 Computer-plotted lattice rotations for {111}<112> intrinsic foulting, according to minimum work criterion. (Axisymmetric tension 5% strain)

expected to play an important role in the development of deformation texture. The {111}<112> will be formed if the motion of the partial dislocation generates a stacking fault on successive {111} layers.

According to the analysis of Chin, Hosford and Mendorf [16], the incremental work done by a stress  $\sigma_{\rm X}$  causing a strain  $\epsilon_{\rm XX}$  is equal to

$$W = \sigma_{\mathbf{x}} \varepsilon_{\mathbf{x}\mathbf{x}} = \tau_{\mathbf{s}} \mathbf{i} \Sigma S_{\mathbf{i}} + \varepsilon_{\mathbf{t}} \mathbf{i} \Sigma T_{\mathbf{i}}$$
 (1.1)

where  $\tau_s$  is critical resolved shear stress of slip,  $\tau_t$  is critical resolved shear stress of twinning,  $S_i$  and  $t_i$  are the corresponding shear. The orientation factor M then

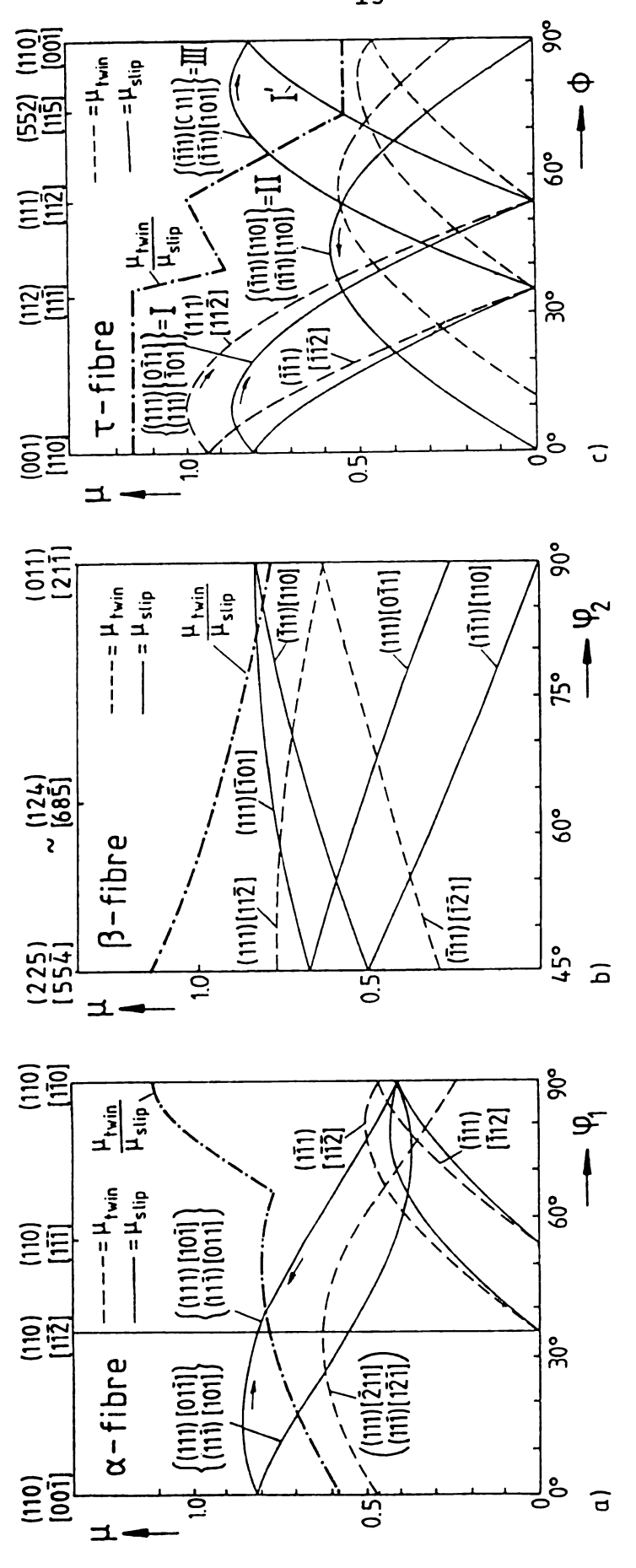
becomes

$$\mathbf{M} = \frac{\sigma_{\mathbf{X}}}{\tau_{\mathbf{S}}} = \frac{1}{\epsilon_{\mathbf{X}\mathbf{X}}} (\Sigma \epsilon_{\mathbf{i}} + \alpha \Sigma t_{\mathbf{i}})$$

where  $\alpha = \tau_{\rm t}/\tau_{\rm s}$ . The operative combination of slip and twin systems is formed if M is minimum. For {111}<110> slip and {111}<112> twinning, mixed slip and twinning can only occur for  $1/\sqrt{3} < \alpha < 2/\sqrt{3}$ ; if  $\alpha > 2/\sqrt{3}$ , only slip is possible; if  $\alpha < 1/\sqrt{3}$ , only twinning happens.

For the plane stress state, mechanical twinning happens if relative twin orientation factor  $\mu$  =  $\mu_{\text{t}}$  /  $\mu_{\text{s}}$ , (where  $\mu_{\text{t}}$ is the Schmid factor for {111}<112> twinning and  $\mu_{c}$  is the Schmid factor for {111}<110> slip), is larger than one [20]. In the case of  $\mu \ge 1$ , the {112}<111> copper orientation undergoes mechanical twinning during rolling to form the {255}<511> twinning copper orientation. Fig.1.7 shows the values of  $\boldsymbol{\mu}_{\text{t}}$  ,  $\boldsymbol{\mu}_{\text{s}}$  and  $\boldsymbol{\mu}$  for the relevant twin and slip systems along the  $\alpha$  ,  $\beta$  and  $\tau$  fibers of cold rolled copper. It can be seen that the tendency for twinning decreases steadily along the  $\beta$  fiber from copper component to brass component and  $\mu$  < 1 along the  $\alpha$ -fiber. This means that the part of  $\beta$ -fiber near copper orientation should twin more easily but for the  $\alpha$ -fiber orientations no twinning should occur. It also can be seen in Fig. 1.7a that two kinds of slip systems, i.e., colinear slip system  $(\bar{1}11)[110]-(\bar{1}\bar{1}1)[110]$  and coplanar slip system  $(111)[\bar{1}01]-$ 



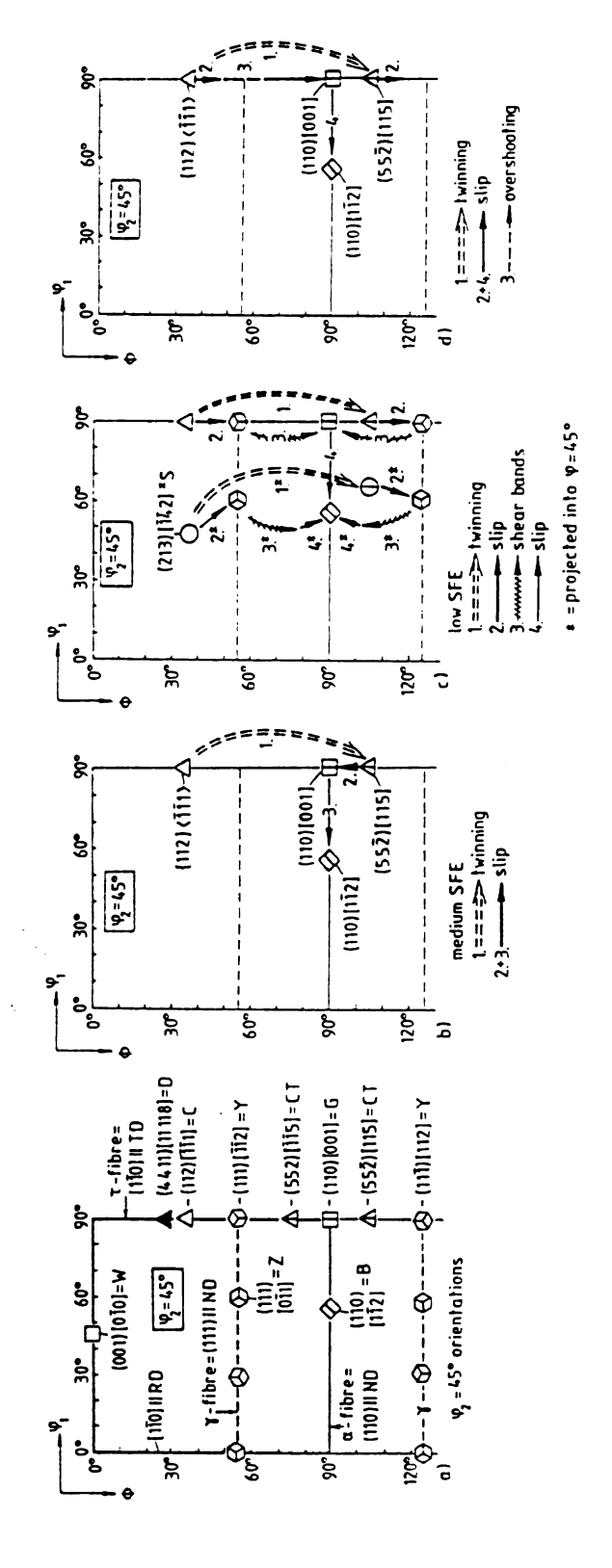


(dashed dotted line). (a) Along the <110> parallel to ND; (b) along the  $\beta$  fibre, <110> tilted 60 twinning (dashed lines) under rolling (assuming a plane stress) and (111)<110> slip (full lines) and (111)<112> along the r fibre, <110> parallel to TD. relative twin orientation factor  $\mu$ Fig.1.7 Orientation factors for from NT towards RD; (c) α fibre,

(111)[011] occur along  $\alpha$ -fiber. Coplanar slip rotates the orientation towards larger  $\Phi$  angle while colinear slip causes a rotation towards smaller  $\Phi$ . So at the position of copper component (112)[111], the two rotations cancel each other and the cooper orientation is stable.

Twinning explains not only the decrease in copper component but also the increase of G and B components. The orientation path of twinning is the one which the texture transition from the copper-type rolling texture with dominant C and S orientation to the brass-type rolling texture where B and G predominate, as shown in Fig.1.8b.

Fig.1.8 schemeticslly shows orientation paths due to mechanical twinning of {112}<111> and subsequent deformation presented in the  $\varphi_2$  = 45° section of the Euler space.(a) is principle orientation occurring in the  $\varphi_2$ =45° section (extended to  $\varphi$  > 90°). (b) is mechanical twinning (1) and subsequent normal slip (2,3). (c) is mechanical twinning (1), subsequent abnormal slip (2), shear band formation (3) and normal slip (4). (The corresponding orientation changes of the S orientation {123}<412> (1\* to 4\*) are projected into the  $\varphi_2$  = 45° section.) (d) is mechanical twinning (1) with subsequent abnormal slip (2), overshooting the matrix orientation C by preferred coplanar slip (3) and normal slip (4). Mechanical twinning increases with increasing strain and decreasing stacking fault energy.



section of the Euler Fig.1.8 Orientation paths due to mechanical twinning of (112)<111> and subsequent deformation presented in the  $arphi_2^{}=45$ space (a)-(d).

# 1.1.4. Micro-Banding

Deformation of polycrystalline materials is usually inhomogeneous, occurring by deformation banding as a common phenomena. There are two kinds of deformation banding. Type one results from the operation of a different allowable combination of slip systems in each of several portions of a grain. Most of deformation bands are formed in this way. Type two is formed if the work done by slip within the bands is less than that for homogeneous deformation and if the bands can be arranged such that the net strain practically matches that for the overall deformation [19].

The mechanism of formation of deformation band is that edge dislocations in the primary slip system of opposite signs accumulate in two parallel subgrain walls, so rotating the inner part in the opposite direction with respect to the matrix<sup>[22]</sup>. These kinds of bands are geometrically necessary to compensate for incompatible strain effects. Therefore, the parts of a grain finally rotate into a different stable orientation to compensate the incompatible strain in polycrystalline deformation. The mechanism of deformation banding is the same as that of kink band in tensile strain of single crystal.

The formation of microbands is also related to dislocation glide on {111} slip plane. The locally

concentrated dislocation gliding and the dislocation channeling on one active slip system cause the microbands, orientations of which coincide with {111} planes<sup>[23]</sup>. After their formation, they are still affected by the normal slip processes and are finally rotated parallel to the sheet plane without producing further misorientations. The microbands can be seen at low and medium strain. Because the orientation difference between microbands and matrix is very small (2°)<sup>[23,24]</sup>, they would not notably change the orientation distribution.

# 1.1.5. Shear-Banding

At low to moderate levels of strain (generally  $\epsilon < 1.0$ ) and at normal strain rates, the materials deform by slip or twinning which is related to the crystallography of the component grains. At somewhat higher strain levels, instabilities develop and shear bands form. Shear bands cross grain boundaries without deviation and the planes in the shear bands are related to the specimen geometry and the deformation process rather than to the crystallography of the deforming material [25]. Shear bands develop with a non-crystallographic geometry when normal crystallogaphic slip is strongly inhibited. The bundles of microbands in medium SFE materials and packages of twin/matrix lamellae, for example, can inhibit the normal crystallographic slip.

Depending on the size of the bands, shear bands are classified into two kinds: grain-scale shear band (microscopic shear band) which extends through one or a few grains and sample-scale shear band (macroscopic shear band) which extends through the entire specimen<sup>[26]</sup>. The grain-scale shear bands can develop only if there is a certain freedom for the local strain to be heterogeneous. They are inclined at angles of 23° and 37° to the rolling direction preferentially. When grain-scale shear bands at these angles encompass larger and larger regions, they are organized into sample-scale shear bands and the inclined angle of 45°<sup>[27]</sup>. The sample-scale shear bands play an important role in the texture softening which offers new slip orientations for further deformation<sup>[28]</sup>.

Clifton and co-workers<sup>[29]</sup> proposed a thermoplastic instability mechanism of shear band formation. They suggested that non-uniform heating caused by non-uniform straining and different heat generation caused by different strain rate make deformation become more non-uniform, thus the shear band may develop.

According to the microstructures of shear bands, two kinds of shear bands, copper-type shear band and brass-type shear band, are defined<sup>[21]</sup>. There are small orientation differences ( < 10°) between orientations inside the copper type shear band and the surrounding matrix<sup>[30]</sup>. For

example, In the C and B grains, the reported shear band angles of 20°, 35° and 30°(5°) correspond almost exactly to shear deformation of {111}<112>, {001}<110> and {112}<110>[30]. So copper-type shear bands have little influence on rolling texture development. Also, the volume fraction of the bands is too small to give rise to a separate texture component. But copper-type shear bands can explain the presence and reappearance of G orientation at high deformation since the bands often contain G orientation<sup>[21]</sup>. During rotation of the twin/matrix lamellae by preferred slip on the coplanar slip systems and I' in Fig.7c, the Schmid factor  $\mu$  for the hindered slip systems II and III and the force exerted by the piled-up dislocations continue to increase. This results in a highly unstable structure with strong geometrical softening effects so that the brass-type shear bands with extremely large shear strains (  $\varepsilon$  up to 10) become possible [25]. The orientation changes due to the shear banding are indicated in Fig.1.8c as stages 3 and 4 or 3\* and 4\*.

# 1.2. Recrystallization Texture

There are two main mechanisms to explain the development of primary recrystallization texture: the oriented growth mechanism and the oriented nucleation mechanism. The oriented growth mechanism assumes that the

nuclei are considered as parts of the deformed matrix but nuclei of many orientations are available. Their growth rate into the matrix depends on their orientation with respect to the matrix and the texture is finally determined by the grains with largest growth rates [31.32]. The oriented nucleation mechanism assumes that the recrystallization textures are only determined by the orientation of nuclei and the oriented growth does not play any role at all [33-35].

#### 1.2.1. Oriented Growth

The oriented growth theory is based on the strong dependence of growth rate of recrystallization nucleus on the orientation relationship between the deformed matrix and the growing grain. So it is assumed in this theory that the recrystallization texture is determined by nuclei oriented in such a way that they grow particularly fast. In this case, the ratio of a fast growth rate of specially oriented grains to the growth rate of randomly oriented grains should be larger than one. That is, this is a grain boundary property not a grain property [36]. For fcc metals, low interface energies occur at 0° and 60° rotations around <111>; high energies occur at intermediate rotations [43,44]. Thus the maximum growth rate orientation is determined as about 40° <111> rotation [37-41]. But this relationship is not exactly obeyed for all materials of fcc. For example,

copper and silver show 30° <111> rotations and aluminum-manganese alloys containing 0.5%Mn show 84° <112> rotations due to the occurrence of annealing twins in these metals<sup>[42]</sup>. For polycrystalline fcc materials, recrystallization occurs at an approximate 40° <111> relationships between the components of recrystallization texture and one or several components of rolling texture<sup>[2]</sup>.

 ${\tt Beck}^{[31,45,46]}$  explained that the development of cube orientation followed the oriented growth mechanism. The formation of the cube texture in a rolled sheet is available if the recrystallized grains at an early stage of the annealing process reach a size at which they come into effective contact with several (or all four) principal orientations of the deformation texture (e.g. {124}<211>). Since these grains of the cube texture orientation are related to each of these four deformation texture components by a <111> rotation suited to high boundary mobility, they can grow faster than any grains with other orientations, and can grow into all four of these components. Some other orientations also have this relationship: the R-orientation has such a relationship to 3 components of the rolling texture, G-orientation to all 4 components and the rotated cube orietation ({001}<110>) to all 4 components [47].

At the higher annealing temperatures, grain growth, because of its importance, will often dominate the texture change. It is possible that different texture components recrystallize at different temperatures, thus, an annealing texture may be a mixture of several components, because individual crystals may have wide differences of recrystallization tendency after a given amount of deformation [48-51].

Microbands or transition bands are also important in this mechanism when the boundary of one of these microbands migrates or when adjacent microbands coalesce in a way that develops high angle and highly mobile boundaries. Crystals that have a sharp, single orientation deformation texture tend to recover rather than recrystallize, and therefore retain their deformation texture at least until they are consumed by differently oriented grains. A low annealing temperature favors retention of the cold-rolled texture [52].

The driving forces for grain boundary movement usually come from the reduction of strain energy in the region swept over by a boundary and a reduction of boundary energy from a reduction in boundary area and from a reduction in energy per unit area.

Grain growth theory has its shortcomings. It can only partially explain the details of recrystallization

texture development. It can't explain that grains in orientations deviating from the maximum of the grain boundary energy by about 15° still grow at relativaly high rates<sup>[32]</sup>, and that there are certain variants of the growth relationships<sup>[53]</sup>, and also that the scatter orientations in slightly deformed single crystals are not related to the matrix orientation in any simple manner<sup>[32]</sup>.

#### 1.2.2. Oriented Nucleation

In this theory, the nucleation process is the important factor in determining the range of available nuclei which can contribute to the recrystallization texture. There are three mechanisms of formation of recrystallion nuclei.

The first one is that nuclei are considered as a part of the deformed matrix and subgrain growth [53-56]. there are three sub-mechanisms which are proposed by Dillamore and Katoh: (i) Nuclei are formed by subgrain growth in the regions of uniform orientation, i.e., it occurs when a subgrain grows until one side meets a pre-existing grain boundary. Recrystallization will then occur if the free length of grain boundary is long enough to bow out under the driving force provided by the energy stored on the other side of the boundary. This is formed within the stable deformation components. (ii) Nuclei are formed in the region of sharp lattice curvature, i.e., in

orientations where a strong divergence of orientation occurs upon further deformation and which lie near the edges of the deformation texture. The example of this mechanism is transition band nucleation, which requires low thermal activation but needs increasing thermal energy as the boundary angle increases. (iii) Nuclei are formed at grain boundaries by migration of existing high angle interfaces. It can also occur at grain edges and grain corners. Grain boundary nuclei usually have orientations either in the main stable texture components or in the principal range of spread about these components.

The second is that nuclei are considered as recrystallization twins formed at the early stages of recrystallization or even during deformation. It is possible for low stacking fault energy fcc materials.

Investigation of Peters<sup>[57.58]</sup> on Cu-Sn shows that texture (326)[634] is oriented to the deformed matrix (011)[211] by a 40°<111> rotation in this mechanism.

The third mechanism is that nuclei are formed by an inverse Rowland-transformation of the deformed matrix<sup>[54]</sup> or by this transformation followed by further twinning.

The <111> fiber texture in recrystallized rolled steel sheet is predicted by oriented nucleation theory. Deformed

grains with <111> normal to the rolling plane are found to have higher stored energy than other oriented grains. Thus new grains with <111> orientations nucleate first during annealing and grow into other <111> region by rotations about the fiber axis.

#### 1.2.3. Nucleation Sites

There are several sites available for nucleations, such as grain interiors, grain boundaries, transition bands, interfaces between second phase and matrix and twins. In the following, the nucleations at these sites will be discussed.

(a) Nucleation in Grain Interiors. It is commonly observed at moderate and high deformations, since at low strains the lattice curvature is seldom sufficient to allow a high angle boundary to be created. The distribution of stored energy depends on orientation in the deformed materials. Within the major texture components of bcc metals, the stored energy increases in the order {011}<011>,{100}<011>,{211}<011>,{111}<uvw>[59,60]. The sequence of increasing stored energy corresponds to that of increasing Taylor M value or corresponds to the total amount of dislocation motion that has taken place. The ease of nucleation within grains would be correspondingly orientation sensitive. Fig.1.9 schematically shows this

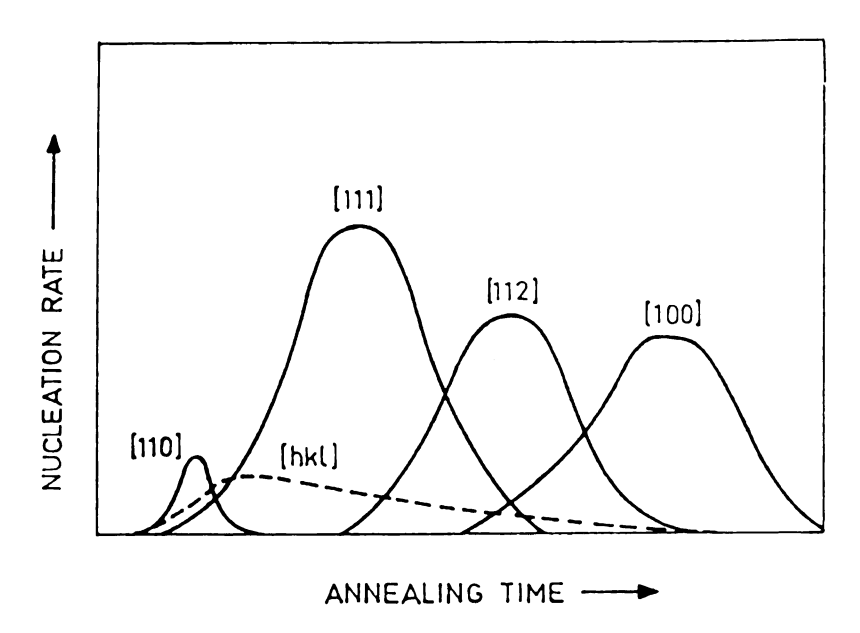


Fig.1.9 Schematic representation of nucleation sequence of recrystallized grains during annealing of cold rooled steel.

relationship based on the stored energy consideration [61]. so the final texture should be dominated by nuclei which form soonest and which are most numerous. During the annealing, the (011) and (111) texture components should nucleate first and therefore have the longest available time for growth before impingement occurs. The least favoured orientation (100) is predicted to disappear on annealing due to its consumption by the growth of other grains, like (110) and (111) grains, which is shown in Fig.1.10. The (111) oriented grains have the best orientation with matrix to grow and therefore increase the (111) texture component [62]. A fine initial grain size increases the orientation sensitivity and therefore the (111) texture component by increasing the homogeneity of strain during rolling and so maximizing the stored energy

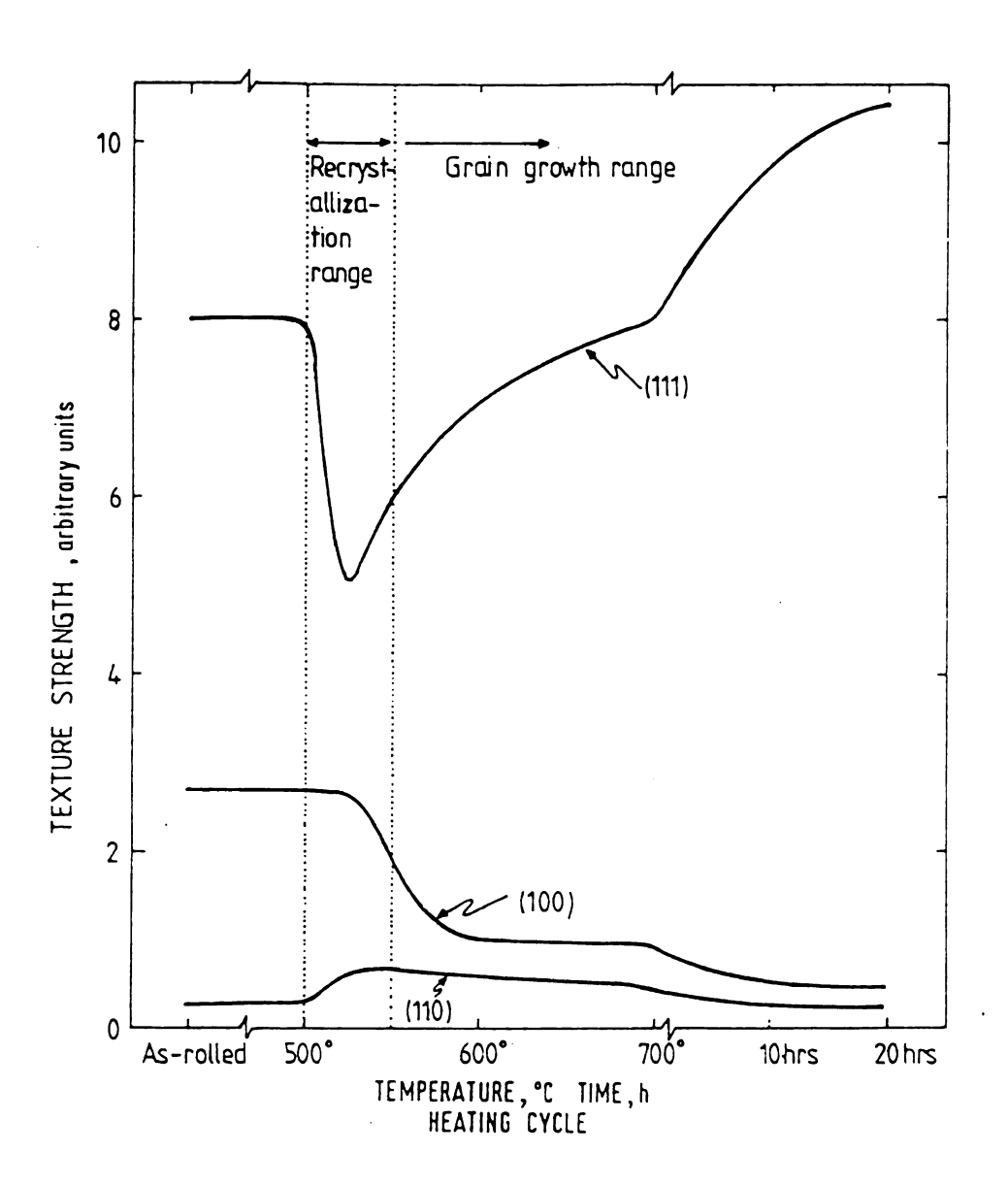


Fig.1.10 Variation of some important texture components during typical box-annealing cycle.

differences between orientations.

(b) Nucleation at Grain Boundaries. This occurs in two ways: One is by the existing boundary bowing out into the grain which has the higher stored energy at the boundary. The other is by growth of a subgrain close to that grain

boundary. In both cases, the orientation of nucleation is close to the orientation of matrix near the boundaries in which they form. Orientations near the grain boundaries often rotate away from the grain center, so the nucleation at grain boundaries introduces recrystallization texture components that have orientations close to, but not at, the deformation texture components [63]. The proportion of nucleations at grain boundaries is much higher than that for intra-granular nucleations.

(c) Nucleation at Transition Bands (Microbands). Transition bands are composed of closely spaced subboundaries which manifest cumulative misorientations. Nucleation at transition bands is possible because of their high stored energy and rapid change of orientation which allows a high angle boundary to be easily formed [64,65]. Because the orientations of the new grains may differ widely from those of deformation texture, notable changes in orientation may occur during annealing. But it is important in development of recrystallization textures only when the subsequent growth rates of new grains are relatively high, since the number of transition band sites which are much favoured is quite small compared to intragranular or grain boundary sites. Thus a small number of nuclei must grow into a very large volume. The most favoured orientations for nucleations at transition bands for bcc metals are in order of {110}<001>, {100}<011> and

- {11,11,8}<4,4,11>(near {111}<112>). But different transition bands will be most favoured for nucleation after different strains and they may cease to be viable after heavy deformation [65]. The cube orientation(100)<001> of fcc metals is also predicted to arise by this mechanism [35]. The operation of different combinations of slip systems in different regions within one grain may give rise to different crystal rotations. In general, at low or moderate strains, almost any orientations of transition bands may occur, but at high strains, the separate blocks or deformation bands converge on a common final orientation. So nucleations at transition bands may contribute to the weak or nearly random recrystallization textures after low defrmation [66].
- (d) Influence of Particles. Influences of particles on recrystallization depend on the size and distribution of the particles. In general, widely spaced coarse particles enhance nucleation and the rate of recrystallization if particles are present before deformation<sup>[67]</sup>, while finely dispersed particles normally reduce recrystallization kinetics, having a greater retarding influence on nucleation than on growth<sup>[68]</sup>. The change in texture is usually accompanied by an increase of the as-recrystallized grain size<sup>[68]</sup>. The texture changes in the metal which has finely dispersed particles can be rationalized on the basis of the oriented nucleation mechanism. If nucleation of all

orientation components is retarded in equal proportions, then the time available for growth of the first formed grains is increased. The recrystallization texture will therefore show increased selectivity and will become even more strongly biased towards the most favoured orientation nuclei. In the case of steel, the precipitates of AlN, NbC and Cu lead to considerable strengthening of the {111} texture components at the expense of those components near {100}<sup>[69,70]</sup>. Finely dispersed particles may also interact with certain types of nucleation sites. In steel, AlN may be effective in strengthening {111} textures and act to suppress the {110} sheet-plane textures, particularly the Goss component (110)<001>. This indicates that nucleation within transition bands may be especially susceptible to interference by finely dispersed particles. Precipitation of Al<sub>2</sub>Fe in pre-existing grain boundaries inhibits growth of the early formed cube nuclei thereby forcing nucleation in the abundant rolling texture components. Hornbogen et al<sup>[71-73]</sup> reported for aluminium-copper alloys and copperbased and nickel based alloys that discontinuous (conventional) recrystallization gives rise to normal recrystallization textures, such as the cube textures, while continuous (or in situ) recrystallization causes retention of the rolling texture.

In addition to the oriented nucleation and oriented growth, the formation of annealing twins play an essential

role for recrystallization texture formation because only this mechanism creates all new orientations relative to the deformed structure. In general, twins occur in materials with low stacking fault energy. In this paper, we will not discuss it further.

### 1.2.4. {100}<001> Cube Texture

As an example of recrystallization texture, cube texture {100}<001> is often found in recrystallized fcc metals and alloys. cube textures are more often formed under the condition of heavy deformation and a fine starting grain size, and may also be considerably strenthened during grain growth after the completion of primary recrystallization.

The cube texture arises because it has favoured orientation relationship to the deformed structure for the rapid growth of recrystallized grains. The orientations of the most mobile grain boundaries are the misorientations of 30°-40° around a common <111> pole<sup>[74,75]</sup>. On the basis that rolling texture, which gives rise to the cube component, is near {123}<412>, it is possible to explain the origin of this component in terms of oriented growth theory, since only {100}<001> bears the necessary orientation relationship with all four equivalent {123}<412> components. In the aluminum alloys and copper

with an initial coarse grain size, the cube texture coexists with a retained rolling texture, which is near {123}<412>. This orientation is possibly consumed by growing cube grains [76]. When enlarged subgrains or small recrystallized grains are present in the unannealed deformed structure of 95% deformed copper, these are almost invariantly of the cube orientation. These cube grains are found to grow rapidly at low annealing temperatures before any other recrystallized grains appear [77].

### 1.3. Grain Growth

It is very important to mention that grain growth plays an important role in texture development after completion of primary recrystallization. Upon completion of primary recrystallization, there is usually a rather diffuse spread of orientations together with the recrystallization texture components, which are often not very strong. During grain growth, these components are strengthened at the expense of the diffuse spread of orientations, and sometimes there is a redistribution of density between different components. This type of texture sharpening is known for the cube texture in aluminum, copper and nickel<sup>[78]</sup>, while the Goss component and the (111) sheet plane orientations are enhanced in steel. During grain growth, large grains grow at the expense of small ones<sup>[79,80]</sup>. If the grain size distribution for grains of a particular texture component

is biased to larger size than the average distribution, then these grains will prosper during the grain growth and their texture will be correspondingly strengthened. If there are sufficient number of second phase particles, they may provide a constant reaction to the migration of grain boundaries, and may cause transition from normal to abnormal grain growth, and amplify the texture changes occuring during grain growth [80]. A limiting case is secondary recrystallization, where a very small fraction of grains grow intensively and thus very sharp textures may be created.

# 1.4. Superplasticity

# 1.4.1. Concept of Superplasticity

Superplasticity is defined as the ability of a material to undergo unusually extensive plastic deformation at high temperature. There are two necessary prerequisites for superplasticity: one is a deformation temperature greater than half the absolute melting temperature, so that diffusional processes occur rapidly, and the other is a small stable equiaxed grain size, usually less than 10  $\mu$ m. The characteristic microstructure feature of superplastic deformation is the retention of equiaxed grain structure throughout deformation.

In broad outline, superplasticity may be divided into two parts, i.e., structural superplasticity and environmental superplasticity. For structural superplasticity, a characteristic structural condition, e.g., a stable ultra-fine grain size, is required and the strain rate sensitivity m (=  $\partial \log \sigma$  /  $\partial \log \varepsilon$ ) is the order of 0.3 to 0.8. In environmental superplasticity, the special testing conditions are necessary, e.g., temperature cycling under a small applied stress and the value of m is equal to about one. In both parts of superplasticity, the applied stress for superplastic deformation is markedly dependent on the strain rate. this dependence is generally

evaluated in terms of the strain rate sensitivity index m in the relationship<sup>[82]</sup>

$$\sigma = K\dot{\epsilon}^{m} \tag{1.3}$$

where  $\sigma$  is the applied stress,  $\dot{\epsilon}$  is the strain rate and K is a constant for given testing conditions, m and K are both dependent on test parameters such as temperature and grain size. For Newtonian-viscous materials, m is equal to one and the elongation in tension is uniform and independent of irregularities in cross section. For superplastic materials, m is usually in the range of 0.3 to 0.85 because resistance to necking can be predicted from continuum mechanics for m greater than about 0.3.

At the temperature below 0.4  $T_{\rm m}$  ( $T_{\rm m}$  is melting point of material), the material being deformed obeys a true stresstrue strain law of the type<sup>[83]</sup>

$$\sigma = C\varepsilon^{n} \tag{1.4}$$

where C is the strength coefficient and n is the strain hardening exponent. The true strain at which plastic instability (necking) occurs can be shown as

$$\epsilon_{\text{necking}} = n$$
 (1.5)

and n usually lies within the range of 0.1 to 0.3.

At high temperature, the rate of strain hardening decreases and extensive plastic deformation occurs without necking which is due to an enhanced strain rate sensitivity<sup>[84.85]</sup>. So when both strain-hardening and strain-rate effects need to be considered, the following flow stress law is assumed to be obeyed<sup>[86-88]</sup>,

$$\sigma = K' \varepsilon^n \dot{\varepsilon}^m \tag{1.6}$$

where K' is a constant embracing C and K. If the condition of  $n/(\epsilon+m) > 1$  is satisfied, the deformation is stable. This criterion is in agreement with those for strain hardening materials and for viscous materials which are resistant to necking for  $m=1^{\left[89\right]}$ .

Environmental superplasticity usually occurs under well defined environmental conditions [90-93], such as (a) during temperature cycling through a phase change, (b) during temperature cycling of a thermally anisotropic material, and (c) during neutron irradiation. Thus this phenomenon is generally observed when a small stress is applied in conjunction with the above conditions. Because the environmental superplastic behavior is observed only in very small number of materials, it is not discussed further here.

# 1.4.2. Mechanical Behavior of Structural Superplasticity

Most superplastic materials exhibit a sigmoidal relationship between the logarithms of stress and strain rate (see Fig.1.11) [94]. The region of maximum strain rate

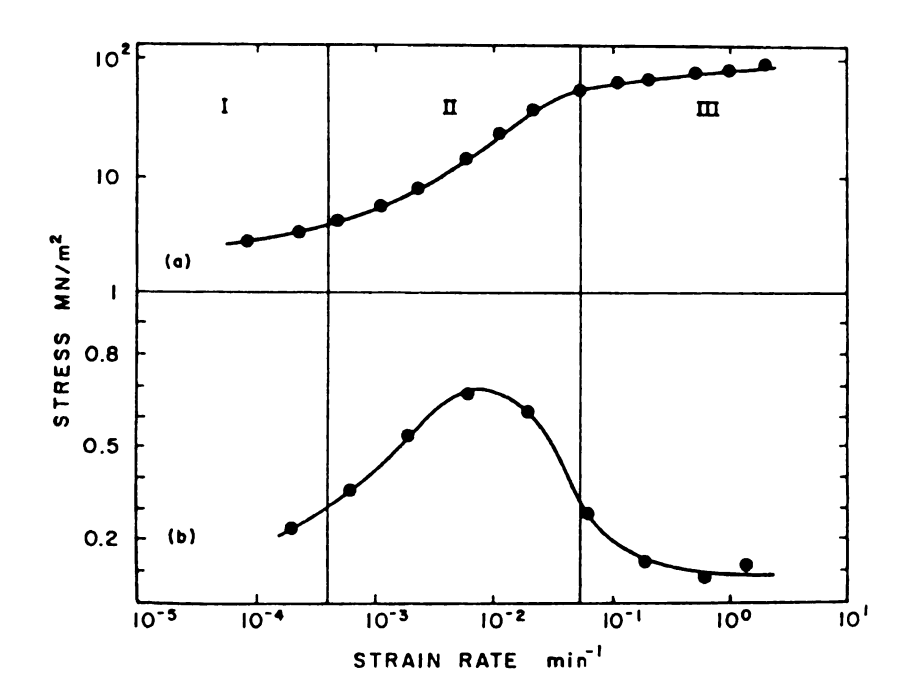


Fig.1.11 The strain rate dependence of (a) the flow stress and the strain rate sensitivity for the Mg-Al alloy, grain size 10.6  $\mu$ m deformed at 350 C

sensitivity (region II) with slope m>0.3 delineates the strain rate range over which the superplasticity occurs. Both the low and high regions of strain rate (region I and III) exhibit values of m<0.3 and correspond to conventional plasticity. However, it must be emphasized that the sigmoidal shape is by no means universal. Some authers reported that they could find no evidence of

sigmoidal shape in the lower strain rate range(region I) of the  $\log \sigma$  vs.  $\log \varepsilon$  curve<sup>[95-98]</sup>. The sigmoidal shape in superplastic deformation is often thought to result from a threshold stress<sup>[99-104]</sup>. But several authors reported that they could not find evidence for a threshold stress in superplastic deformation<sup>[95,105,106]</sup>. The possible mechanism of formation of threshold stress will be discussed in a later section.

In general, the resistance to neck formation during superplastic deformation is ascribed to a high value of  $m^{[86,107]}$ . For large values of m, the strain rate of materials near a neck and that in the rest of the specimen are nearly equal. This minimizes the tendency for localized necking and premature failure and therefore leads to large overall total elongation. In this case, theoretically stable flow is possible provided m>1/2 for constant velocity testing and m>1/3 for constant strain rate testing. So for creep deformation, the stress dependence of strain rate in  $\varepsilon=A^n$ , where n is inverse of m, should not exceed 2 or 3 for stable flow to occur.

The strain rate sensitivity m increases with a decrease in grain size in regions II and I, and the transition between regions II and III is shifted to higher strain rates. This is shown in Fig.1.12 [108]. The strain rate corresponding to a given flow stress and temperature has been shown to vary with grain size L as

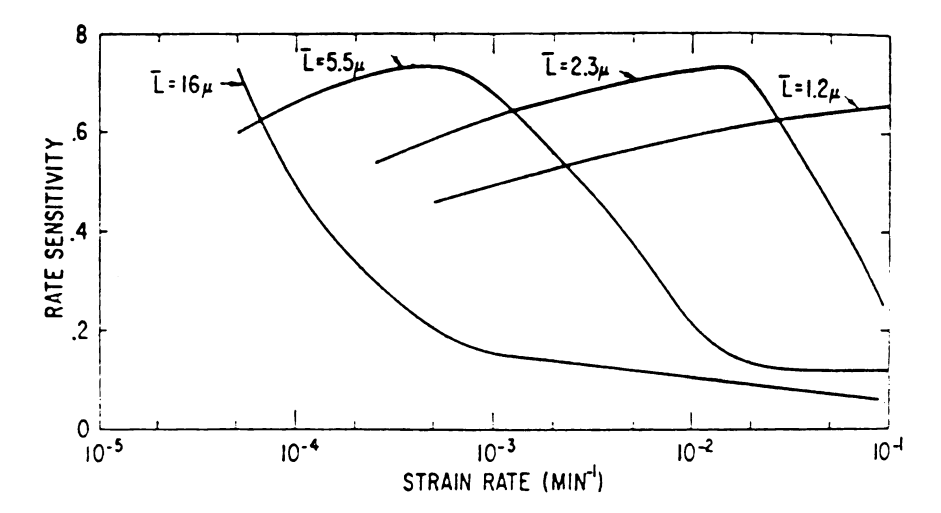


Fig.1.12 Strain rate sensitivity versus strain rate for Sn-5%Bi samples of varying Sn grain size

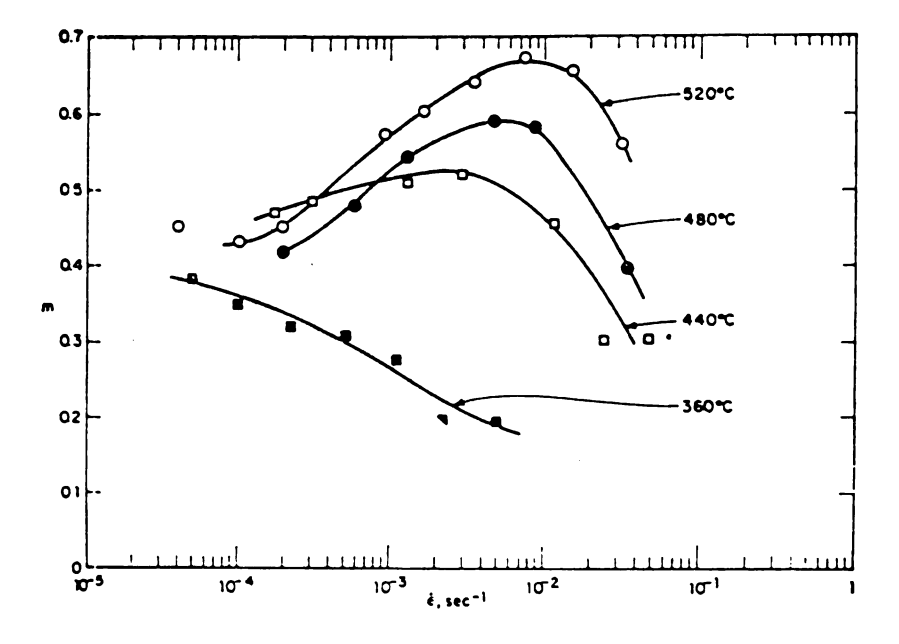


Fig.1.13 The dependence of strain rate sensitivity index on strain rate at different temperatures for aluminium-copper eutectic specimens

$$\dot{\varepsilon} \propto \frac{1}{L_a} \tag{1.7}$$

where the exponent a generally lies within 2 and 3<sup>[108-113]</sup>. The dependence of flow stress on grain size at constant strain rate and temperature follows the relation of

$$\sigma \propto L^{b}$$
 (1.8)

where b lies in the range 0.7 to  $1.2^{[110,112,114-116]}$ .

The temperature effects on superplastic deformation are shown in Fig.1.13<sup>[112]</sup>, which shows that m increases with increasing temperature. Increasing deformation temperature reduces the overall level of the flow stress and displaces the transitions between regions I and II and between regions II and III to higher strain rates (see Fig.1.14). There are two categories for activation energies of deformation in region II: one is activation energies similar to those for grain boundary diffusion [106,117] and the other is activation energies comparable to those for lattice diffusion<sup>[118]</sup>. The activation energies for region III usually correspond to those for dislocation creep [96,105,117,119,120]. There are also two categories in region I: activation energy in this region is equal to that for volume diffusion [105,117] and activation energy equals that for grain boundary diffusion [96]. The relationship

between strain rate (  $\dot{\epsilon}$  ) and activation energy (Q) is expressed as

$$\dot{\epsilon}_{\sigma L} \propto \exp(-Q/kT)$$
 (1.9)

where k is Boltzmanns constant. It is therefore apparent that diffusional processes are of considerable importance in superplastic deformation. And this point of view is further reinforced by Morrison's observation that alloying elements which increased atomic mobility also enhanced superplastic behavior<sup>[121]</sup>. The effects discussed above on strain rate may, therefore, be combined into one relation equation as

$$\dot{\epsilon} = A \frac{\sigma^{n}}{\tau^{a}} \exp(-Q/kT)$$
 (1.10)

where A=constant, n=1/m.

# 1.4.3 Microstructural Behavior of Superplasticity

It has been shown that the grain structure remains essentially equiaxed with little growth during deformation under optimal conditions. Fig.1.14 shows that the Sn-5% Bi alloy has an equiaxed shape even after 1000% elongation<sup>[122]</sup>. Fig.1.14a is cross section and Fig.1.14b a longitudinal section. Grain deformation usually occurs near the grain boundaries and grain boundaries become

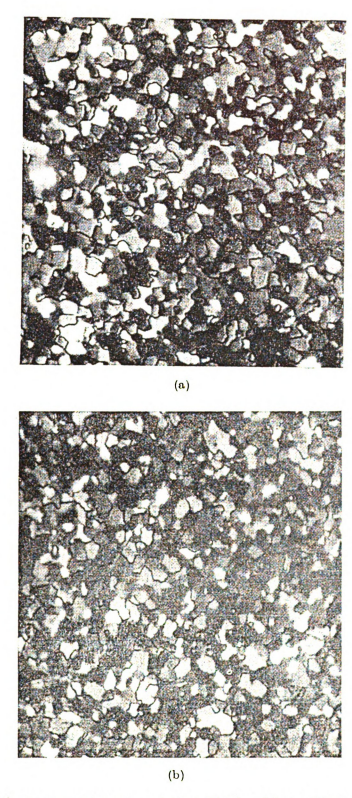


Fig.1.14 Microstructures of Sn-5%Bi alloy strained 1000% at room temperature. (a) Cross section.

(b) Longitudinal section, tensile axis vertical.

curved after deformation. But grain shape still remains equiaxed and grains do not elongate in the direction of tensile axis during superplastic deformation.

Grain boundary sliding (GBS) is commonly observed during superplastic deformation. Two initially adjacent grains may end up many grain diameters apart. (see Fig.1.15). The relative motion of two initially adjacent grains depends on the resolved shear stress across the grain boundary and grains with transverse or longitudinal boundaries generally moving apart less rapidly than other oriented grains during superplastic flow. Fig.1.16 shows a GBS dependence of the angle between the axis of the applied stress and the orientation of sliding boundary. The sliding mainly occurs at the transverse boundaries in region I but in regions II and III the main sliding is at the boundary which lies at 45° to the applied stress axis. GBS occurs at the onset of plastic flow. Small apparent gaps develop between surface grains at low strains due to sliding. After some amount of strain, new grains begin to emerge to the surface from the interior to fill the gaps. This process continues throughout the strain range. Most surface grains present at large strains are initially located in the specimen interior. The contribution of GBS is a maximum in region II and decreases at higher (region III) and lower (region I) strain rates, which can be seen in Table 1.1.

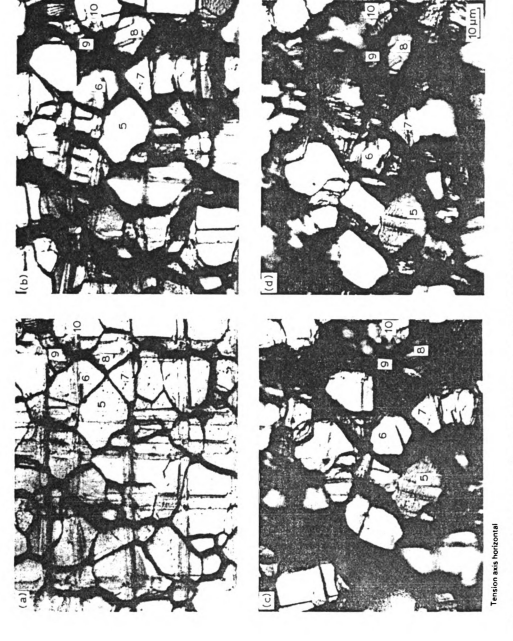


Fig.1.15 Changes in surface appearance of same area in specimen, with increasing strain at i= 7.7x10 min in vacuum 2x10 mmHg. Deformed (a) 9%, (b) 35%, (c) 64%, (d) 96%.

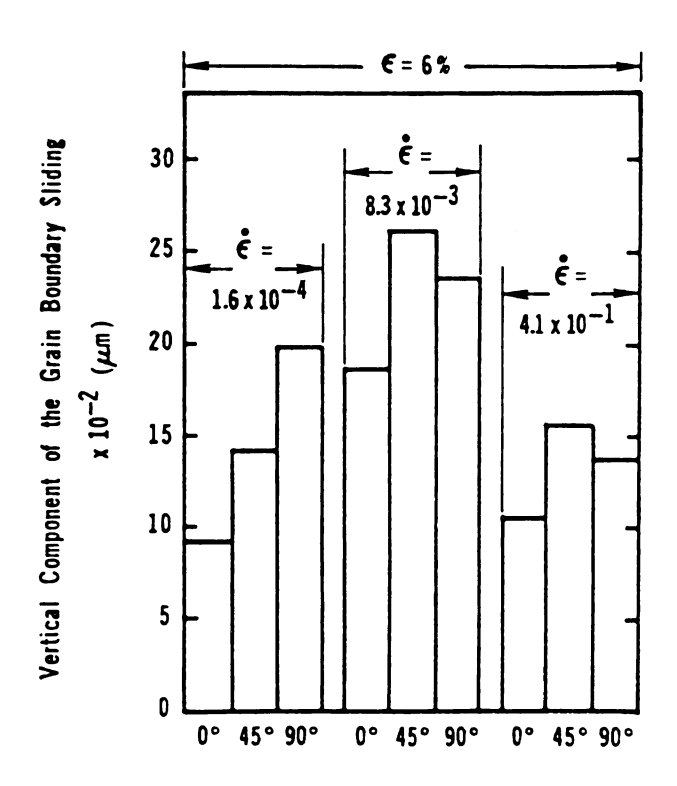


Fig.1.16 The value of the vertical component of the grain boundary sliding versus boundary angle with the tensile axis. (a)  $i=1.6\times10^{-4}$  sec (region I), (b)  $i=8.3\times10^{-3}$  sec (region II), (c)  $i=4.1\times10^{-1}$  sec (region III).

Individual grain rotations are often observed during superplastic flow. In Fig.1.17, it is apparent that the internal marker lines are tilted with superplastic strain. The amount of grain rotation during superplastic deformation as a function of strain rate and strain are shown in Fig.1.18 and Fig.1.19 respectively [123]. The rotations higher than 35° are only at the lowest strain rate ( $\dot{\epsilon}_{\rm A}$ ) and the intermediate degree of rotation of 5 to 25° are greatest at the intermediate strain rate ( $\dot{\epsilon}_{\rm B}$ )

Table 1.1 Contribution of grain boundary sliding to the total axial strain  $(\epsilon_{\rm gb}/\epsilon_{\rm t})$  in regions I, II and III

Material		<sup>¢</sup> gb/ <sup>¢</sup> t (%)	
	Region I	Region II	Region III
AMg6 Alloy	05~	0,2	~ 40
Al-33%Cu eutectic		~70	
Al-9%Zn-1%Mg	42	63	26
Al-11%Zn-1%Mg	09~	08~	250
MA8	250	~75	~ 50
Mg-33%Al eutectic	12	64	29
Mg-1.5%Mn-0.3%C	33	41-49	30
Pb-Tl		50	33.
Pb-Sn eutectic	21	56	20
Zn-0.4%Al	42	48	28
Zn-Al eutectoid	30	09~	30

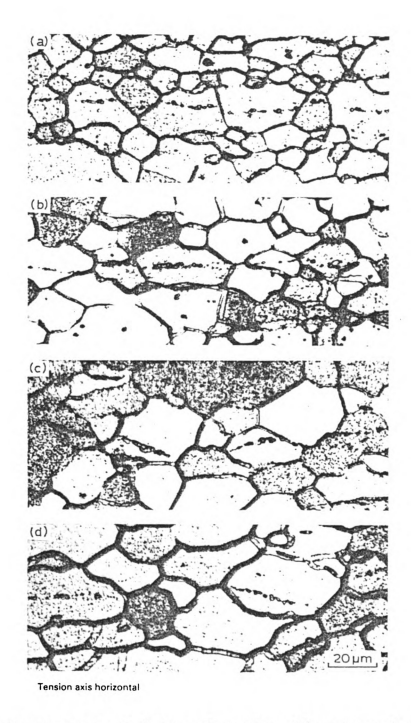


Fig.1.17 Appearence of internal marker line translations in specimens deformed at  $\dot{\epsilon}=6.7\times10^{-3}\,\mathrm{min}^{-1}$ . Deformed (a) 30%, (b) 60%, (c) 100%, (d) 200%.

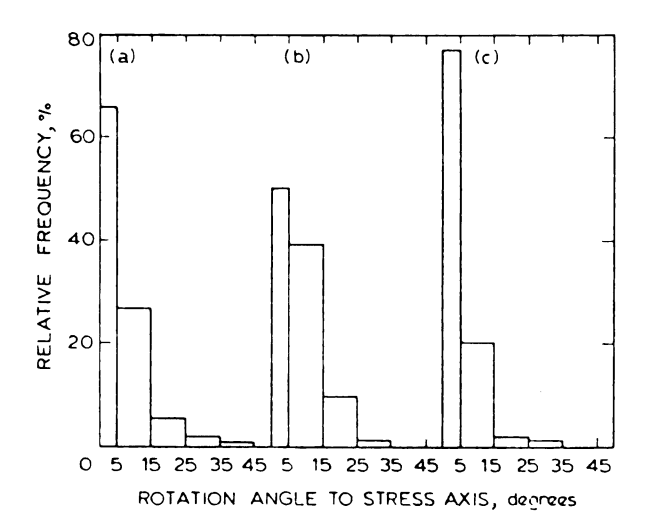


Fig.1.18 Relative frequency of rotation of internal marker lines to stress axis in specimens deformed 60%. (a) At  $\epsilon_A = 2 \times 10^{-3} \min_{i=1}^{4} (b)$  at  $\epsilon_B = 6.7 \times 10^{-3} \min_{i=1}^{4} (c)$  at  $\epsilon_C = 1.1 \times 10^{-1} \min_{i=1}^{4} (c)$ 

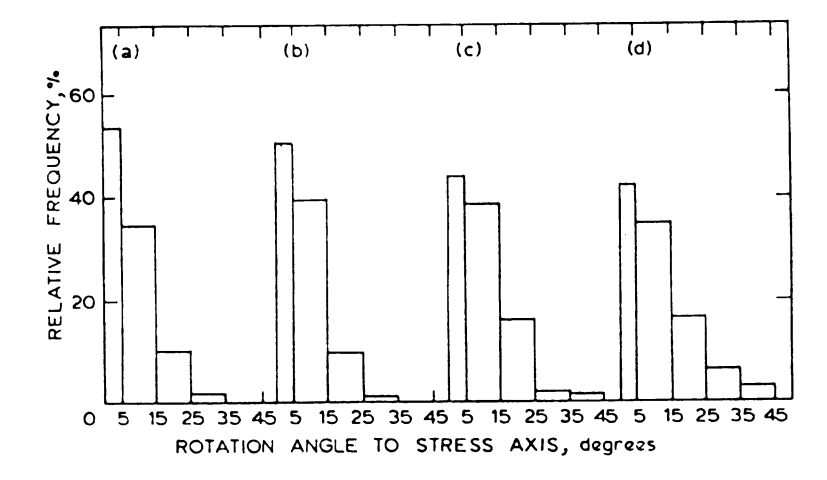


Fig.1.19 Relative frequency of rotation of internal marker lines to stress axis in specimens deformed at  $\epsilon_B=6.7\times10^{-3}$  min Deformed (a) 30%, (b) 60%, (c) 100%, (d) 200%.

compared to the other two strain rates. As the strain increases from 30 to 200, more grains rotate to larger degrees since the greater degrees of grain rotations are required to accommodate the increased amount of grain boundary sliding during superplastic deformation. Whereas the amount of rotation varies from grain to grain and the rotation of a grain usually changes sign during superplastic flow. Therefore the sense of rotation for any one grain depends on its instentaneous surroundings<sup>[104,125]</sup>.

It is also found that grain boundaries become thicker after larger strain when the grain size is noticeably larger (see Fig.1.17) because of the grain rotation and deformation in the grain mantle<sup>[123]</sup>.

Whether or not the dislocation activity occurs during superplastic deformation still is open to debate. Several authors [107,127-129] reported that no dislocation activity accompanied the superplastic deformation in their investigations. But evidence of dislocation activity during superplastic deformation has been found recently. Fig.1.20 shows dislocation density changes with superplastic deformation in regions I to III. A large number of dislocations in grain interior are active during deformation in region III, and dislocation density increases with increasing strain. In region II dislocation has the same trend as that in region III but the

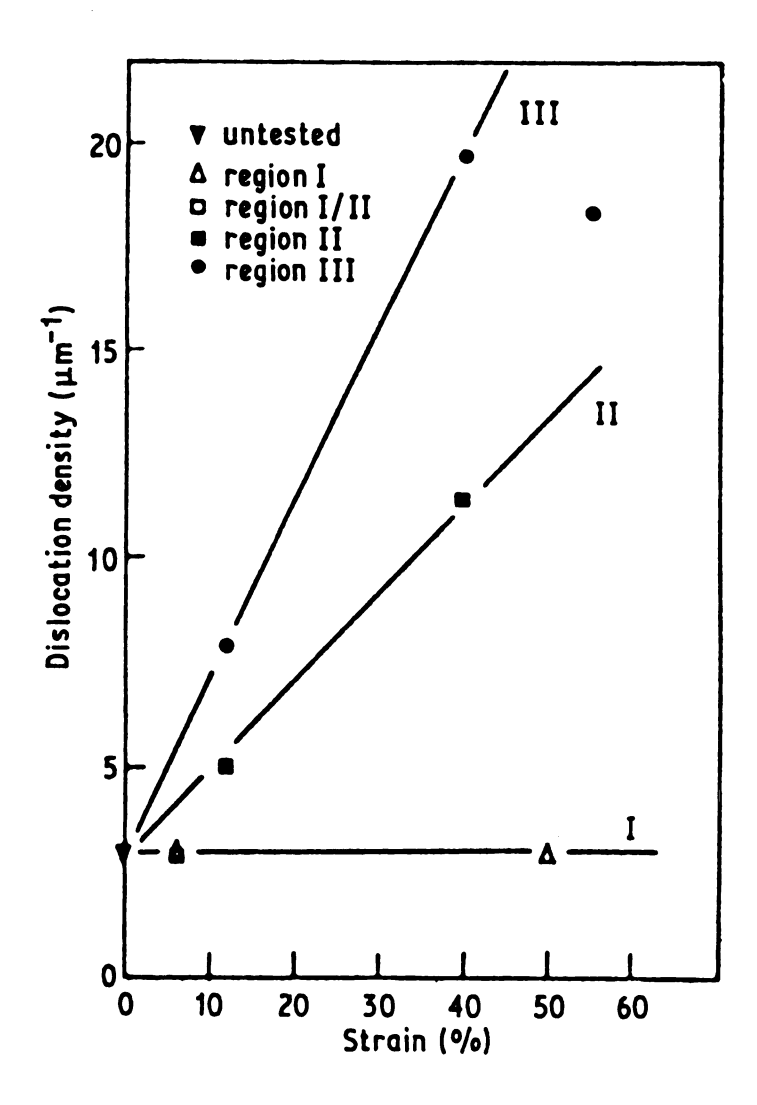


Fig.1.20 Densities of dislocations in twin boundaries as a function of strain for regions I-III.

dislocation density decreases notably. In region III, a high dislocation density was produced by deformation but there were no regular cell structures. Only low angle boundaries and dislocation tangles were observed. In region II, dislocations were found in the grains

containing precipitates, but many grain free from precipitates were without dislocations. Dislocation activity was also found in region I. The Burger's vector distribution was similar at all but the lowest strain rate. This might indicate that at low strain rate the dislocations only accommodate the GBS, but at higher strain rate the dislocations contribute to both GBS and intragranular slip.

## 1.4.4. Mechanisms of Superplastic Deformation

It is a common agreement that GBS plays a major role in superplastic deformation. In order to maintain a compatibility across grain boundaries, extensive accommodations such as diffusion, grain rotation and dislocation motion are required.

## (a) GBS with Diffusion Accommodation

Ashby and Verrall<sup>[99]</sup> proposed a mechanism in which grains switch their neighbours and do not elongate significantly as illustrated in Fig.1.21. The four grains in the initial position, Fig.1.21a, move by GBS along the inclined boundaries to an intermediate saddle position, Fig.1.21b, and further grains move to the final position, Fig.1.21c, by GBS and diffusion accommodation as well as grain boundary migration. In Fig.1.21b, the shapes of grains are changed by diffusion in the region in order

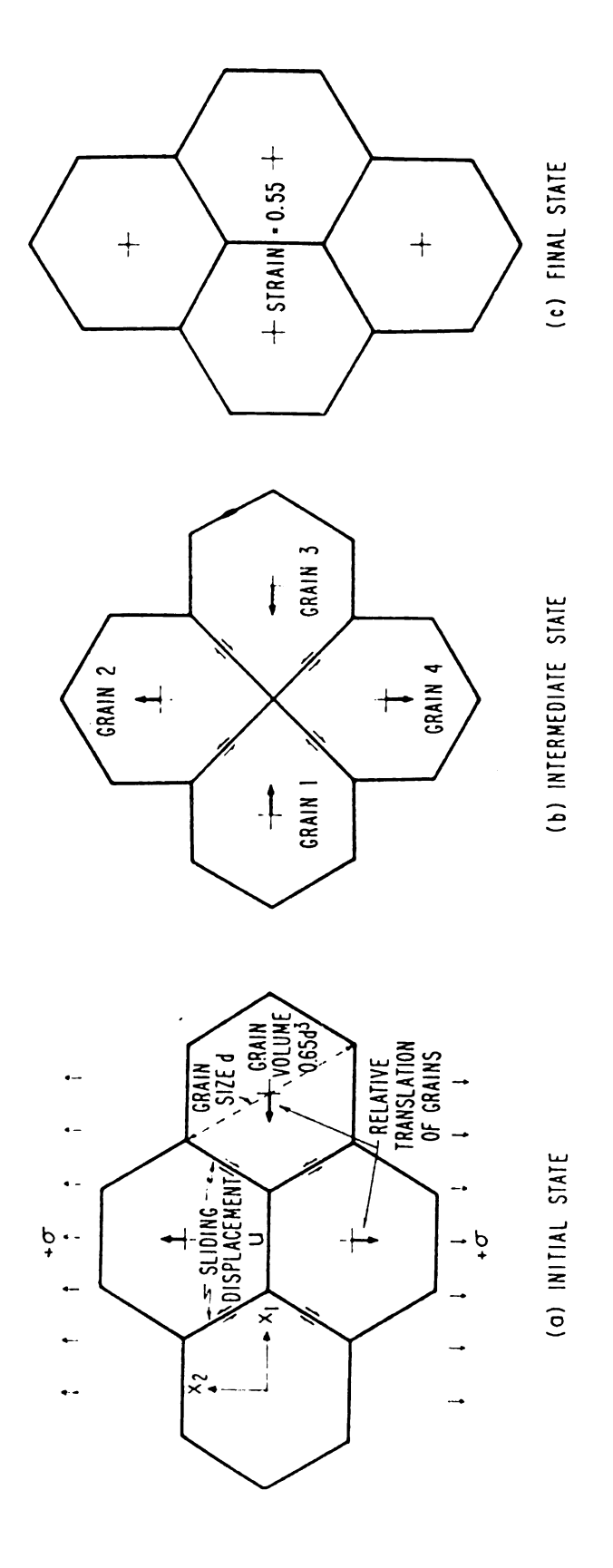


Fig.1.21 The unit step of the deformation process (a)-(c)

to avoid formation of voids. The total true strain in this process is 0.55 (73%). The grain switching event gives rise to a threshold stress because significant energy is required to change grain boundary area during the process in Fig.1.21b. In detail, four irreversible processes are involved in this mechanism: (i) Diffusional process, which is schemetically shown in Fig.1.22: The diffusional process

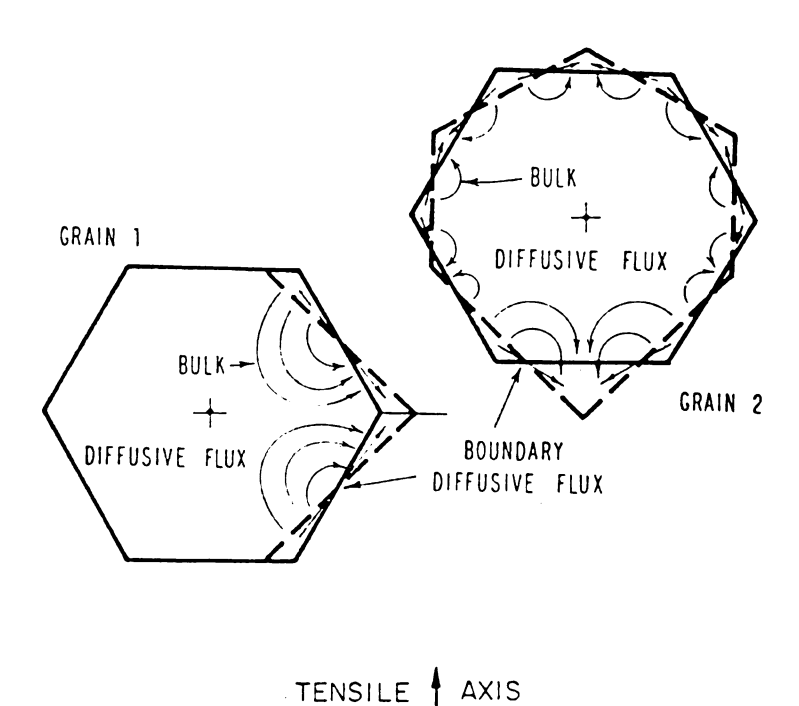


Fig.1.22 The accommodation strains required when grains move from the initial to the intermediate states.

may occur by bulk diffusion through the grains or by diffusion via the grain boundaries. The diffusional path in Fig.1.22 is short compared with those involved in normal diffusion creep and it is for this reason that the strain rate derived by this theory is faster than that for

diffusion creep. (ii) Grain boundary reaction: Grain boundaries may be imperfect sinks or sources for point defects, and therefore grain boundaries may be barriers for vacancies to be removed from or added to the grain boundaries. (iii) Grain boundary sliding: The shear displacements occur in the grain boundary plane and these displacements allow the grains to shift their position relative to each other. (iv) Fluctuations of grain boundary area: Grain boundary area increases as the grains move from their initial state to their intermediate state, which increases the free energy in the system. As the grains move from the intermediate state to the final state, the grain boundary area decreases again, which releases free energy from the system. This process requires that the external stress does enough work to cover the energy increment to permit the superplastic flow to take place, the result of which is a small threshold stress below which the superplastic flow is impossible.

In summary, GBS with diffusion accommodation usually accounts for almost all the strain rate in region I and some part of strain rate in region II. According to this mechanism, grains do not elongate much; the translations and rotations of the grains should destroy any texture; since dislocation motion is not involved, dislocation cells or tangles do not exist; and the deformation occurs in the way of non-uniform flow (see Fig.1.23).

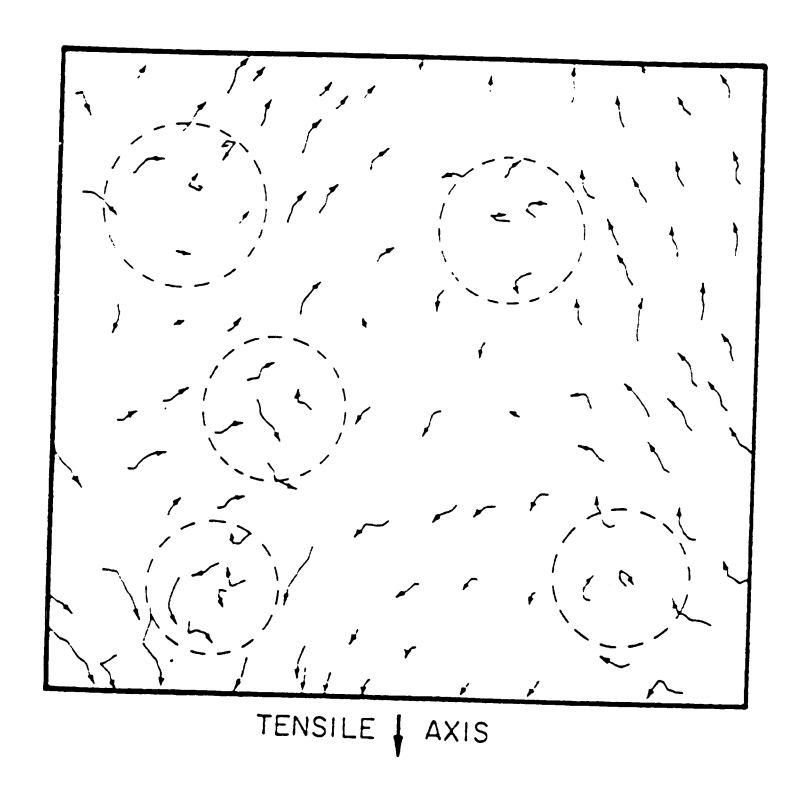


Fig.1.23 The trajectories of grain centers in the emulsion, where a switching event has occured.

# (b) GBS with Dislocation Motion Accommodation

(i) Accommodation by grain boundary dislocation movement. In this mechanism, grain boundary sliding occurs either by grain boundary dislocation glide if the dislocations dissociate so that some of the partial

dislocations have Burger's vectors lying parallel to the grain boundary surface or alternatively by dislocation climb and glide movements if the dislocations retain their original Burger's vectors and remain undissociated. The components of their Burger's vectors parallel to the grain boundary will then contribute to shear parallel to the boundary. Thus grain boundary dislocation movement results in GBS and dislocation pile up at the triple point, (see Fig.1.24).

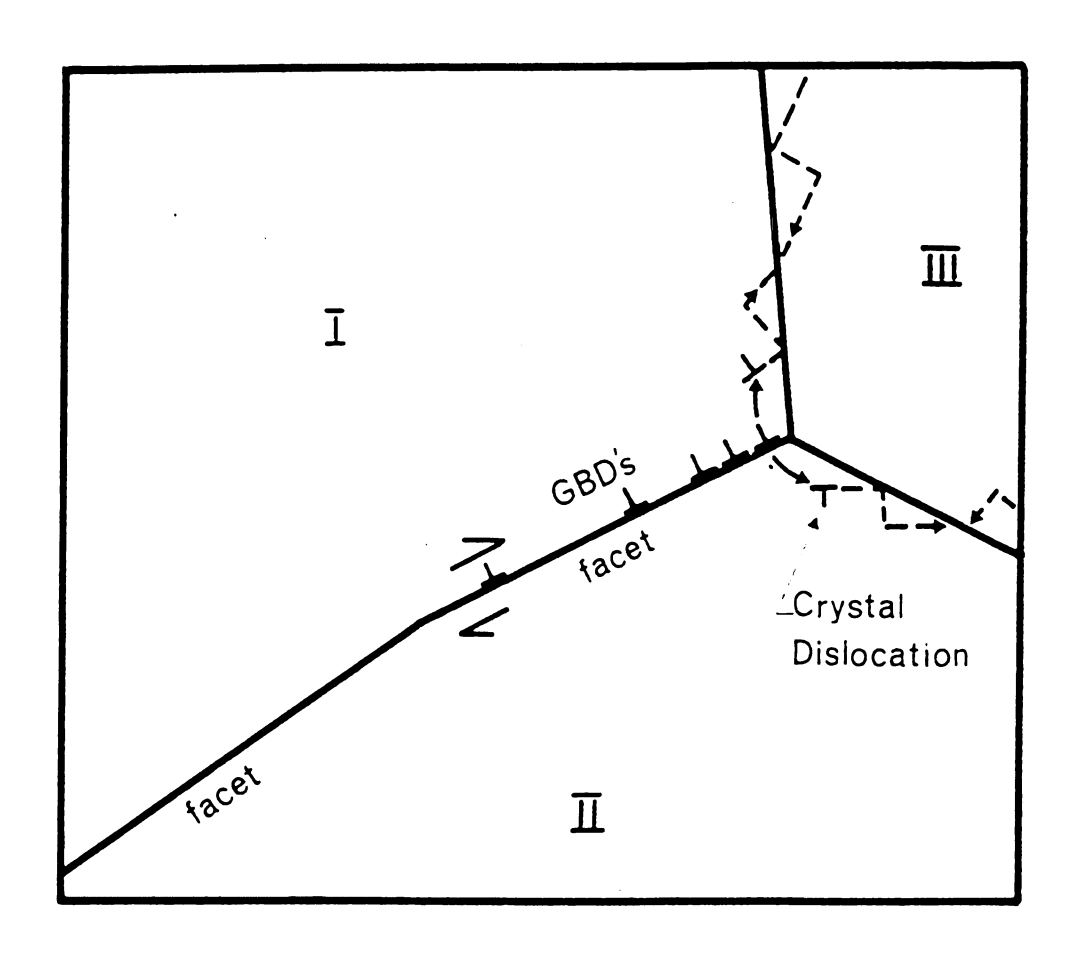


Fig.1.24 GBS and its accommodation to give deformation in region II of superplasticity.

Accommodation at the triple edge is allowed by creating new dislocation under the stress concentration followed by their gliding and climb in the mantle among the adjacent grain boundaries and eventually annihilating or recombining to form new grain boundary dislocations. This mechanism can explain the absence of grain elongation and dislocation cell structure after superpladtic deformation.

(ii) Accommodation by intragranular dislocation movement. When the sliding of groups of grains is blocked by an unfavorably oriented grain, the resultant stress concentration is released by dislocation motion in the blocking grain (see Fig.1.25). The moving dislocation

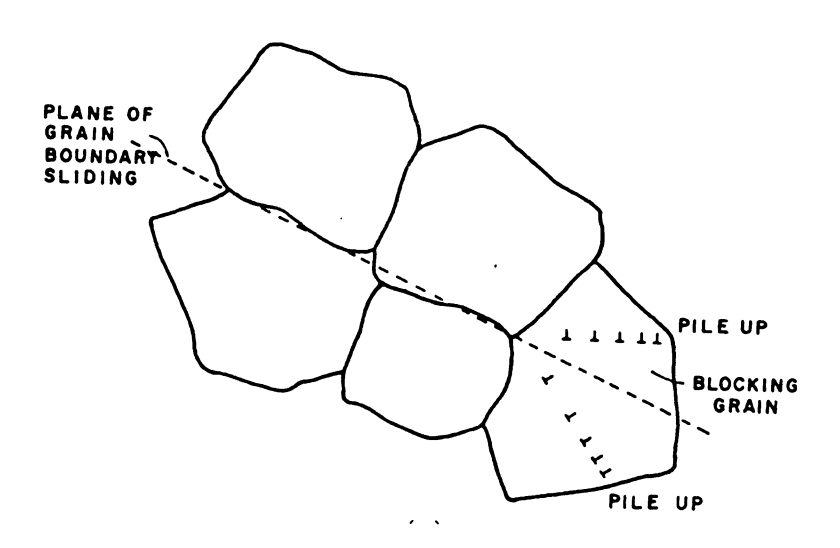


Fig.1.25 Slip accommodation of grain boundary sliding.

glides across the grain and pile up at the opposite grain boundary. The back stress from this dislocation pile up will stop the dislocation source and therefore the GBS. The continuation of GBS requires that the leading dislocation climbs into or along the grain boundary [111]. In the individual grain sliding, the dislocations are generated by ledges and protrusions at the grain boundaries (Fig.1.26). The dislocations traverse the grain and

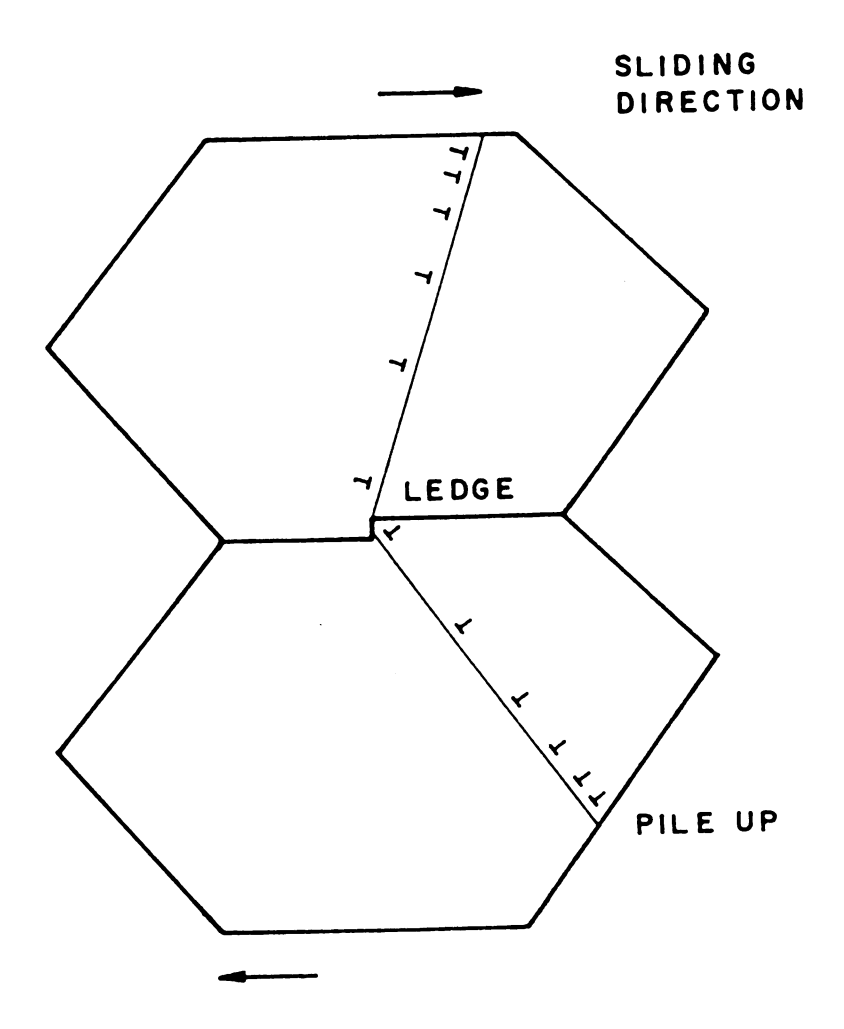


Fig. 1.26 Slip accommodation from grain boundary ledges.

pile up at grain boundaries. Therefore, the rate of GBS is controlled by the climb rate of the leading dislocation towards annihilation sites which are located at grain boundaries.

The dislocation motion mechanisms can also account for the higher part of strain rate in region I and the lower part of strain rate in region II. The texture may destroyed by this mechanism.

#### (c) Dislocation Slip.

This is a mechanism in common with deformation, which is discussed above, and is appliable to the high strain rate region. According to this mechanism, grains elongate and do not change neighbors; dislocations move through the grains and accumulate as cells or tangles; the texture may be created by the deformation.

# 1.5. Relationship Between Texture and Superplastic Deformation

## 1.5.1. Texture Effects on Superplasticity

Anisotropic behaviour in superplastic deformation has been reported in many materials [136,144-146]. This indicates that preferred crystallographic orientations affect the superplastic deformation behaviours. Fig.1.27 shows this anisotropic behaviour of Zn-0.4%Al alloy in

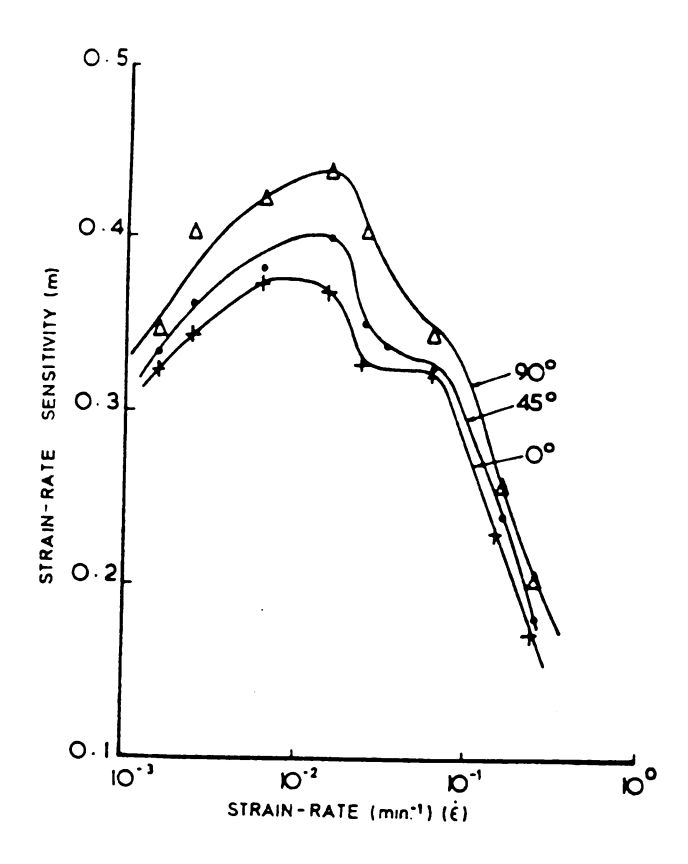
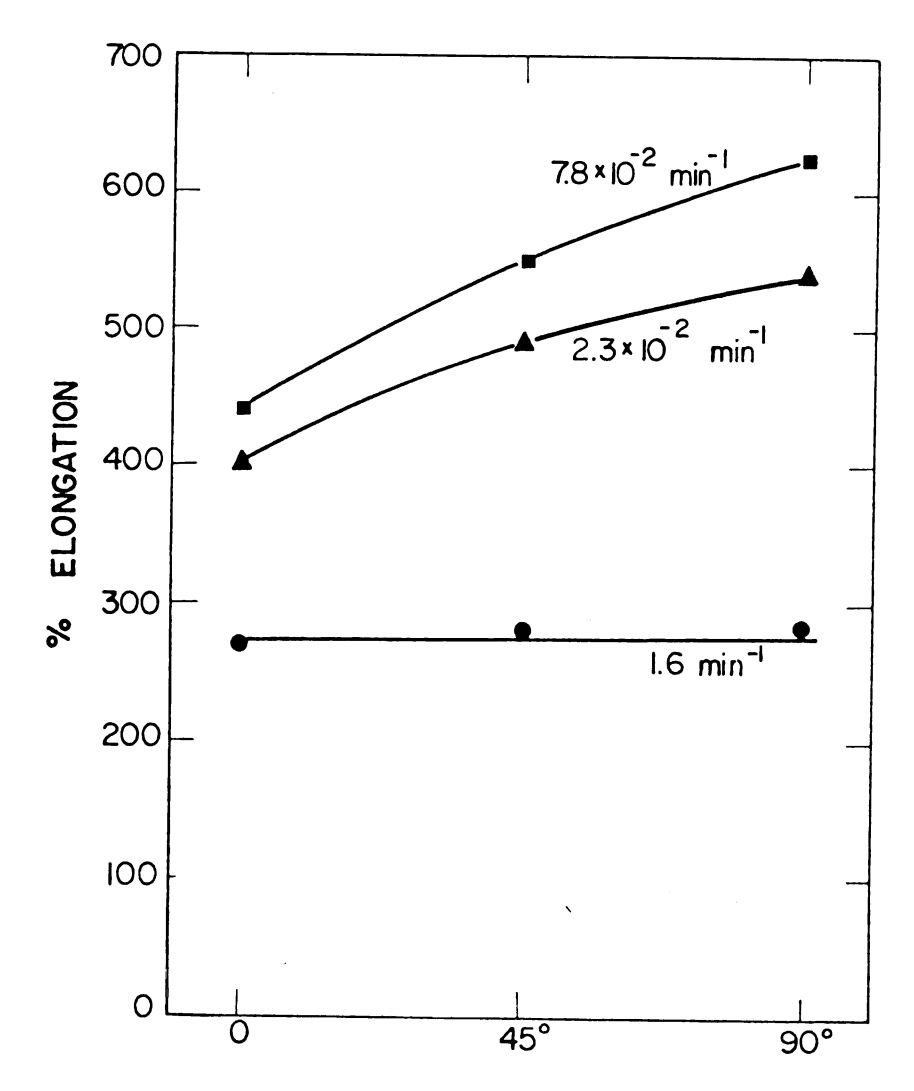


Fig.1.27 Variation of m with strain rate and with direction of straining

sheet form at angles of 0°,45° and 90° to the rolling direction. The strain rate sensitivity (m) increases with increasing the angle to the rolling direction for Zn-0.4%Al alloy. Fig.1.28 shows elongations at fracture as a function of angle of the tensile axis to the rolling direction for aluminum-bronze sheet tested at 800°C. It also indicates that elongation increases with the angle of tensile axis to the rolling direction.



ANGLE OF TENSILE AXIS TO ROLLING DIRECTION

Fig.1.28 Elongation at fracture as a function of angle of the tensile axis to the rolling direction at three strain rates for alumimun-bronze sheet tested at 800°C

It was reported that the formation of a strong crystallographic texture in Zn-22%Al alloy on prior rolling enhenced elongation several times compared to the textureless as-quenched alloy with the similar grain size[134]. The influence of this initial texture on the elongation increases with increasing strain rate. In Fig.1.29 for as-quenched staes 1 and 2, the difference in elongation increases from 150% at  $\dot{\epsilon} = 2.5 \times 10^{-4} \text{ s}^{-1}$  to 450% at  $\dot{\epsilon} = 2.8 \times 10^{-1} \text{ s}^{-1}$ , and for the asrolled states 3 and 4, the difference in elongation increases with strain rate even more, that is, at high strain rate, this difference in elongation reaches 800%. The pre-existing texture causes a decrease in the flow stress of superplastic deformation, and this initial defference in flow stress between the texture and textureless material is retained up to a very high degree of strain (see Fig.1.30). The initial texture also shifts the optimum strain rate region to higher strain rate (see Fig.1.31).

The texture effects on superplasticity increase with a decrease in temperature. In the as-quenched alloy at  $250^{\circ}$  and  $\dot{\epsilon}=2.8\times10^{-4}\mathrm{s}^{-1}$  in state 2, the elongation is 1.3 times higher and flow stress 1.25 times lower than those in state 1, but at  $150^{\circ}\mathrm{C}$  this difference is 2.1 and 1.5 times respectively. Texture effects on an optimum strain rate are much greater at  $150^{\circ}\mathrm{C}$  than those at  $250^{\circ}\mathrm{C}$ . The difference

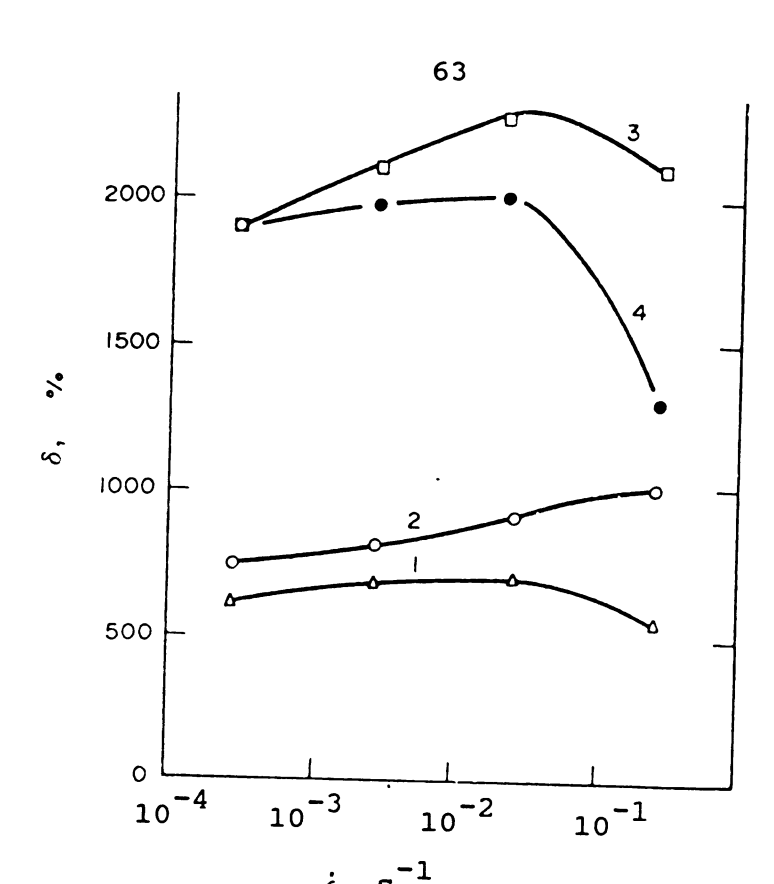


Fig.1.29 Elongation as a function of strain rate

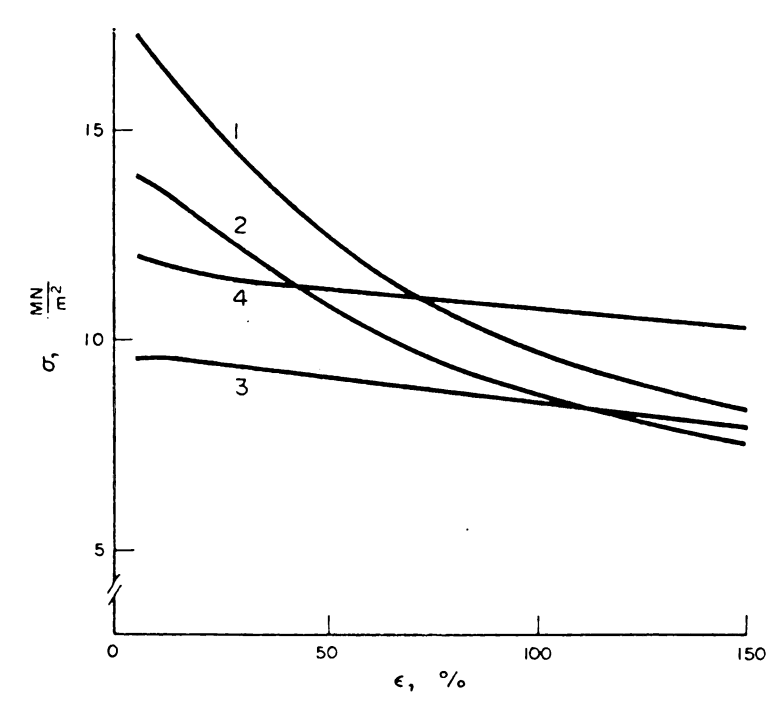
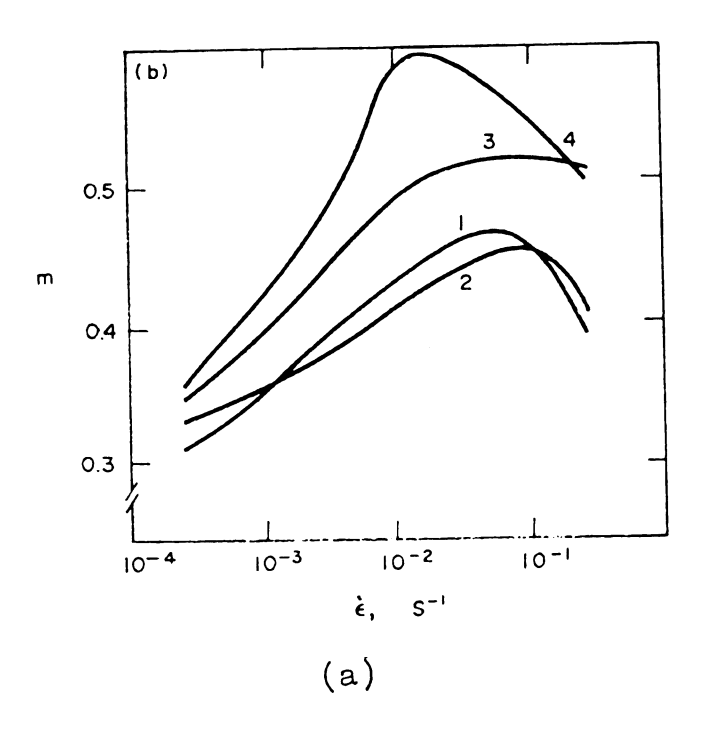


Fig.1.30 True stress/true strain curves on extention with  $\epsilon_0$ =2.8x10 s at 250 C for different states of the alloy.



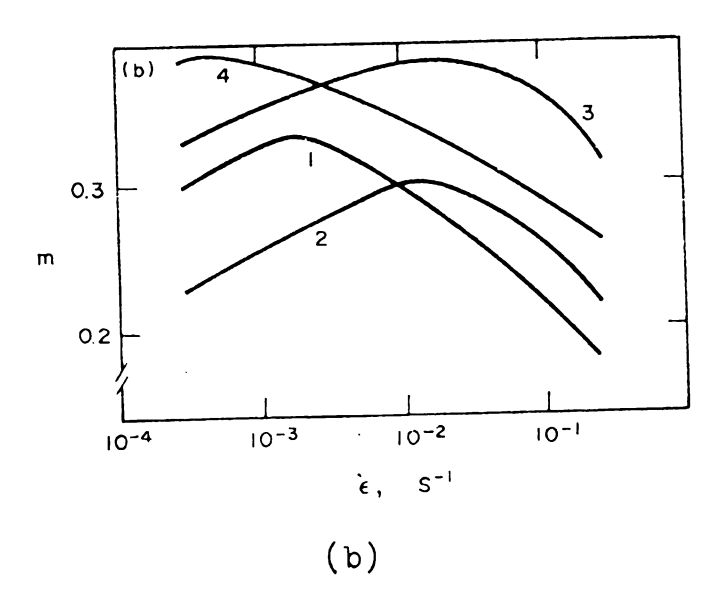


Fig.1.31 Strain rate sensitivity as a function of strain rate. (a) At 250°C, (b) at 150°C.

1. quenching, rolling at 250°C, annealing at 350°C for 5h, water quenching. 2. Quenching, 96.6% rolling at 20°C, annealing at 350°C for 5h, quenching.

3. Quenching, 96.6% rolling at 20°. 4. Quenching, rolling to 96.6% at 250°

in optimum strain rates between states 1 and 2 at 250°C makes 2-3 times whereas at 150°C it is 15 times. Texture can extend the temperature range of superplastic deformation into the lower temperature region.

It was proposed<sup>[134]</sup> that the effects of texture on the superplastic flow could be connected mainly with the dependence of grain boundary structure on the texture.

On the condition that the grain shape and size are the same, the texture causes a change in grain misorientation and different grain boundary structure and therefore the defferent superplastic behaviors.

### 1.5.2. Superplastic Deformation Effects on Texture

Superplastic deformation has two principal effects on the texture. First, there is a reduction in the overall texture due to GBS and grain rotation. Second, in addition to the overall texture reduction, some texture components are stabilized and new ones are created, indicating intergranular slip and dynamic recrystallization occurrence.

(i) Grain boundary sliding: GBS would, as discussed before, be expected to rotate the grains randomly, therefore, GBS results in the overall reduction in texture during superplastic deformation [138-140,147].

(ii) Slip<sup>[124,136,139,148-151]</sup>: Superplastic deformation is one of the few polycrystalline deformation modes in which diffusive flow may relax the need for five independent slip systems to be operative and single slip can be expected. The occurrence of single slip during superplastic deformation manifests itself in the stabilisation or build-up of material in <121> orientation (for fcc crystal). During superplastic deformation, the diffusional accommodation allows a grain to act as a isolated single crystal in uniaxial tension and to rotate until the second slip system activated stabilises the crystal at <121>. Such orientations are stable in the sense that any rotation away from them occasioned by GBS leads to a counteracting slip rotation back towards <121>. Furthermore, <121> orientations have a relatively high Schmid factor(0.41), so single slip is to be expected in grains at or near these orientations. But it should be noticed that the single slip which builds up <121> orientations is in response to the imposed stress system and contributes some part of the overall strain. If single slip, which results from the internal stress concentrations caused by GBS, occurs as an accommodation mechanism, this slip will not be in directions related to the tensile axis and so will not contribute to this texture component.

At higher strain rates (region III), multiple slip on {111}<110> systems in the fcc crystal occurs by forming a

strong <111> fiber texture. This is predicted to be the stable end orientation under conditions of multiple slip on {111}<110> systems in polycrystals, as five of the six possible systems are required to provide the shape change and thus the operation of the sixth allows only a rotation about the tensile axis.

Therefore, it is concluded that (1) the number of operating slip systems increases with increasing strain rate, (2) the relative contributions of individual systems change with strain rate, and (3) even when no shift in the positions of the texture peaks is seen, it is due to slip in two systems which rotate the grain by equal but opposite amounts.

(iii) Dynamic recrystallization: Dynamic recrystallization is of the type produced by short time static annealing, which was discussed in previous section. Here we are not going to discuss it further.

#### 1.6. Representation of An Orientation

The crystallite orientation is defined as the rotation (g) which transforms the sample coordinate system  $K_{A}(XYZ)$  into that of the crystallite  $K_{B}(X'Y'Z')$ , (see Fig.1.32). The orientation g may be characterized in many different ways. In the following sections, we are going to

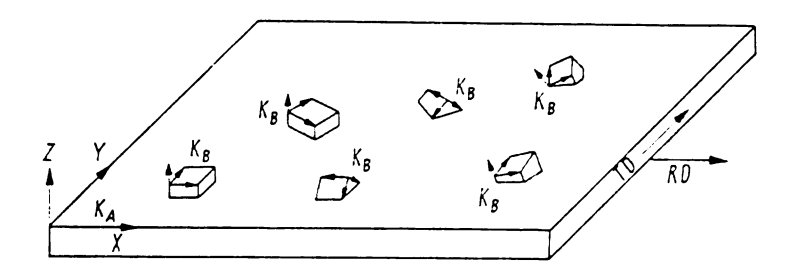


Fig.1.32 The sample fixed coordinate system  $\rm K_{A}$  and the crystal fixed coordinate system  $\rm K_{B}$  in the sheet.

discuss some of these representations.

## 1.6.1. Introduction to Rotation System

## (a) Euler Angles.

Two kinds of variants, Bunge's and Roe's variants, are usually used to represent the orientation g in Euler angle space. In the Bunge's rotation, the definition of Euler angles is shown in Fig.1.33. At the begining of the rotation, the axes of the crystal coordinate system coincide with those of the sample coordinate system. The crystal coordinate system is then first rotated about the Z'-axis through the angle  $\varphi_1(g^{Z'})$ , then about the X'-axis (in its new orientation) through  $\phi(g^{X'})$ , and finally, once again about the Z'-axis (in its new orientation) through the angle  $\varphi_2(g^{Z'})$ . Thus the rotation g is represented in the Bunge's rotation system by

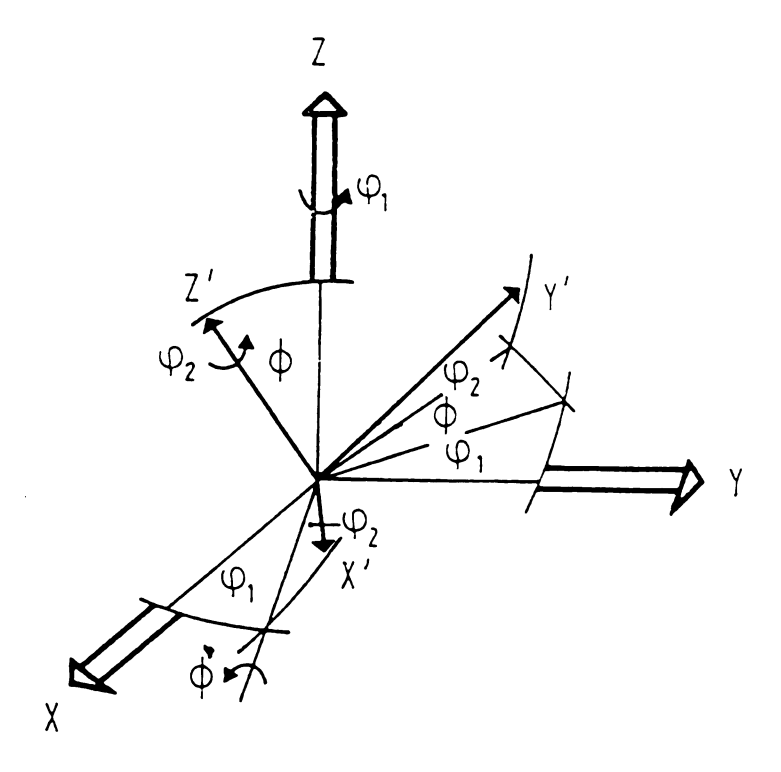


Fig.1.33 Definition of the Euler angles  $\varphi_1^{\ \phi \varphi}_2$ 

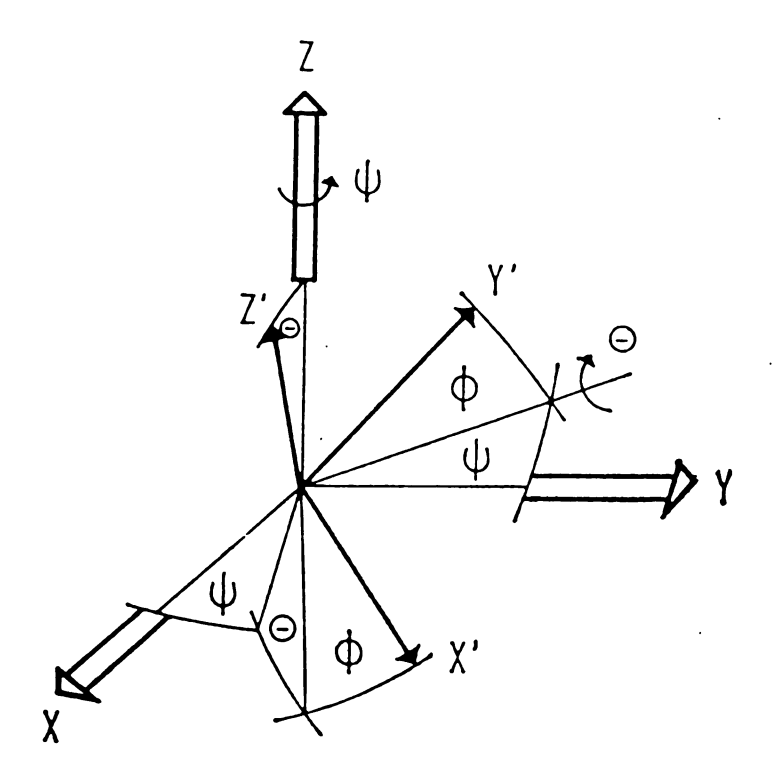


Fig.1.34 Definition of the Euler angles  $\Psi\theta\Phi$ .

$$g = \{\varphi_1, \Phi, \varphi_2\} = g^{Z'} g^{X'} g^{Z'}$$
 (1.11)

In the Roe's Variants, the second rotation is not carried out about the X'-axis, but about the Y'-axis. The first and third rotations remain, as Bunge's, about the Z'-axis, which is shown in Fig.1.34. The Euler angles are defined by  $\Psi\theta\Phi$  in this case. Thus the rotation g can be represented by

$$g = \{\Psi\theta\Phi\} = g^{Z'} g^{Y'} g^{Z'}$$
 (1.12)

(b) Rotation Axis and Angle.

The rotation can be obtained by specifying the rotation axis d and rotation angle  $\omega$  about the direction d (see Fig.1.35). So the rotation g is

$$g = \{d, \omega\} = \{\theta, \Psi, \omega\} \tag{1.13}$$

## 1.6.2. Representation of the Orientation

(a) Representation of the Orientation in the Pole Figure.

The pole figure shows a specific crystal direction [hkl] which is fixed in the crystal coordinate system  $\mathbf{K}_{\mathrm{B}}$  with respect to the sample coordinate system  $\mathbf{K}_{\mathrm{A}}$  in stereographic projection. Therefore, the orientation of the pole can be described by the polar coordinates  $\Phi_{\mathrm{hk}}$  and

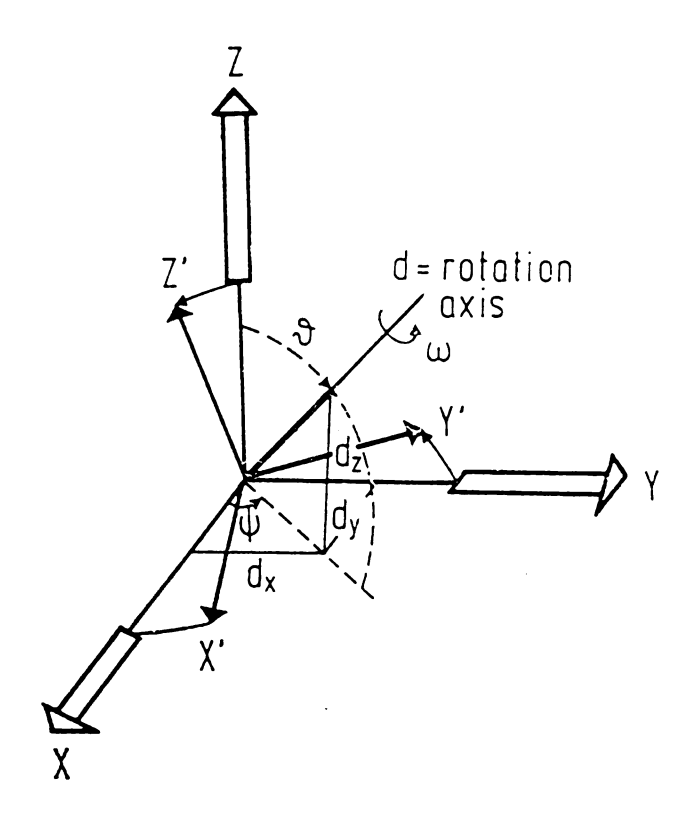


Fig.1.35 Representation of a rotation by the rotation axis d and the appropriate rotation angle  $\omega$ .

 $r_{\rm hkl}$ . As an example, Fig.1.36 shows the representations of <100>,<110> and <111> poles in pole figures. This representation of the orientation is redundant because the orientation is specified by only two angles.

(b) Representation of the Orientation in the Inverse Pole Figure.

The inverse pole figure shows the orientation of the

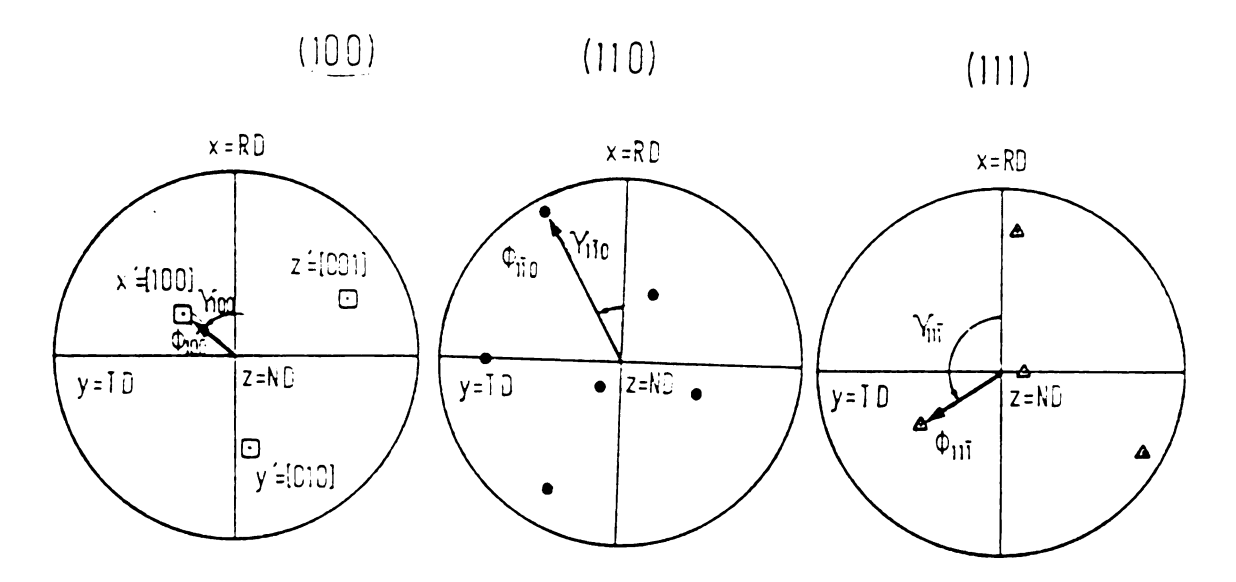


Fig.1.36 The orientations of some crystal directions in pole figures.

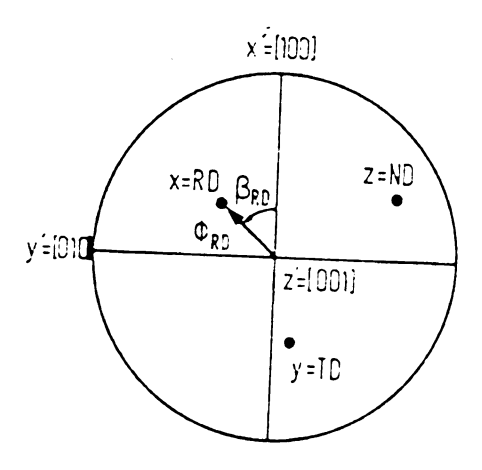


Fig.1.37 The prientations of the specimen directions in inverse pole figure.

specimen directions (for example, rolling direction, transverse direction and normal direction) relative to the crystal coordinate axes in stereographic projection, which is shown in Fig.1.37. This representation is also redundant as the pole figure is.

## (c) Representation by Miller Indices.

A method rather frequently used for describing an orientation is to indicate rolling plane and rolling direction by the Miller indices (hkl)[uvw], where (hkl) is the crystal plane which is parallel to the sheet plane and [uvw] is the crystal direction which is parallel to the sheet rolling direction. Therefore, the rotation by Miller indices is writen as

$$g = (hkl)[uvw]$$
 (1.14)

This representation is redundant too because this representation is related to the representation of the inverse pole figure if we express the orientation of directions Z=ND and X=RD by the corresponding miller indices.

## (d) Matrix Representation.

The coordinates x'y'z' of an arbitary point in the crystal coordinate system  $K_{p}=\{x'y'z'\}$  can be expressed in

terms of the coordinates xyz in the sample coordinate system  $K_{\lambda} = \{xyz\}$ ,

$$x' = a_{11}x + a_{12}y + a_{13}z$$
 (1.15)

$$y' = a_{21}x + a_{22}y + a_{23}z$$
 (1.16)

$$z' = a_{31}x + a_{32}y + a_{33}z$$
 (1.17)

or

From the inversion of equation (1.18), we can express the coordinates xyz of an arbitary point in the sample coordinate system  $K_A = \{XYZ\}$  by means of the coordinates x'y'z' in the crystal coordinate system  $K_B = \{X'Y'Z'\}$ ,

$$x_j = a_{ij}^{-1}x'_i = a_{ji}x'_i$$
 i,j=1,2,3. (1.19)

In equation (1.18), it is easily found that the columns of  $a_{ij}$  are the direction cosines of the sample directions X= RD, Y= TD, Z=ND in the crystal coordinate system, that is, the direction cosines of the directions in the inverse pole figure. Similarly, from the equation (1.19), the rows of  $a_{ij}$  are the direction cosines of the directions X'=[100], Y'=[010], Z'=[001] in the pole figure.

### (e) Orientation Distribution Function.

For a complete description of the crystal orientation

of a polycrystalline material, one must specify the relevant orientation g for each point with coordinates x,y,z within the sample

$$g = g(x, y, z) \tag{1.20}$$

If it is writen in Euler angles, then

$$g = g(\varphi_1, \phi, \varphi_2) = g[\varphi_1(x, y, z), \Phi(x, y, z), \varphi_2(x, y, z)]$$
 (1.21)

Such a representation of crystal orientation is very complicated. If we consider only the orientation but not the position coordinates x,y,z of a volume element in the sample, we will get a much simpler representation.

Therefore, by assuming that V is the total sample volume, dv is the volume element of the sample which possess the orientation g within the element of orientation dg, we can define an orientation distribution function f(g) (in this case the orientation distribution function of the volume) by

$$\frac{dV}{V} = f(g)dg \qquad (1.22)$$

The orientation distribution function f(g) can be obtained by a method of series expansion of spherical harmonics and usually expressed in Euler angle coordinates, i.e.,

$$f(\varphi_1, \phi, \varphi_2)$$
 or  $f(\Psi, \theta, \Phi)$ 

(f) Relationship between Euler Angles and Miller Indices.

From the matrix representation, we can obtain the matrix discription for the three Euler rotation

$$g^{Z'} = \begin{bmatrix} \cos\varphi_1 & \sin\varphi_1 & 0 \\ -\sin\varphi_1 & \cos\varphi_1 & 0 \\ 0 & 0 & 1 \end{bmatrix}$$
 (1.23)

$$g^{X'} = \begin{bmatrix} 1 & 0 & 0 \\ 0 & \cos\phi & \sin\phi \\ 0 & -\sin\phi & \cos\phi \end{bmatrix}$$
 (1.24)

$$g^{z'} = \begin{bmatrix} \cos\varphi_2 & \sin\varphi_2 & 0 \\ -\sin\varphi_2 & \cos\varphi_2 & 0 \\ 0 & 0 & 1 \end{bmatrix}$$
 (1.25)

Therefore, the rotation g can be expressed as

$$g(\varphi_1, \phi, \varphi_2) = g^{Z'} g^{X'} g^{Z'}$$

$$= \begin{bmatrix} \cos\varphi_1\cos\varphi_2 - \sin\varphi_1\sin\varphi_2\cos\phi & \sin\varphi_1\cos\varphi_2 + \cos\varphi_1\sin\varphi_2\cos\phi & \sin\varphi_2\sin\phi \\ -\cos\varphi_1\sin\varphi_2 - \sin\varphi_1\cos\varphi_2\cos\phi & -\sin\varphi_1\sin\varphi_2 + \cos\varphi_1\cos\varphi_2\cos\phi & \cos\varphi_2\sin\phi \\ & \sin\varphi_1\sin\varphi & -\cos\varphi_1\sin\phi & \cos\phi \end{bmatrix}$$

In the miller index representation, we have

$$z = ND = \frac{h}{m} x' + \frac{k}{m} y' + \frac{1}{m} z'$$
 (1.27)

$$x = RD = \frac{u}{n}x' + \frac{v}{n}y' + \frac{w}{n}z'$$
 (1.28)

where  $m = \sqrt{h^2 + k^2 + 1^2}$ ,  $n = \sqrt{u^2 + v^2 + w^2}$ . Thus, according to  $Y = Z \times X$ ,

$$y = TD = \frac{kw-lv}{mn} x' + \frac{lu-hw}{mn} y' + \frac{hv-ku}{mn} z'$$
 (1.29)

so, the matrix of rotation defined by the Miller indices (hkl)[uvw] is expressed by

$$g((hkl)[uvw]) = \begin{bmatrix} \frac{u}{n} & \frac{kw-lv}{mn} & \frac{h}{m} \\ \frac{v}{n} & \frac{lu-hw}{mn} & \frac{k}{m} \\ \frac{w}{n} & \frac{hv-ku}{mn} & \frac{1}{m} \end{bmatrix}$$
(1.30)

Comparing the matrix elements of equation (1.26) with the corresponding ones of equations (1.30), we obtain the relation between the Euler angle representation and Miller index representation

$$h = m \sin\phi \sin\phi_2 \tag{1.31}$$

$$k = m \sin\phi\cos\varphi_2 \tag{1.32}$$

$$1 = m \cos \phi \tag{1.33}$$

$$u = n(\cos\varphi_1 \cos\varphi_2 - \sin\varphi_1 \sin\varphi_2 \cos\phi) \qquad (1.34)$$

$$v = n(-\cos\varphi_1 \sin\varphi_2 - \sin\varphi_1 \cos\varphi_2 \cos\phi) \qquad (1.35)$$

$$w = n \sin \varphi_1 \sin \phi \tag{1.36}$$

By inversion of these relations, we obtain the Euler angles which are expressed in terms of the miller indices (hkl)[uvw],

$$\phi = \arccos \frac{1}{\sqrt{h^2 + k^2 + 1^2}}$$
 (1.37)

$$\varphi_2 = \arccos \frac{k}{\sqrt{h^2 + k^2}} = \arcsin \frac{h}{\sqrt{h^2 + k^2}}$$
 (1.38)

$$\varphi_1 = \arcsin \left[ \frac{w}{\sqrt{u^2 + v^2 + w^2}} \cdot \sqrt{\frac{h^2 + k^2 + 1^2}{h^2 + k^2}} \right]$$
 (1.39)

For the rotation in the Roe's coordinate system, we have

$$g = \begin{bmatrix} \cos\Psi & \sin\Psi & 0 \\ -\sin\Psi & \cos\Psi & 0 \\ 0 & 0 & 1 \end{bmatrix}$$
 (1.40)

$$g = \begin{bmatrix} \cos\theta & 0 & -\sin\theta \\ 0 & 1 & 0 \\ \sin\theta & 0 & \cos\theta \end{bmatrix}$$
 (1.41)

$$g = \begin{bmatrix} \cos \Phi & \sin \Phi & 0 \\ -\sin \Phi & \cos \Phi & 0 \end{bmatrix}$$
 (1.42)

thus,

$$g(\Psi\theta\Phi) = g^{Z'} g^{Y'} g^{Z'}$$

$$= \begin{bmatrix} \cos \Phi \cos \theta \cos \Psi - \sin \Phi \sin \Psi & \cos \Phi \cos \theta \cos \Psi + \sin \Phi \cos \Psi & -\cos \Phi \sin \theta \\ -\sin \Phi \cos \theta \cos \Psi - \cos \Phi \sin \Psi & -\sin \Phi \cos \theta \sin \Psi + \cos \Phi \cos \Psi & \sin \Phi \sin \theta \\ & \sin \theta \cos \Psi & \sin \theta \sin \Psi & \cos \theta \end{bmatrix}$$

$$(1.43)$$

Therefore, by comparing the equation (1.43) with equation (1.30), the relation between the Euler angles and miller indices in Roe coordinate system can be expressed as

$$h = -m \cos \Phi \sin \theta \qquad (1.44)$$

$$k = m \sin \Phi \sin \theta \qquad (1.45)$$

$$l = m \cos \theta \qquad (1.46)$$

$$u = n(\cos \Phi \cos \theta \cos \Psi - \sin \Phi \sin \Psi) \qquad (1.47)$$

$$v = n(-\sin \Phi \cos \theta \cos \Psi - \cos \Phi \sin \Psi) \qquad (1.48)$$

$$w = n \sin \theta \cos \Psi \qquad (1.49)$$

and by inverting these equations, we have

$$\theta = \arccos \frac{1}{\sqrt{h^2 + k^2 + 1^2}} \tag{1.50}$$

$$\Phi = \arcsin \frac{k}{\sqrt{h^2 + k^2}} = \arccos \left[ -\frac{h}{\sqrt{h^2 + k^2}} \right]$$
 (1.51)

$$\Psi = \arccos \left[ \frac{w}{\sqrt{u^2 + v^2 + w^2}} \cdot \sqrt{\frac{h^2 + k^2 + 1^2}{h^2 + k^2}} \right]$$
 (1.52)

By comparing equations (1.37)-(1.39) with equations (1.50)-1.52), we can easily find the relationship between two Euler angle systems,

$$\varphi_1 = \Psi + \pi/2 \tag{1.53}$$

$$\phi = \theta \tag{1.54}$$

$$\varphi_2 = \Phi - \pi/2 \tag{1.55}$$

which is shown in Fig.1.38.

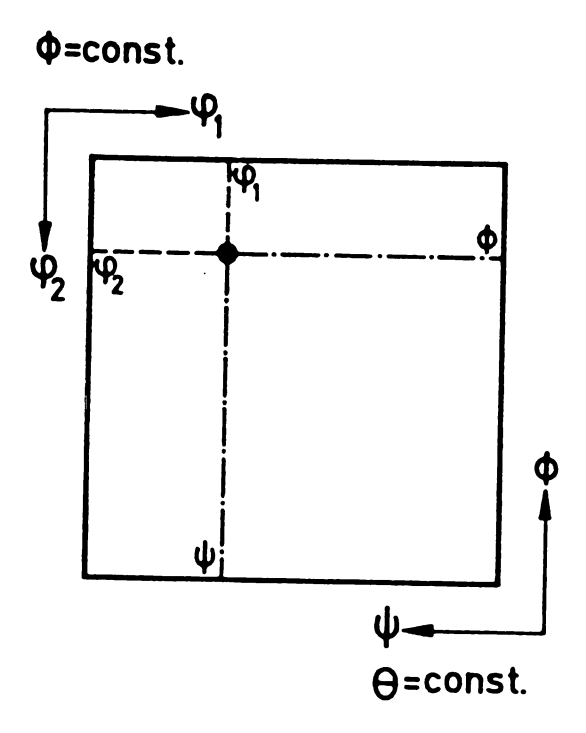


Fig.1.38 Relationships between the angles  $\varphi_1$ ,  $\phi$ ,  $\varphi_2$  and  $\psi$ ,  $\theta$ ,  $\phi$ .

#### CHAPTER 2

#### EXPERIMENTAL PROCEDURES

The material used in this study was IN90211, which has a composition similar to 2124 aluminium alloy (Table 2.1). In addition to solution hardening provided by magnesium atoms and

Table 2.1 Composition(wt%) of IN90211

_	Mg	Cu	С	0	Al <sub>2</sub> Cu	Al <sub>4</sub> C <sub>3</sub>	Al <sub>2</sub> O <sub>3</sub>	Al
	2.0*	4.4 0.9	1.1	0.8	6.4 <sup>*</sup> 4.1vol* <sup>*</sup>	4.3 <sup>*</sup> 4.1vol% <sup>*</sup>	1.7 <sup>*</sup> 1.2vol% <sup>*</sup>	91.7 84.7 90.6vol%

<sup>\*</sup> Assuming 80% Cu in Al<sub>2</sub>Cu, O and C in Al<sub>4</sub>C<sub>3</sub>, and Mg in solution.

precipitation hardening provided by copper in the form of Al<sub>2</sub>Cu phase, the mechanical alloying process introduces about 5 vol% fine oxide and carbide dispersions that stabilize the grain size.

The specimens were machined from a processed sheet of IN90211. The sheet was made from an extruded 25mm rod provided by Novamet Aluminum (lot 85V032). The rod was forge flattened and rolled at elevated temperature to a thickness of 2.5mm. The sheet was annealed at 492°C for 1 hour and water quenched. The specimen was nominally

2.5x2.5mm<sup>2</sup> in cross section, and the gage length was 6.4mm long, with the tensile axis parallel to the rolling direction. The specimens were quickly heated in about 10 minutes with a radiant furnace, and deformed at constant true strain rate in a hydraulic testing machine. The temperature gradient along the specimen was within 3°C, and the specimen was air colled following fracture.

The specimens used in this study were superplastically deformed at (1)  $\dot{\epsilon}$ =1/sec, T=425°C; (2)  $\dot{\epsilon}$ =77/sec, T=475° and (3)  $\dot{\epsilon}$ =330/sec, T=475°.

Texture measurements were made on a computer controlled four axis goniometer system in a Scintag Diffractometer with a graphite monochrometer. Specimens were mounted and ground to the approximate center of the specimen.

Incomplete (111),(200), and (220) pole figures were made along the superplastically deformed specimen shown in Figure 2.1. The reflection method was used, with 5° azimuthal and 5° tilt increments up to a maximum tilt of 70°. A 1mm diameter mask was used to limit the diffracted signal to the desired part of the specimen. The CODF (crystal orientation distribution function) was calculated using the coefficients of the spherical harmonic expansion of the orientation distribution with expansion to 1<sub>max</sub>=22. The software was popLA (the preferred orientation package from Los Alamos, Los Alamos National Laboratory).

#### CHAPTER 3

#### RESULTS

The CODF has the advantage of being a unique result compared to the pole figure and inverse pole figure. Therefore, we are investigated the texture evolution with CODF. The experimental pole figure and inverse pole figure are presented in the appendix. For convenience, an indexed  $\Phi=0^{\circ}$  section of CODF is ploted in Fig.3.1. Most of the

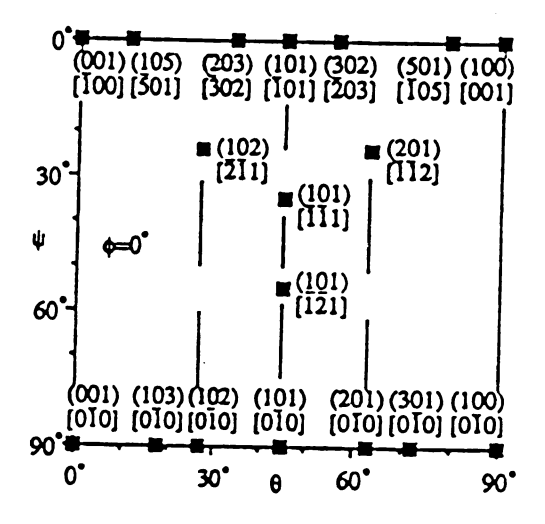


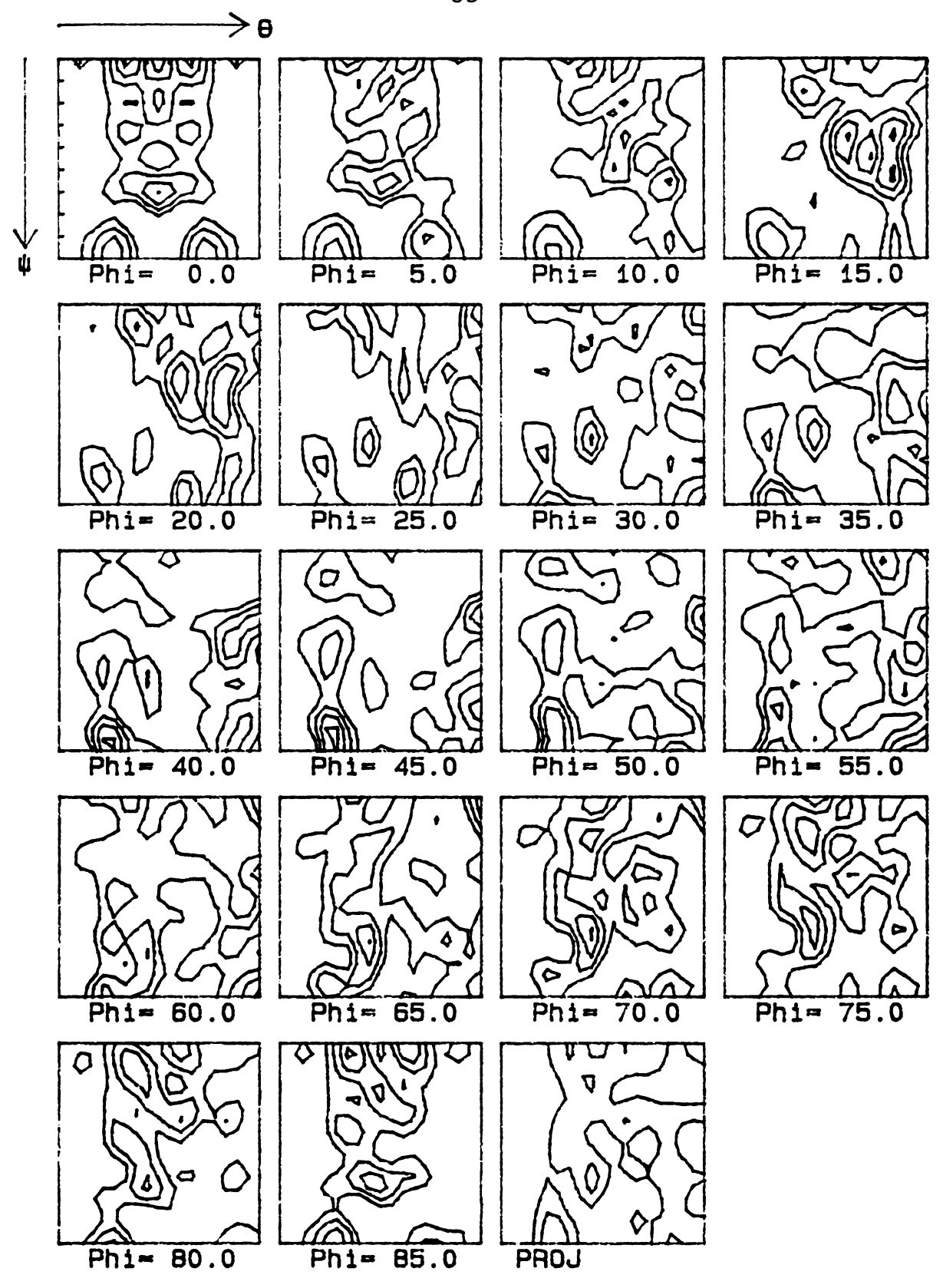
Fig.3.1 Some ideal components in  $\Phi=0^{\circ}$  section

important texture changes can be observed in this section. Some aditional components will also be described.

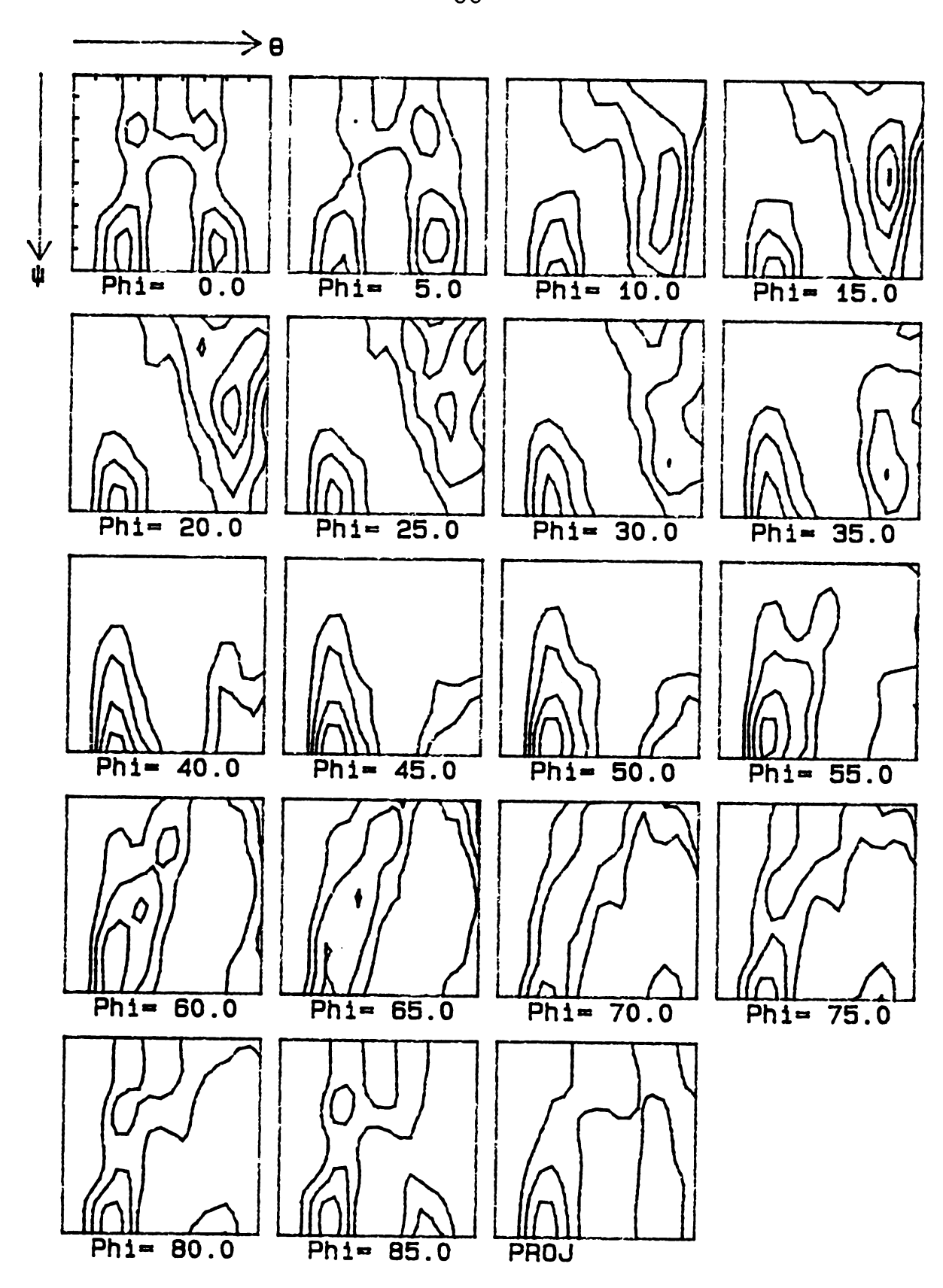
## 3.1 Specimen Deformed at $\dot{\epsilon}=1/\text{sec}$ and T=425°C

The complete CODFs obtained from the specimen deformed at the strain rate  $i=1/\sec$  and the temperature T=425°C are shown at sections of constant  $\Phi$  in Fig.3.2. For brevity, Changes in texture arising from superplastic deformation are investigated in terms of the  $\Phi=0$ ° section of the CODF for this specimen, which are shown in Fig.3.3.

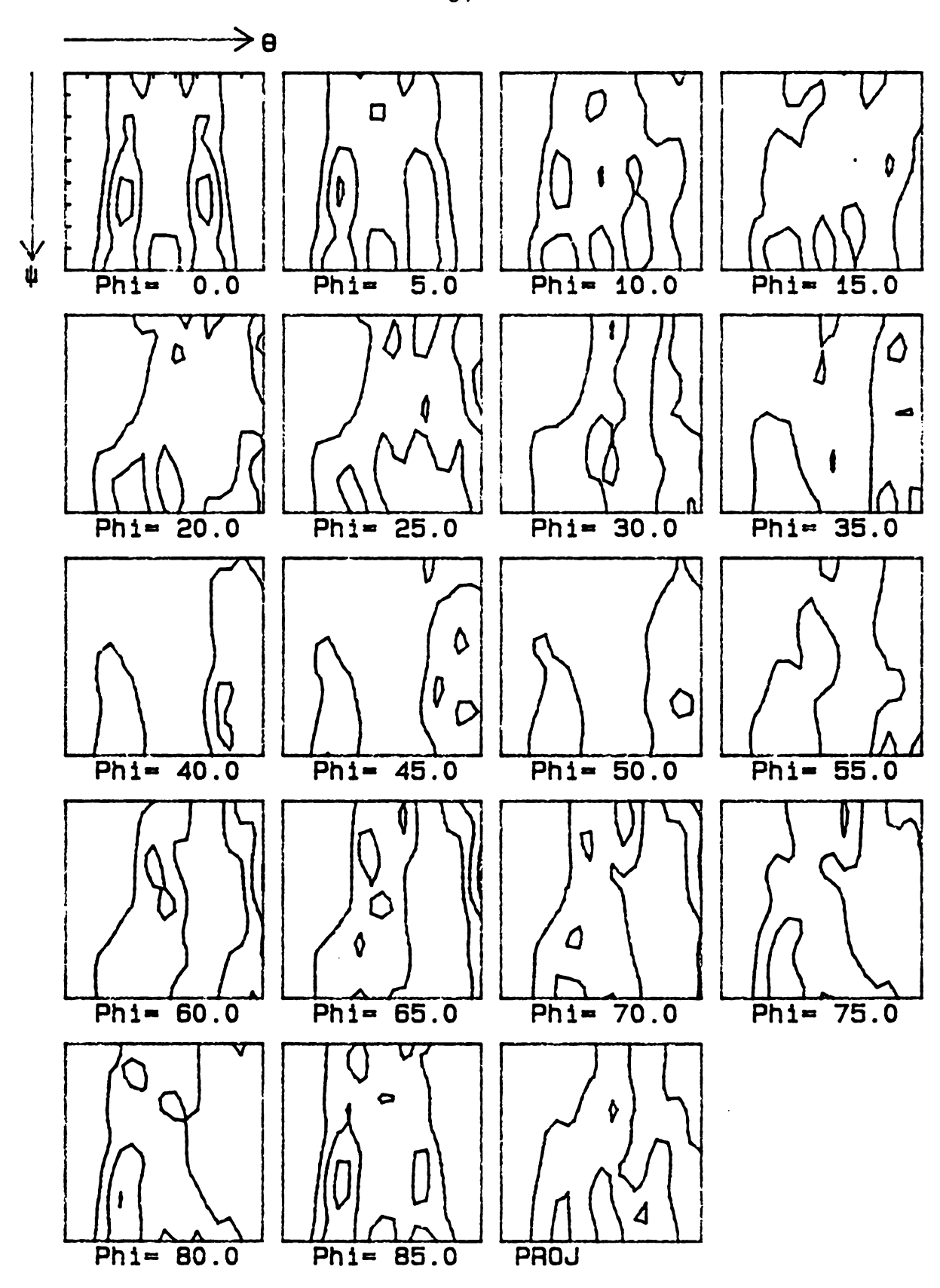
- (a) Undeformed Shoulder. The texture consists of three fiber textures: (101)[uvw] ( $\alpha$ -fiber texture), (102)[uvw] and (201)[uvw]. Since the latter two textures are symmetric about  $\theta$ =45° in the  $\Phi$ =0° section, only the components of (102)[uvw] texture will be considered below. In  $\alpha$ -fiber texture the maximum density is at (101)[101] orientation, but some other components also appear in the  $\Phi$ =0° section. No (001)[100] cube components exist in this initial texture, (Fig.3.3.a).
- (b) Texture at  $\varepsilon=1.1$ . A notable decrease in the  $\alpha$ -fiber texture is observed. The components  $(101)[\overline{13}1]$ ,  $(101)[\overline{12}1]$  and  $(101)[\overline{23}2]$  disappear. Slight changes occur in the (102)[uvw] fiber texture, though the density of most components is essentially unchanged, (Fig.3.3.b).
- (c) Texture at  $\varepsilon=1.6$ . At this strain, the  $\alpha$ -fiber becomes very smooth, that is, almost every component has the same density of about 1.5. The conponents between (101)[ $\overline{323}$ ] and (101)[ $\overline{101}$ ] continue to weaken from their initial intensities, but the rest of the components increase in intensity. In the (102)[uvw] fiber, the maximum



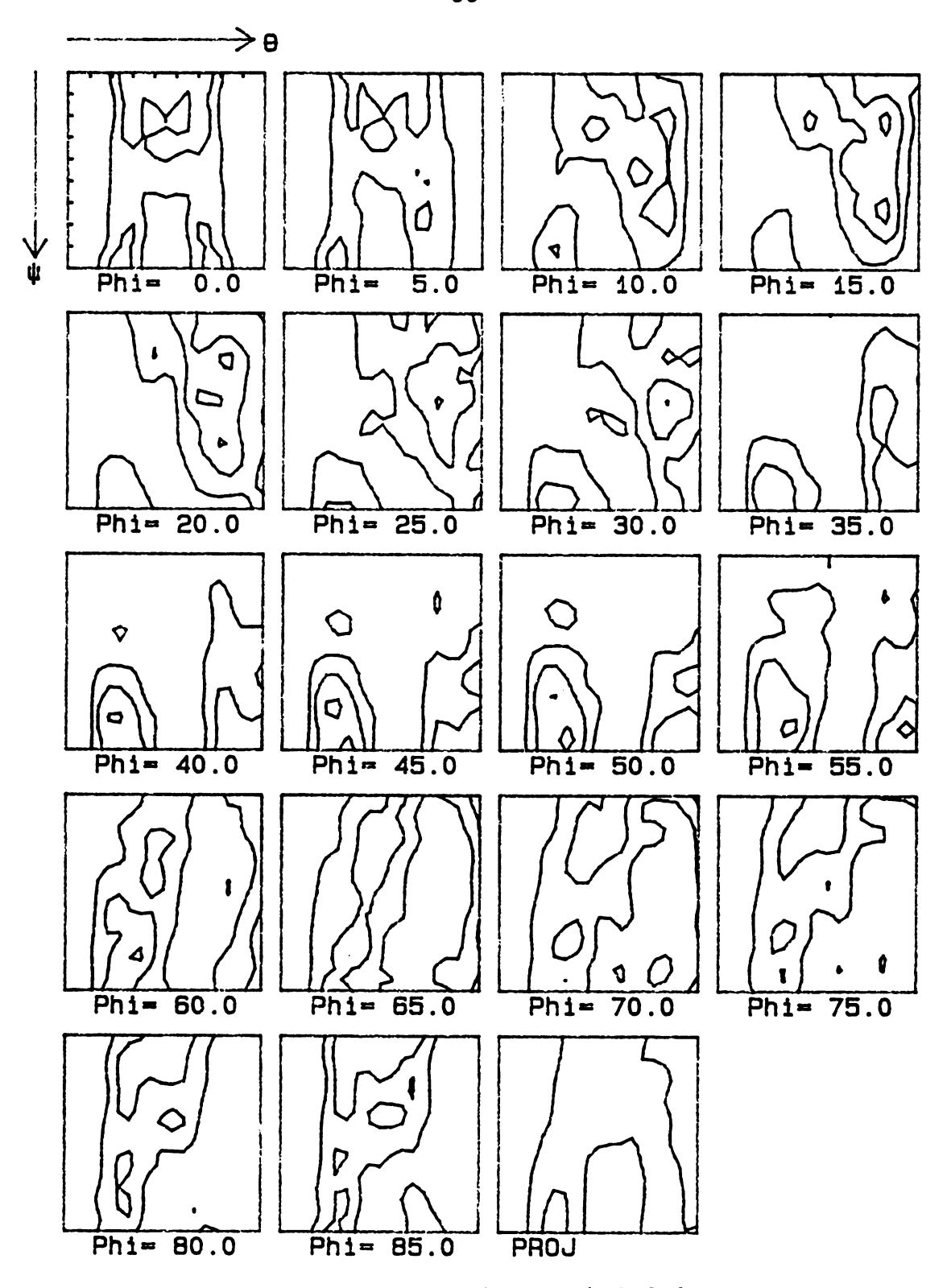
(a) Texture at  $\epsilon$ =0, contours at 1 2 3 4 Fig.3.2 Complete CODF of  $\dot{\epsilon}$ =1 sec<sup>-1</sup> and T=425°C (a)-(f).



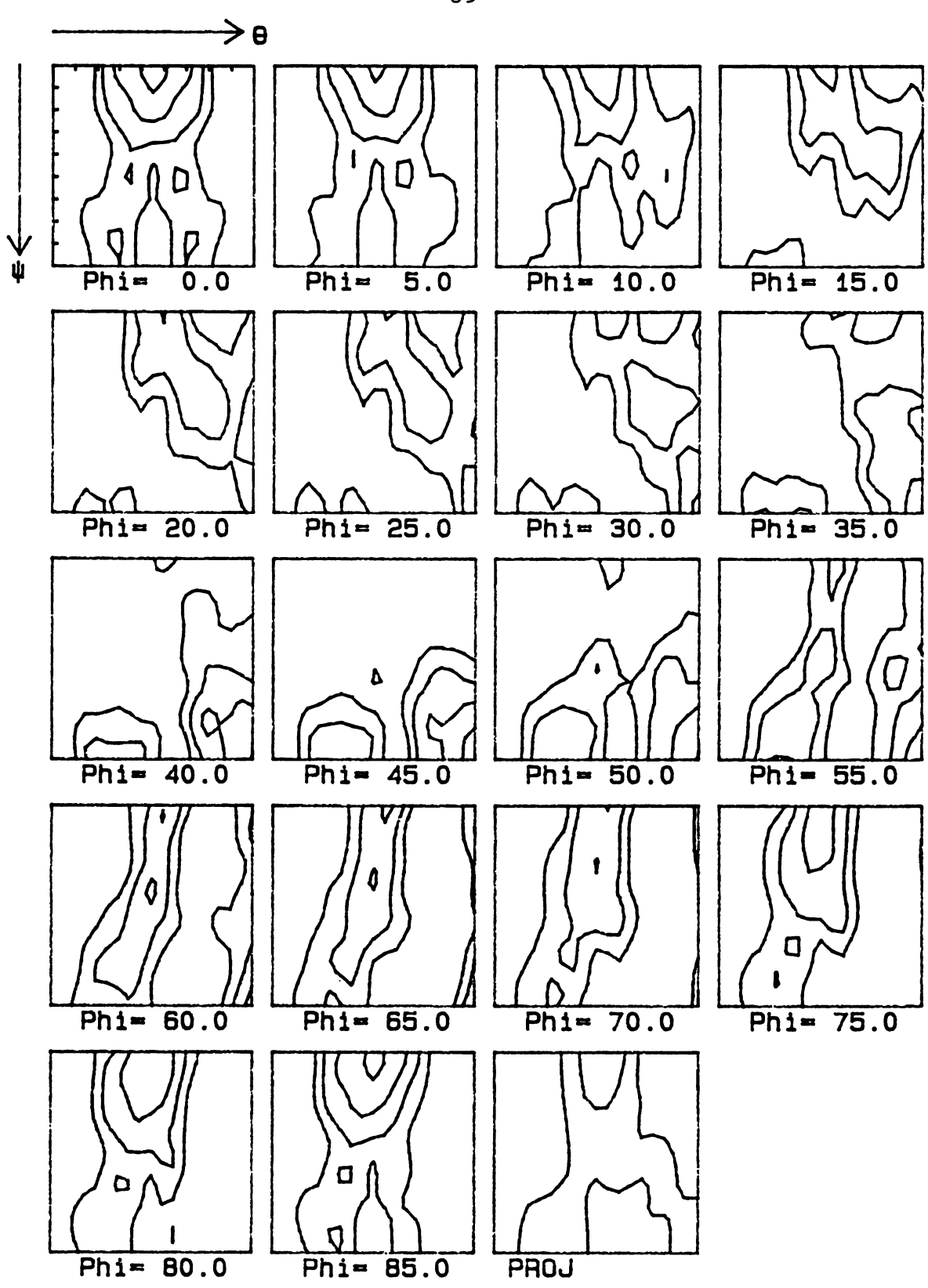
(b) Texture at  $\epsilon$ =1.1, contours at 1 2 3 4 5



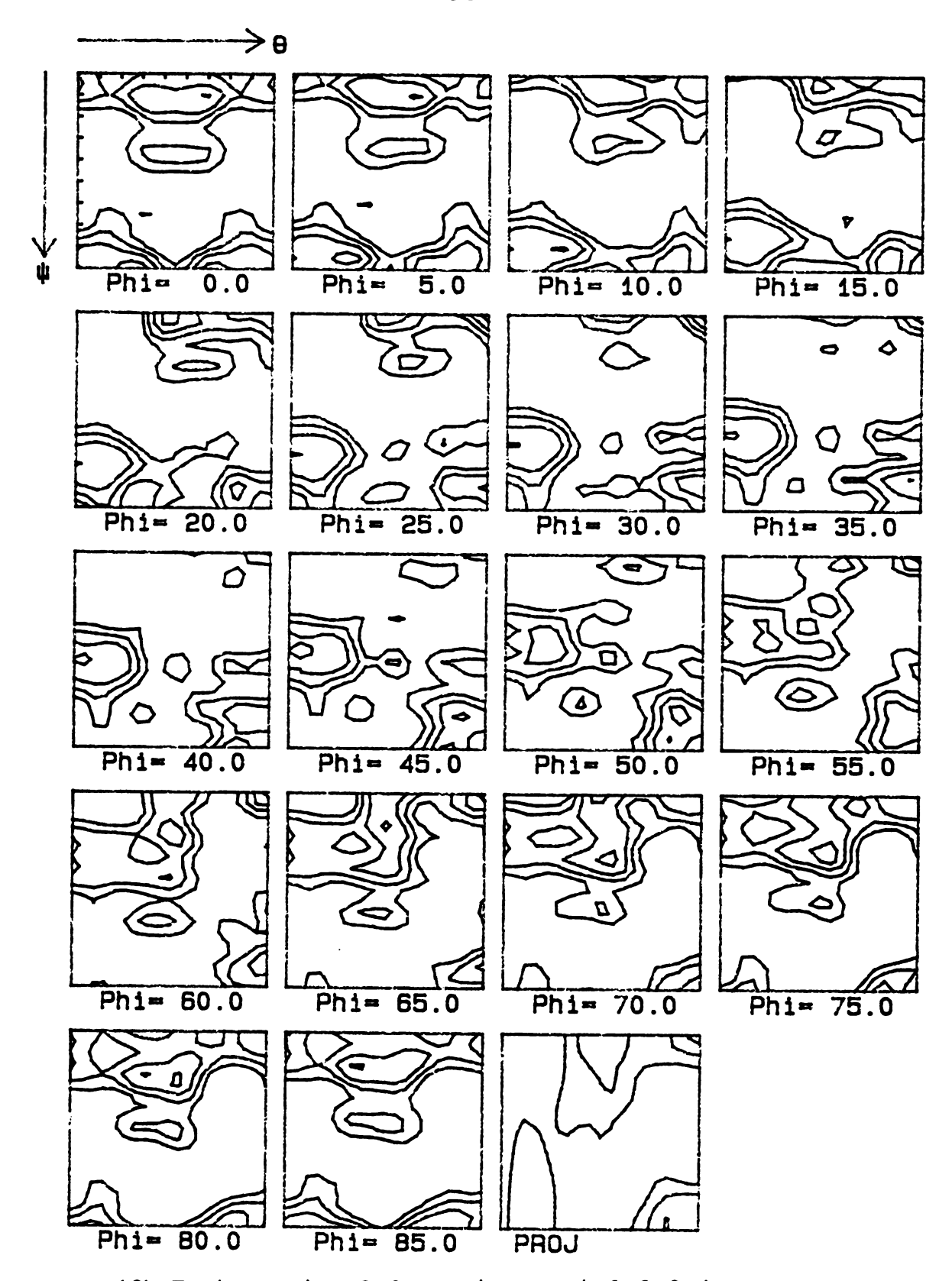
(c) Texture at  $\epsilon$ =1.6, contours at 1 2 3



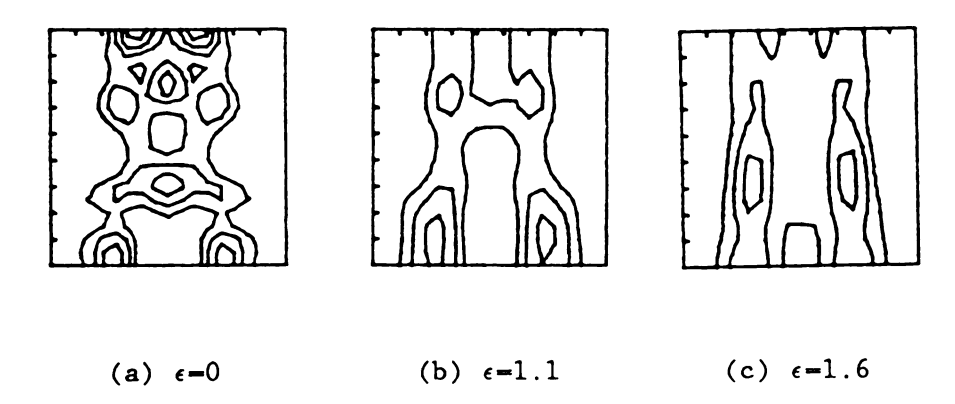
(d) Texture at  $\epsilon$ =2.3, contours at 1 2 3



(e) Texture at  $\epsilon$ =2.6, contours at 1 2 3 4



(f) Texture at  $\epsilon$ =3.0, contours at 1 2 3 4



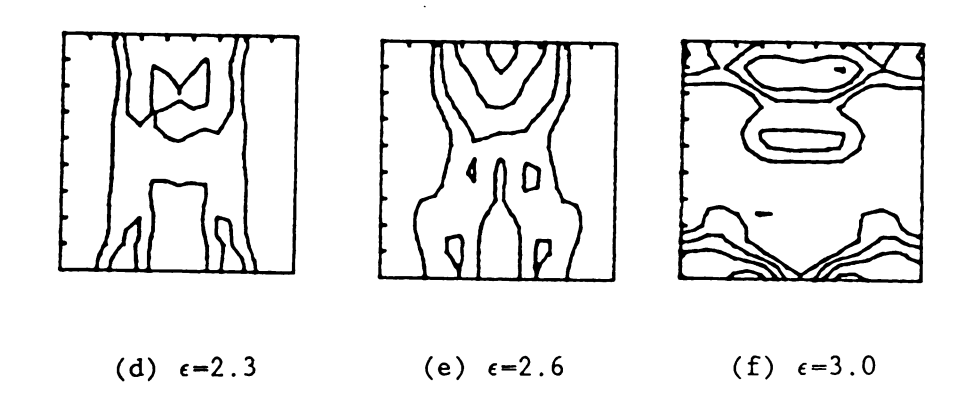


Fig.3.3 The  $\phi=0^{\circ}$  section of CODF vs strain.

intensity shifts slightly to  $(102)[2\overline{3}1]$  orientation. The peak  $(103)[0\overline{1}0]$  is weakened slightly. There is no evidence for development of a cube component, (Fig. 3.3.c).

- (d) Texture at  $\varepsilon=2.3$ . The components between  $(101)[\overline{23}2]$  and  $(101)[\overline{101}]$  in the  $\alpha$ -fiber sharpen, instead of reducing, compared to those at  $\varepsilon=1.6$ , but  $(101)[\overline{13}1]$  and  $(101)[\overline{12}1]$  are reduced further. The overall intensity of (102)[uvw] fiber declines and the highest intensity continues to shift to a lower  $\Psi$  angle, (Fig. 3.3.d).
- (e) Texture at  $\epsilon$ =2.6. The  $\alpha$ -fiber continues to sharpen, and the intensities of components at the lower  $\Psi$  angle also increase. For the (102)[uvw] fiber, the highest intensity continues to shift to lower  $\Psi$  angle so that only (102)[ $\overline{2}$ 01] component is sharpening drastically while other components weaken slightly or remain unchanged. A considerable sharpening is noted at the (203)[ $\overline{3}$ 02] peak, but there is still no evidence for cube texture development, (Fig.3.3.e).
- (f) Texture at  $\varepsilon=3.0$ . Near the fracture tip, a new fiber (h01)[010] has developed considerably, while the other components among the previous fibers are weakened. A strong cube texture emerges at this point, (Fig.3.3.f).

To summarize, some of the changes in texture described above are plotted as a function of  $\Psi$  and strain in Figure 3.4.

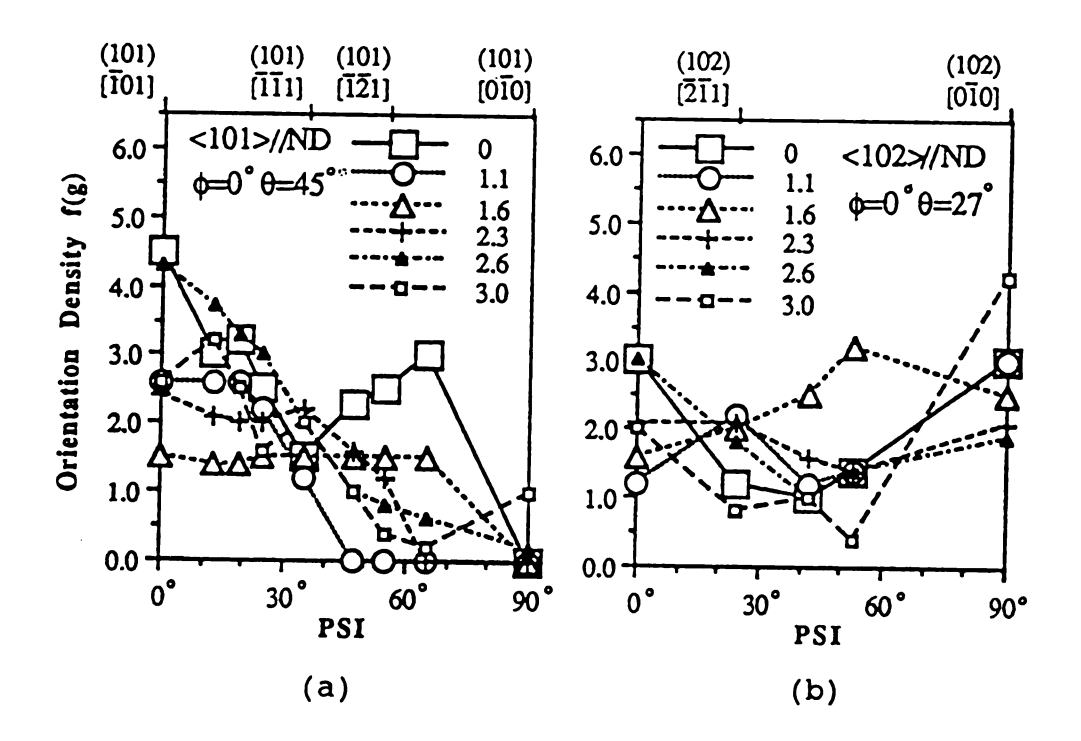


Fig.3.4 Orientation density vs.  $\Psi$  and strain

## 3.2. Specimen Deformed at $\dot{\epsilon}=77/\text{sec}$ and T=475°C

For the specimem deformed at a strain rate  $\dot{\epsilon}=77/\text{sec}$  and a temperature T=475°C, we are mainly considering the fiber type texture in  $\Phi=0$ ° section of the CODF and some specific peak type components in the sections from the whole range of  $\Phi$ . The complete experimental CODFs of this specimen are shown in Fig 3.5.

(a) Undeformed Shoulder. In Φ=0° section, it mainly consists of three fiber textures: (101)[uvw], (102)[uvw] and (201)[uvw], which is similar to those of undeformed specimen in previous section 3.1. Here again, we are going

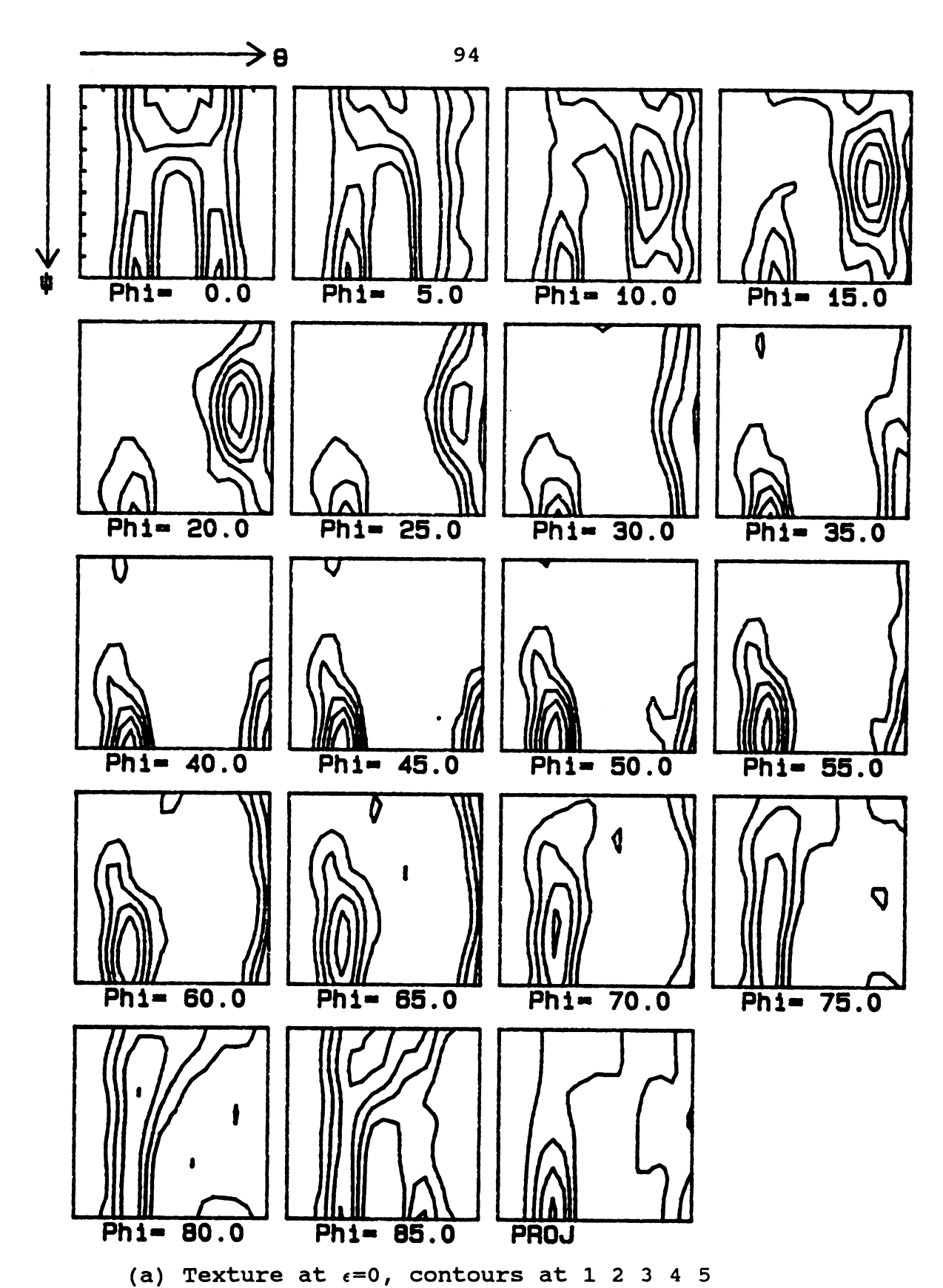
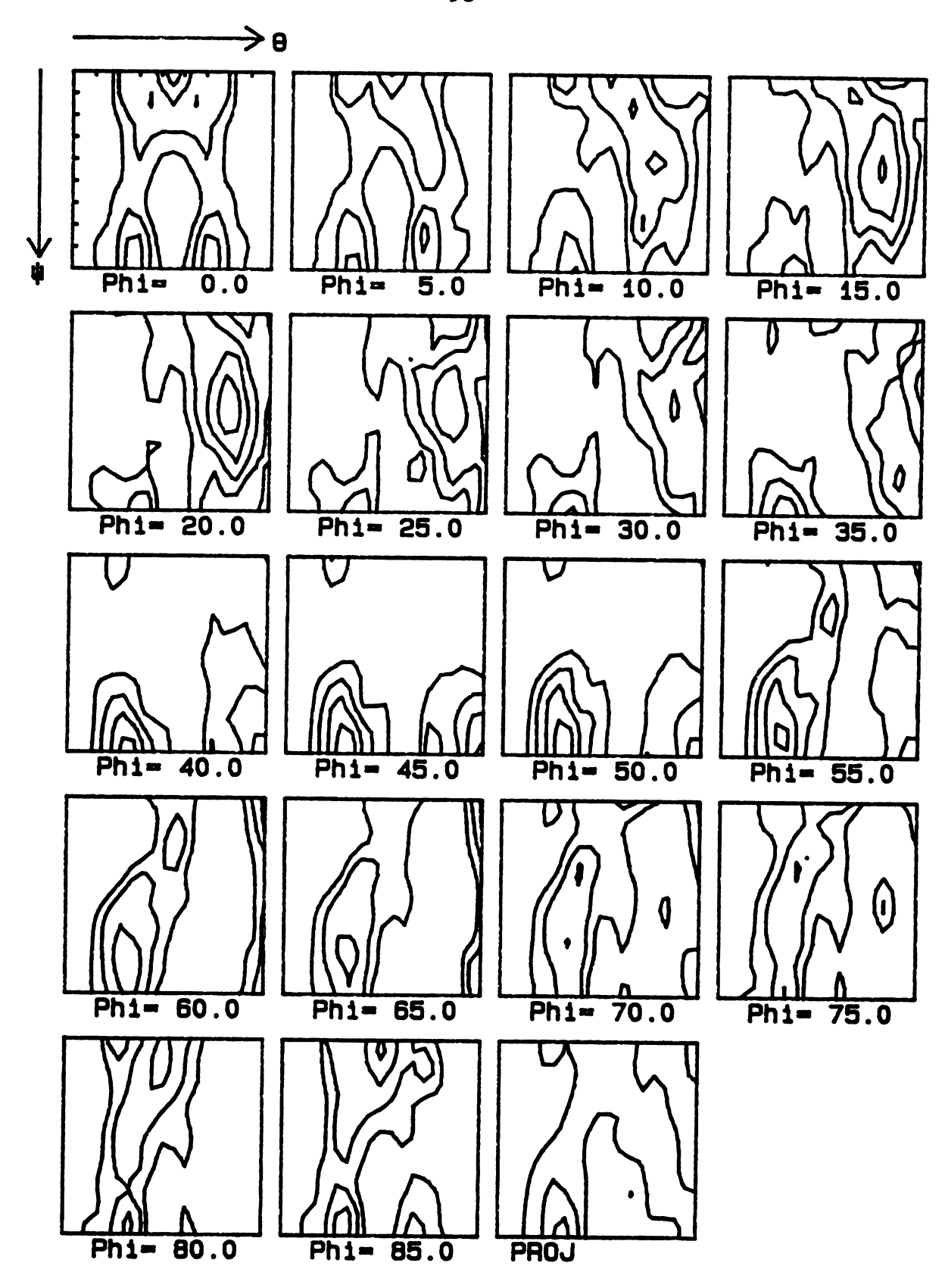
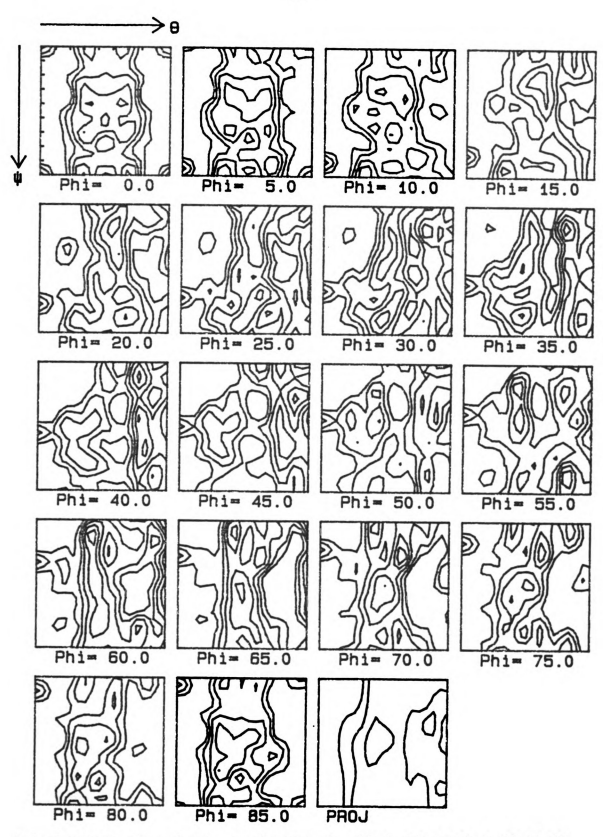


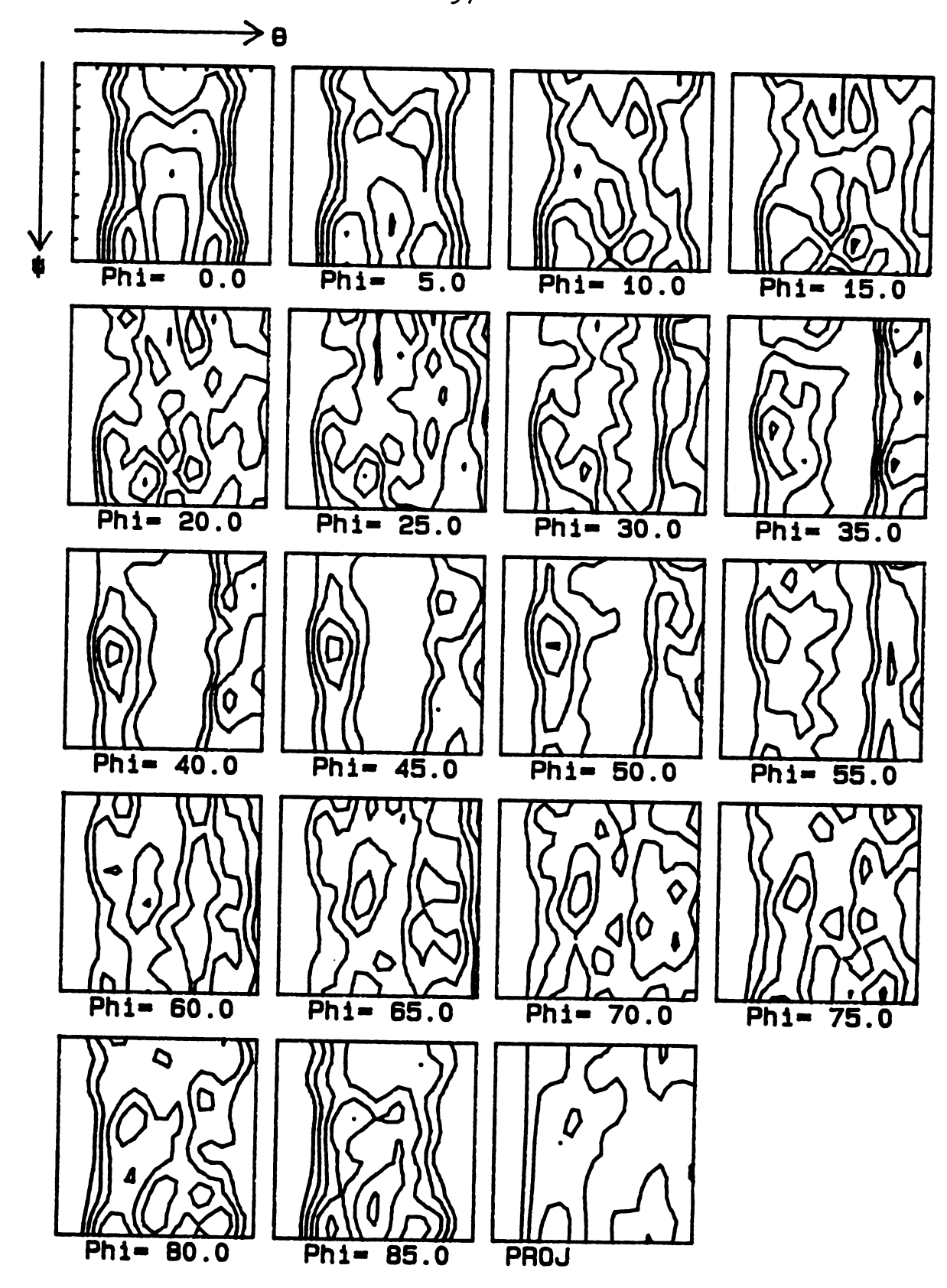
Fig.3.5 Complete CODF of  $\dot{\epsilon}=77~\text{sec}^{-1}$  and T=475°C (a)-(e).



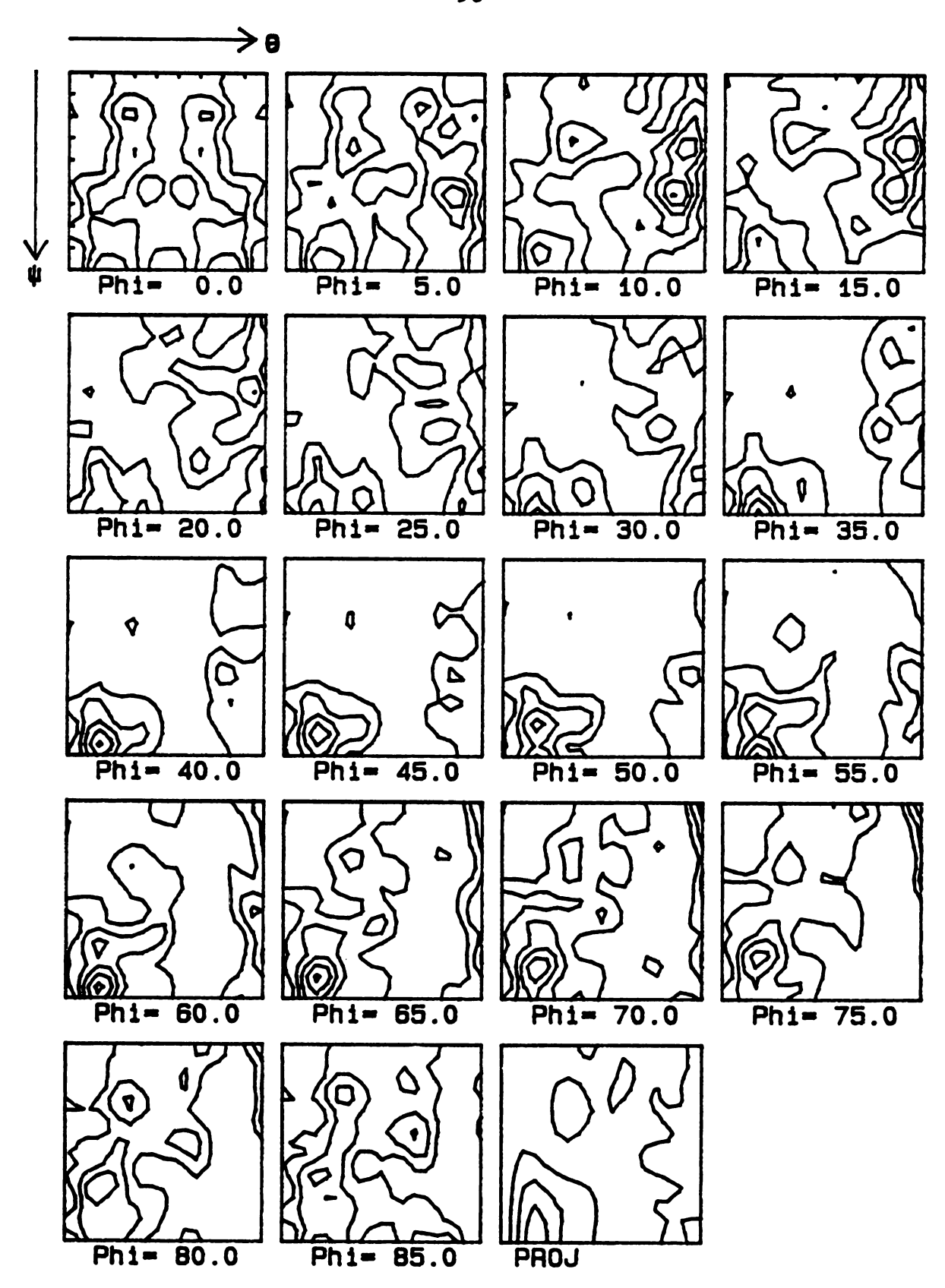
(b) Texture at  $\epsilon$ =1.6, contours at 1 2 3 4



(c) Texture at  $\epsilon$ =2.13, contours at .50 1.00 1.50 2.00 2.50



(d) Texture at  $\epsilon$ =2.36, contours at .50 1.00 1.50 2.00 2.50



(e) Texture at  $\epsilon$ =2.86, contours at 1 2 3 4 5

to consider only the components of (102) [uvw] since the components of (102) [uvw] and (201) [uvw] are symmetric about  $\theta$ =45° in  $\Phi$ =0° section. In  $\alpha$ -fiber texture, intensity declines gradually with a maximum intensity at (101) [ $\overline{1}01$ ] and the intensities from (101) [ $\overline{2}\overline{3}2$ ] to (101) [ $0\overline{1}0$ ] are zero. There are very high intensities at (203) [ $\overline{3}02$ ] and (311) [ $0\overline{1}1$ ]. But there is no cube texture, (Fig. 3.5.a).

- (b) Texture at  $\varepsilon=1.6$ . The components of the fiber texture and peak type texture at this point remain unchange compared to the initial texture from the undeformed shoulder, but the overall intensity is weakened, (Fig.3.5.b).
- (c) Texture at  $\varepsilon=2.13$ . At this point, the intensities of texture (102)[uvw] and peak (203)[ $\overline{3}$ 02] continue decreasing, but in the texture (101)[uvw], the components from (101)[ $\overline{0}$ 10] to (101)[ $\overline{2}$ 32] which were zero in intensity at lower strain are sharpened considerably and the previous high intensity components from (101)[ $\overline{1}$ 11] to (101)[ $\overline{1}$ 01] are weakened drastically. So the highest intensities shift to the [010],[ $\overline{1}$ 21] and [ $\overline{1}$ 11] directions in this fiber. Several new peaks are noted, developing at (312)[ $\overline{1}$ 12],(321)[ $\overline{1}$ 4 11], (231)[ $\overline{1}$ 31],(123)[ $\overline{1}$ 43] and (132)[ $\overline{1}$ 34]. Meanwhile, a cube texture is also developed, (see Fig.3.5.c).
- (d) Texture at  $\varepsilon$ =2.36. The intensities of texture (102) [uvw] are sharpened but the intensities of (101) [uvw]

are noted to be weakened except for peak (101)[11]. The cube texture disappears again. The formerly developed (321)[1 4 11] is shifted to (321)[2 3 12] and a new peak (321)[121] is developing, while the formerly present peaks (312)[112], (231)[431], (123)[143] and (132)[134] are weakened. It is also noted that a new fiber texture (113)[uvw] is developed with a maximum intensity at peak (113)[031], (see Fig.3.5.d).

(e) Texture at  $\varepsilon=2.86$ . The intensities of (102)[uvw] continue increasing with a maximum intensity at  $(102)[0\bar{1}0]$ , and overall intensity of (101)[uvw] continues decreasing. A new orientation  $<0\bar{2}3>//RD$ , such as  $(11\ 2\ 3)[0\bar{3}2]$ ,  $(12\ 3\ 2)[0\bar{2}3]$ ,  $(823)[0\bar{3}2]$ ,  $(3\ 2\ 11)[2\bar{3}0]$  and  $(3\ 2\ 12)[2\bar{3}0]$ , is strongly developed even though the peak  $(203)[\bar{3}02]$  reachs minimum intensity compared to that at lower strain. New strong peaks  $(611)[\bar{1}\ \bar{6}\ 12]$  and  $(116)[\bar{6}\ \bar{12}\ 1]$  are also created. The overall intensity of texture at this point increased markedly to reach the initial intensity, (Fig.3.5.e).

In order to compare the results with the former specimen, the texture changes in  $\alpha$ -fiber texture and (102)[uvw] texture are plotted in Fig.3.6.

3.3 Specimen Deformed at  $\dot{\epsilon}$ =330/sec and T=475°C

The complete experimental CODFs of this specimen are

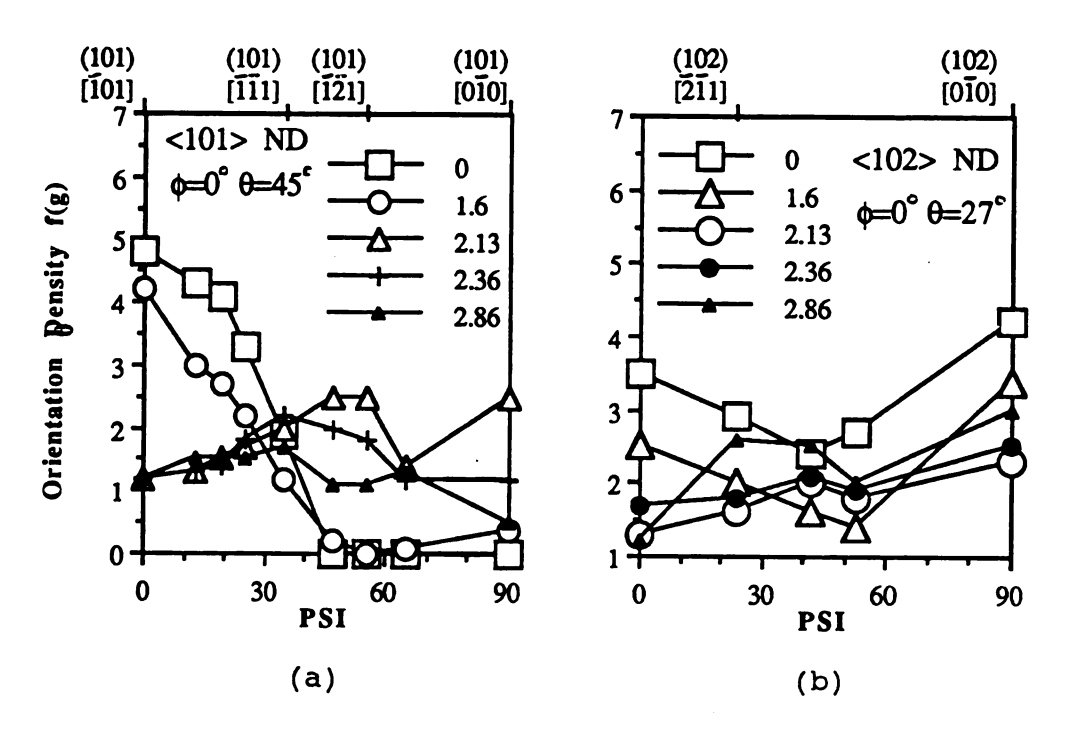


Fig.3.6 Orientation density vs.  $\Psi$  and strain

shown in Fig.3.7. In this specimen, two fiber texture, which are different from those in other two specimens, are found: one is (203) [uvw] and the other is a skeleton line in which the [001] orientation is tilted from ND by about  $30^{\circ}$  towards TD. The results are ploted in Fig.3.8. The overall intensity of skeleton line keeps constant until the  $\varepsilon$ =1.38, where the some parts of the skeleton line are sharpened slightly. But the overall intensity of the fiber (203) [uvw] decreases with strain increasing.

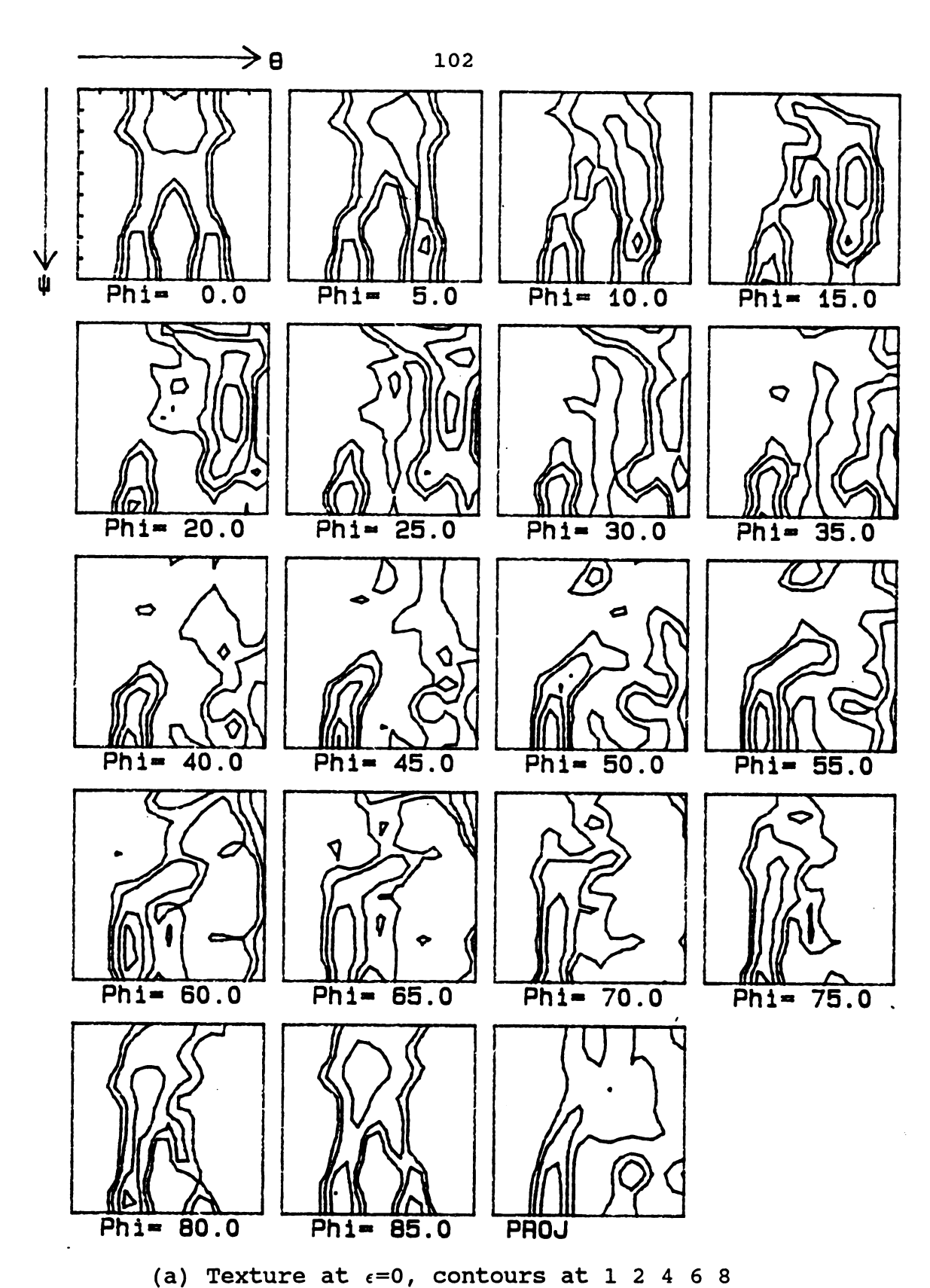
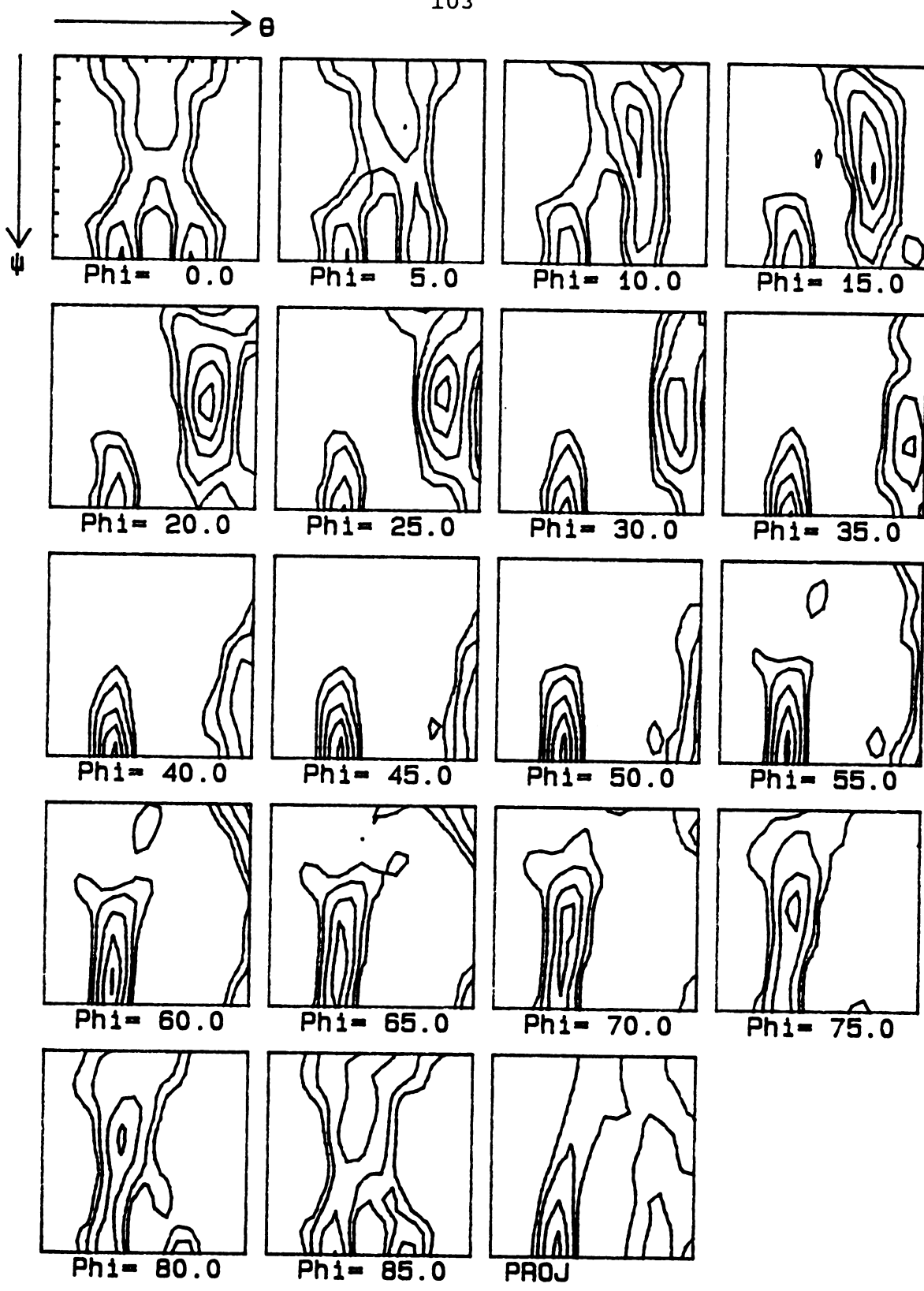
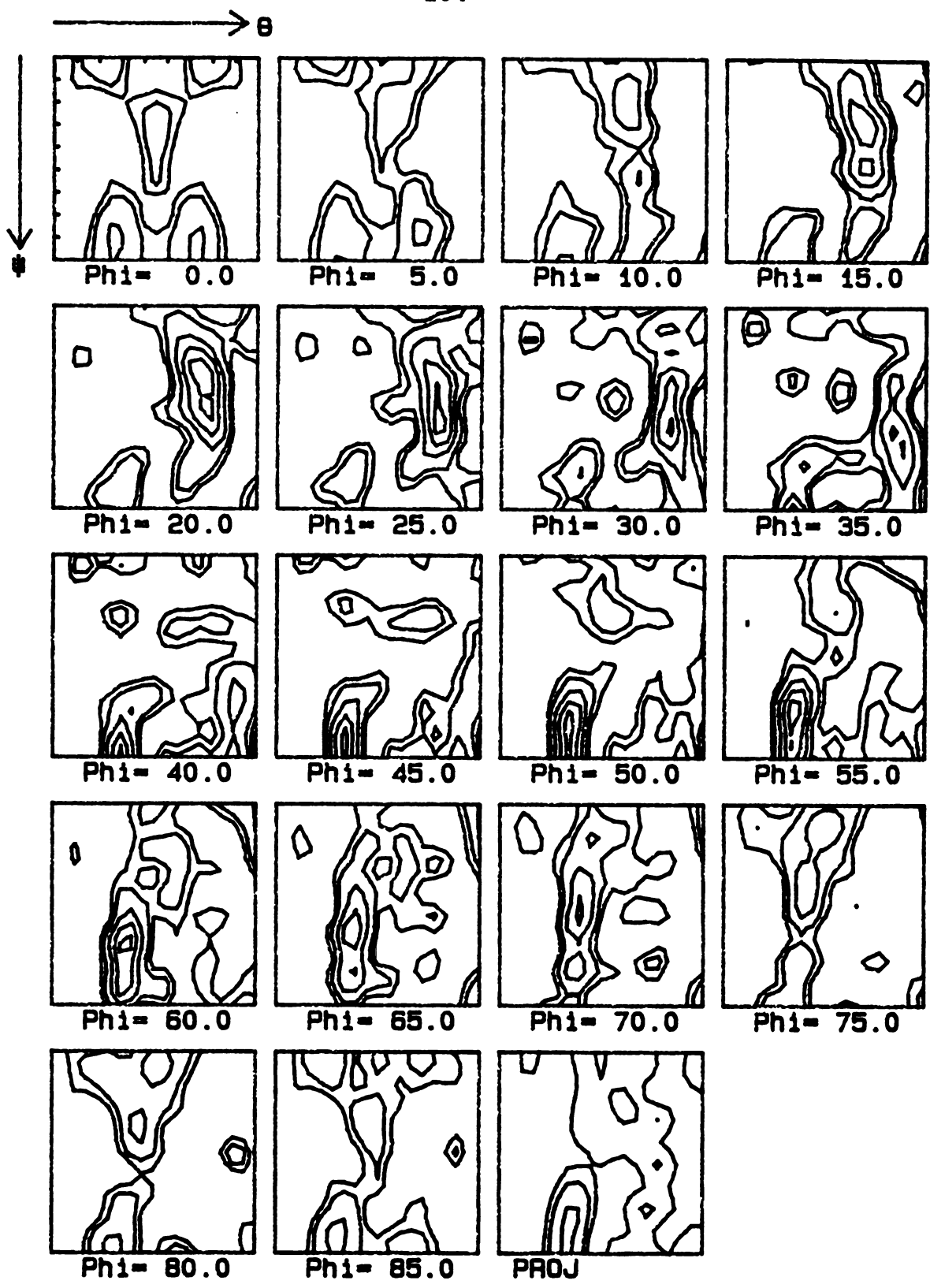


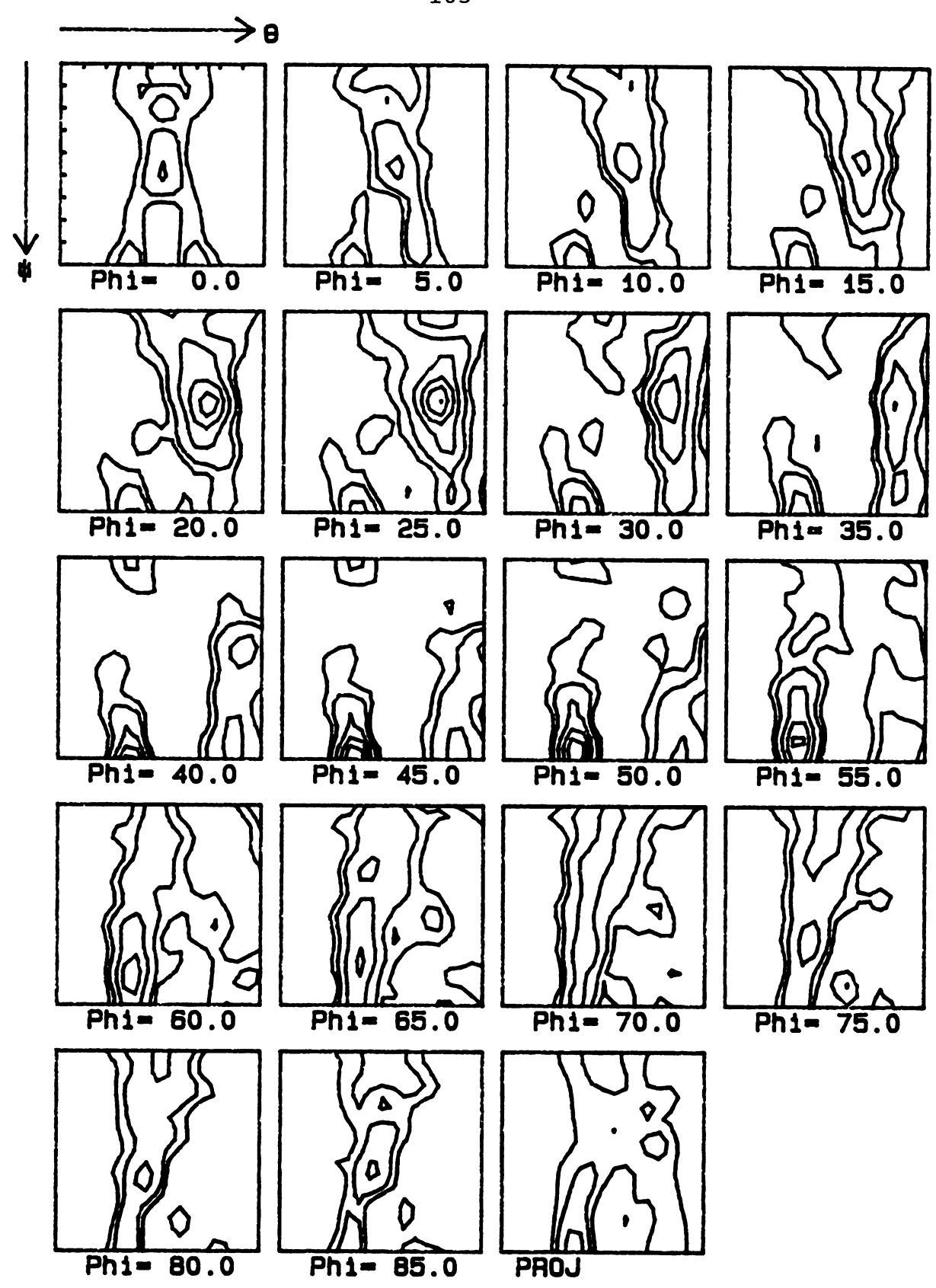
Fig.3.7 Complete CODF of  $\dot{\epsilon}$ =330 sec<sup>-1</sup> and T=475°C (a)-(d).



(b) Texture at  $\epsilon$ =0.45, contours at 1 2 4 6 8



(c) Texture at  $\epsilon$ =0.73, contours at 1 2 4 6 8



(d) Texture at  $\epsilon$ =1.38, contours at 1 2 4 6 8 10

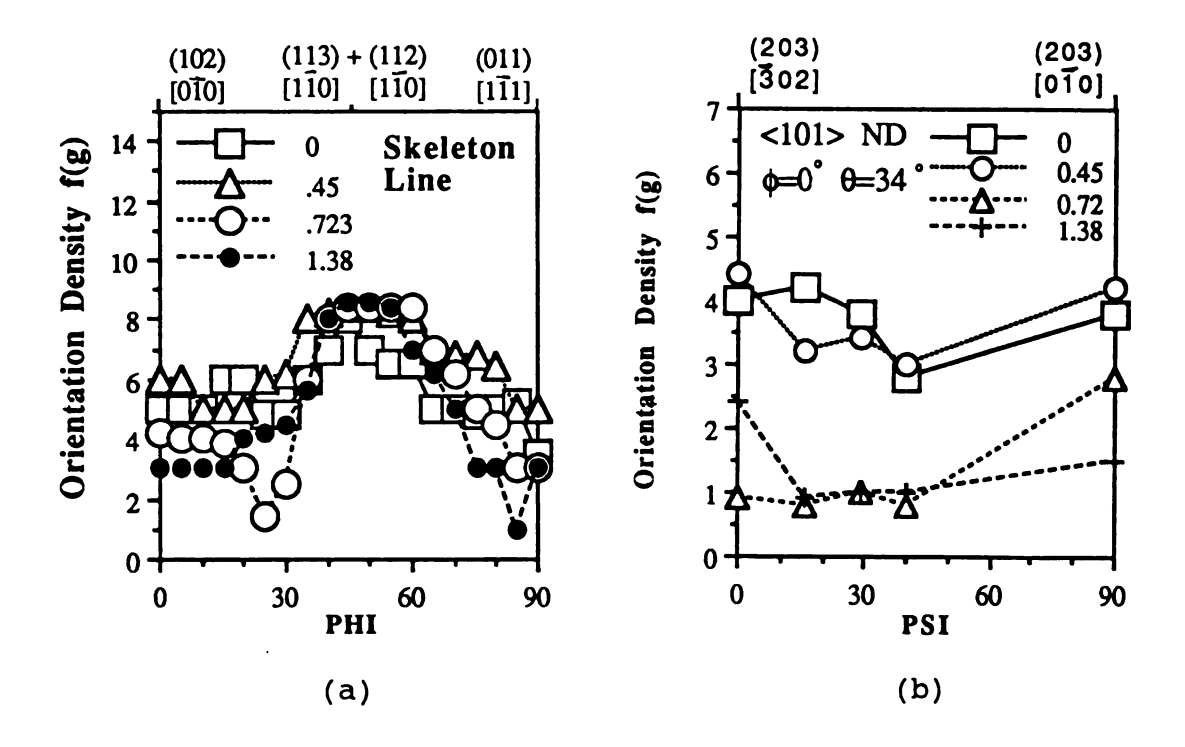


Fig.3.8 Orientation density vs.  $\Psi$  and strain

#### CHAPTER 4

#### ANALYSIS AND DISCUSSION

# 4.1. Deformation at Relatively Lower Superplastic Strain Rate

The specimens deformed at strain rate  $i=1/\sec$  and  $i=77/\sec$  are mainly composed of two fiber textures, with <101> and <102> directions parallel to the rolling plane normal, and some individual peaks. During the superplastic deformation, two fiber textures dominate the texture components, even though the intensities of individual components in these fibers change with strain. The texture changes produced by superplastic deformation can be described in terms of grain boundary sliding, slip and dynamic recrystallization.

#### 4.1.1. Grain Boundary sliding.

In Fig.4.1 some ideal components are plotted vs. strain. It is noted that the overall texture intensity with strain up to  $\varepsilon$ =2.6 in the first specimen and strain up to  $\varepsilon$ =2.13 in the second specimen decrease. The texture decline in superplastic deformation can not be explained in terms of slip or recrystallization, because annealing is found to lead to only a slight or no reduction in intensity and

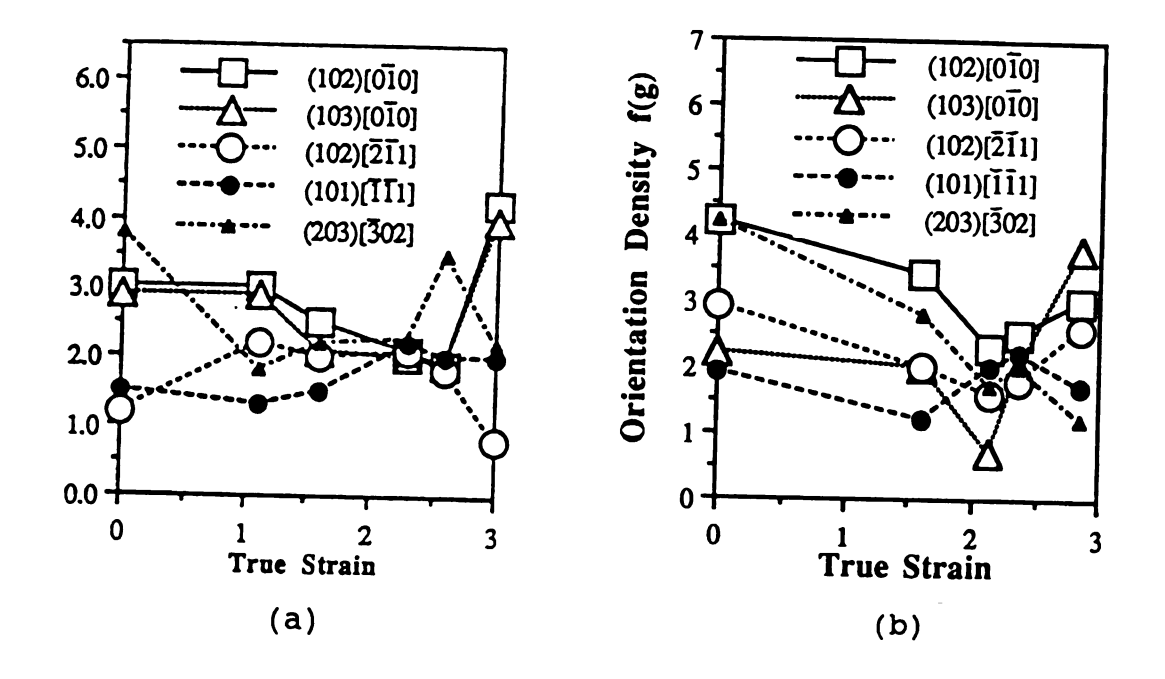


Fig. 4.1 Texture components vs. true strain

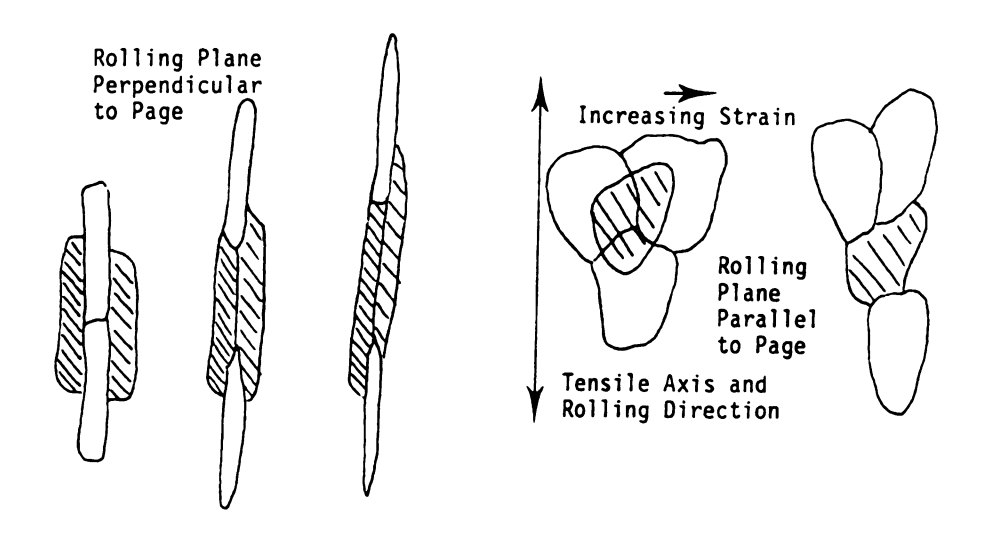


Fig.4.2 Schematic diagram showing sliding of platelet-shaped grains during superplastic elongation.

recrystallization leads to the development of new and distinct texture components. However, this overall reduction can be easily accounted for in terms of grain boundary sliding and grain rotation. The mechanism of GBS is schematically shown in Fig. 4.2 [154]. Because the grain aspect ratio is about 1 to 8, the sliding in the direction perpendicular to the plane of the grain is difficult. The GBS and grain rotation take place in the plane parallel to the rolling plane, and the grains remain in the same plane as they started. It is proposed that grain boundary sliding and grain rotation have a randomizing effect on any existing texture components<sup>[138,139,155,156,]</sup>. However, the randomizing effect of GBS and rotation in these specimens is restricted in the direction perpendicular to the rolling plane due to the plate shape grains. Therefore, the sliding stresses on the different types of boundaries are accommodated by either grain rotation in the rolling plane or dislocation slip in grain interiors, as show in Fig.4.2.b. The relatively slow reduction of overall texture implies that the grain rotation rate is limited. SEM and TEM studies show that GBS and rotation are limited to an axis normal to the rolling plane [154]. But it is difficult to make a quantitative assessment of its contribution to an individual orientation, since there are varying concurrent sharpening and weakening of existing texture components due to the occurrence of slip and recrystallization.

4.1.2. Slip.

Investigation of the [211] orientation in Fig.4.1 shows the occurrence of single slip during superplastic deformation. In Fig.4.1.a, high indensity of [21] orientation is in the range of lower strain, and intensities drop considerably close to the fracture surface. However, in Fig. 4.1.b, the intensity of [21] orientation continues to increase after an initial drop of overall intensity due to GBS and rotation. It is possible to treat a grain as a isotated single crystal in uniaxial tension in the case of diffusion accommodated superplastic deformation, so that the single slip allows the grain to rotate to <121> direction where the second slip system operates and keeps the grain at <121>. Furthermore, <121> orientations have a relatively high Schmid factor (0.41) and thus slip is possible in grains at or near these orientation [123]. The sharpening of the  $[\bar{2}\bar{1}1]$  orientation indicates that a large amount of single slip has occurred. The reduction of the  $\lceil \overline{2} \overline{1} 1 \rceil$  orientation with further strain may be attributed to an increase of the number of multiple slips and an occurrence of dynamic recrystallization. The increment of  $[\overline{211}]$  orientation with strain in Fig.4.1.b indicates more single slip occurring at high strain. Such an orientation is stable in the sense that any rotation away from it occasioned by grain boundary sliding leads to a Counteracting slip rotation back towards <121>.

The gradual increase of a [11] orientation suggests that multiple slip occurs in this specimen because the <111> texture is commonly associated with multiple slip under uniaxial tension in polycrystalline materials [149]. The <111> texture is stable during multiple slip, because only five of the six active slip system in this orientation are required to maintain grain compatibility and the remaining one degree of freedom allows a rotation of the grains about the tensile axis only [148].

There are strong <100> components in the starting materials, compared to the other texture components, but <100> texture gradually declines up to  $\varepsilon$ =2.6 at lower strain rate (see Fig.4.1.a) and  $\varepsilon$ =2.13 at  $\dot{\varepsilon}$ =77/sec (see Fig.4.1.b). This is because the <100> orientation has eight active slip system so that after providing five slip systems for grain compatibility, the grain slill has three degrees of freedom and any rotation is possible [148]. Close to the fracture surface in the specimen deformed at  $\dot{\epsilon}$ =1/sec, where neck formation and a rising local temperature take place, and the higher strain in the specimen deformed at  $\dot{\epsilon}=77/\text{sec}$ , the slip system shifts from <111> to <100> directions. It may be possible since the <100> orientation is more likely to operate with strain increasing in this material and the grain compatibility can be more strongly assisted by diffusional processes due to the adiabatic thermal effect. In this case the deformation

in each grain is more like that of an isolated single crystal in uniaxial tension<sup>[150]</sup>. Further, the Schmid factors for the <100> and <111> orientations are 0.408 and 0.272, respectively. This leads to increasing intensity in <100> orientation.

### 4.1.3. Recrystallization.

The appearance of cube texture at the highest strain in the specimen deformed at 1/sec and at the median strain in the specimen deformed at 77/sec suggests that recrystallization occurs. The small amount of cube texture is possibly due to the effects of the finely dispersed particles and fine substructures. Local lattice rotations are found at the large particles and the regions near the particles rotate in the opposite sense to the matrix about the same axis. The deformation zone at the particles is a preferred nucleation site for recrystallization. Therefore, the contribution of the particles to the overall texture is expected to be a smearing out of the deformation texture by an amount which depends on the volume fraction of particles present [157-161]. But for small particles  $(<0.1\mu\text{m})$ , some studies have shown that the texture is strengthened whereas in other cases a neutral or a weakening effect has been observed [162-164]. In this study. Because the particle size is very small (13.7nm) and the spacing between the particles is 40nm, the particles have

such a strong pinning effect on both substructures and grain boundaries that subgrains are very difficut to grow to a recrystallizing nucleus. So it requires large enough strain to overcome this barrier for recrystallization.

The overall initial texture is retained after superplastic deformation and dynamic recrystallization, although the amounts of the different texture components may be altered. This is in agreement with Humphreys and Jensen's investigation<sup>[165]</sup>. This results may be also related to an effect of particles on the formation of dynamic recrystallization nuclei which may take place at the original high angle boundaries<sup>[166]</sup>. The nucleation process is retarded by presence of small particles reducing the rate of subgrain growth. This retarding effect may be least pronounced at the original grain boundaries where nucleation may require less subgrain growth than nucleation in the grain interiors. The preference for nucleation at the original grain boundaries may lead to an increased retention of the initial texture<sup>[64,167]</sup>.

## 4.2. Deformation at High Strain Rate

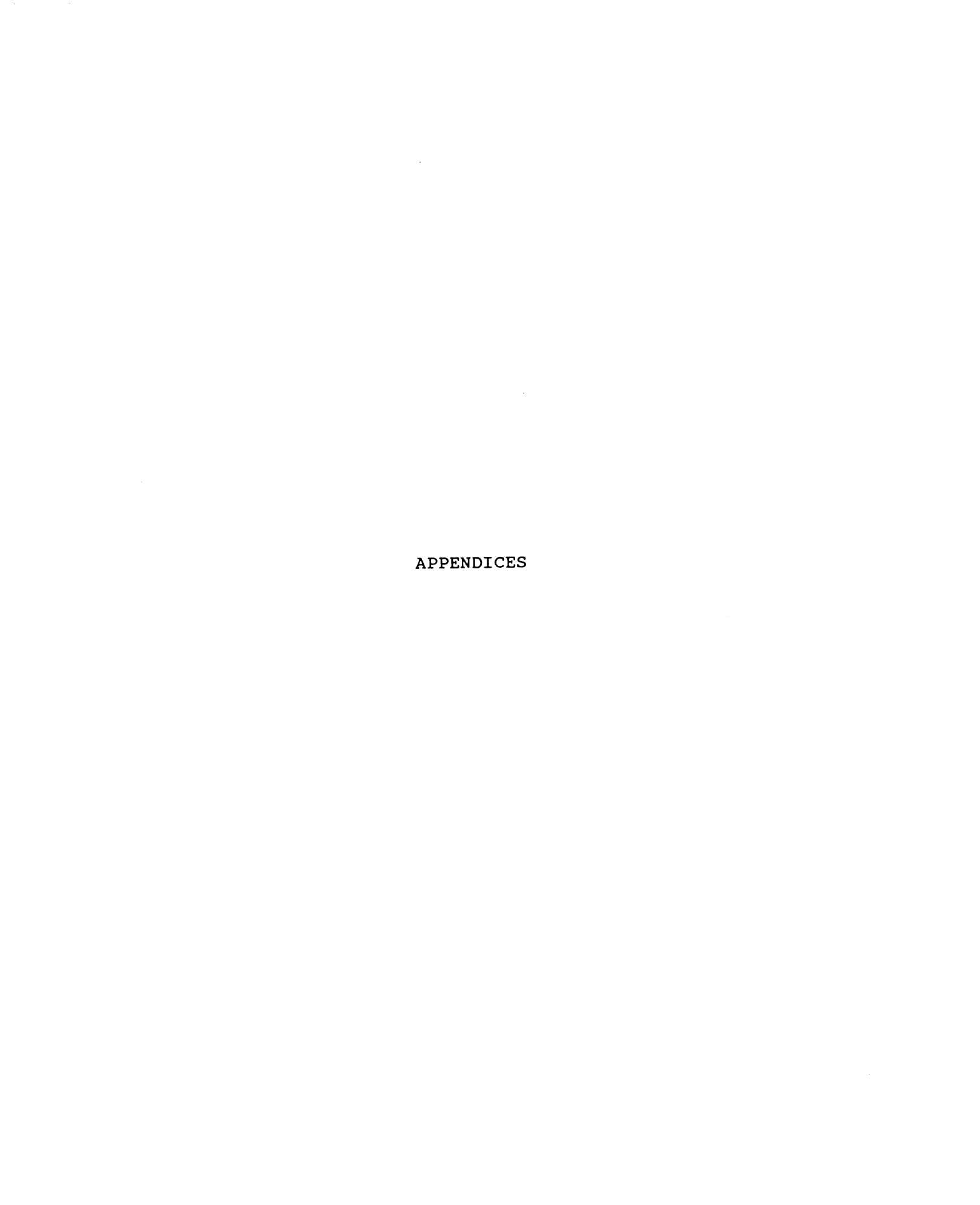
The specimen deformed at strain rate  $\dot{\epsilon}=330/\text{sec}$  mainly consists of one skeleton fiber texture which runs from (102)[010] to (011)[111]. Contrary to the overall reduction of intensity in the superplastically deformed specimen, the overall intensity in this specimen keeps constant.

Therefore, it indicates that there should be a some kind of balance between sharpening and weakening effects due to slip, recrystallization, GBS and rotation. In this specimen, components of (102)[010] and (001)[111] decrease in intensity with strain while the intensities of (113)[110] and (112)[110] components increase as strain increases. This result is contrary to the traditional deformation mechanism which predicts an increment of <001> and <111> orientations by tensile deformation. It indicates that a different deformation mechanism is occurring in this case.

#### CHAPTER 5

#### CONCLUSIONS

- 1. Texture is a very powerful structure parameter to study the deformation behaviors. It can isolate the individual contributions from the various mechanisms, such as dislocation slip, twinning, grain boundary sliding, grain rotation and recrystallization.
- 2. The superplastic deformation mechanism of IN90211 consists of grain boundary sliding, dislocation slip (sigle slip and multiple slip), grain ratation and recrystallization. But at the highest strain rate, there is no evidence of recrystallization.
- 3. At the lower strain rates (1/sec and 77/sec), the textures are mainly two fibres,  $\alpha$ -fibre (<101> parallel to ND) and {102}<uvw> (<102> parallel to ND). At the highest strain rate (330/sec), the textures are mainly composed of two fibres, {203}<uvw> (<203> parallel to ND) and a skeleton line (<001> orientation is tilted from ND towards TD by about 30°).



## APPENDIX A POLE FIGURES OF IN90211

Fig. A.1 (111), (200), (220) pole figures of specimen deformed at  $\dot{\epsilon}=1/\text{sec}$  and T=425°C.

Fig. A.2 (111), (200), (220) pole figures of specimen deformed at  $\dot{\epsilon}=77/\text{sec}$  and T=475°C.

Fig. A.3 (111), (200), (220) pole figures of specimen deformed at  $\dot{\epsilon}=330/\text{sec}$  and T=475°C.

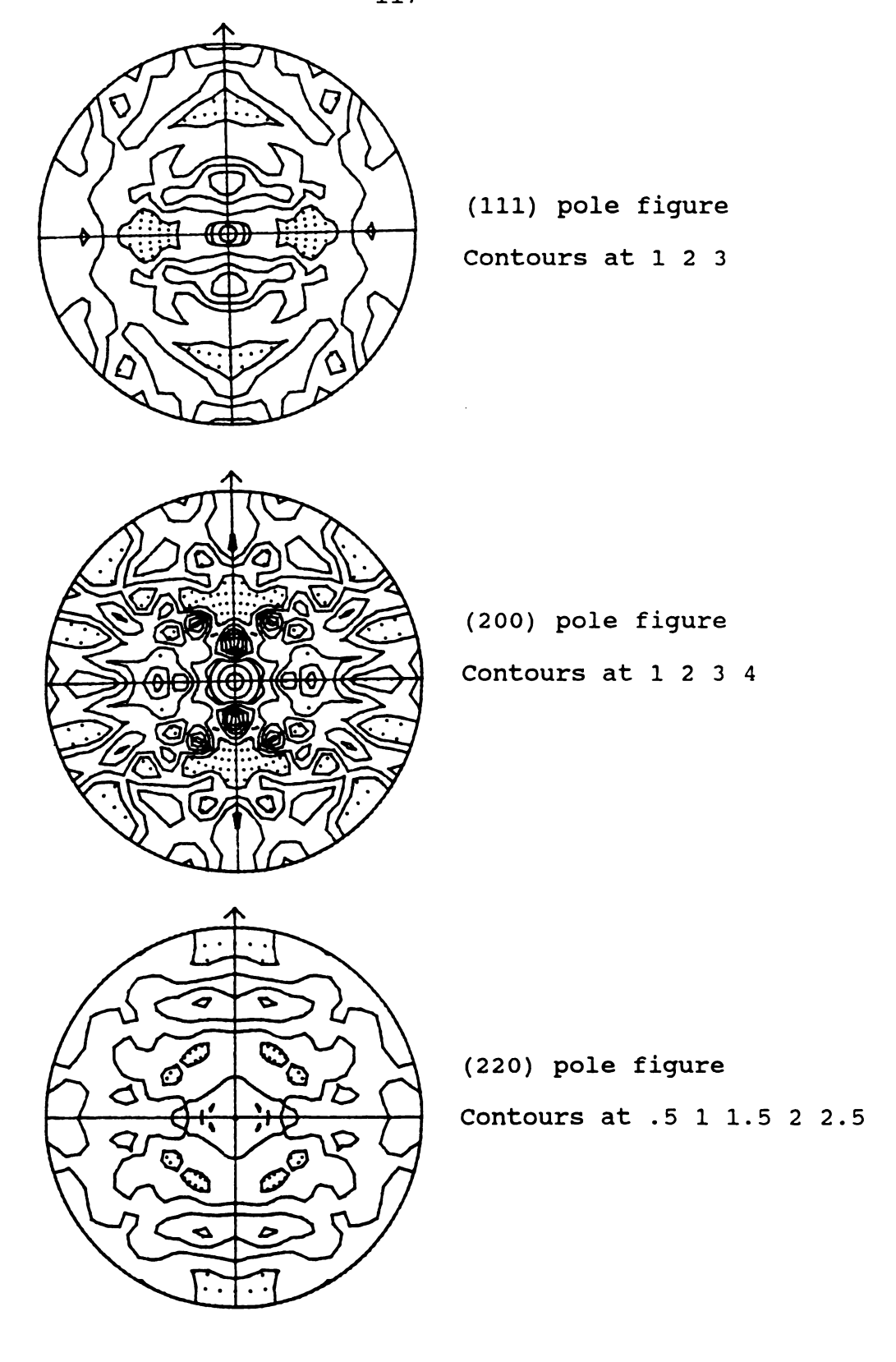
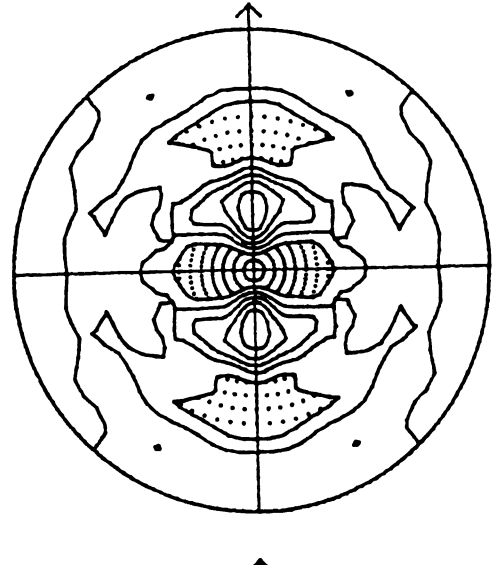
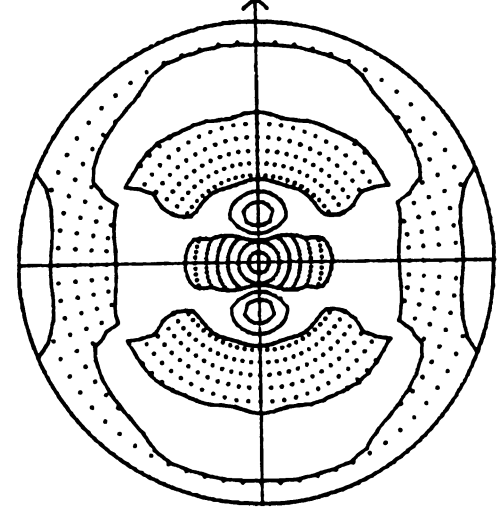


Fig.A.1 (111),(200),(220) pole figures of specimen deformed at 1/sec and  $T=425\,^{\circ}\text{C}$ . (a)-(f)

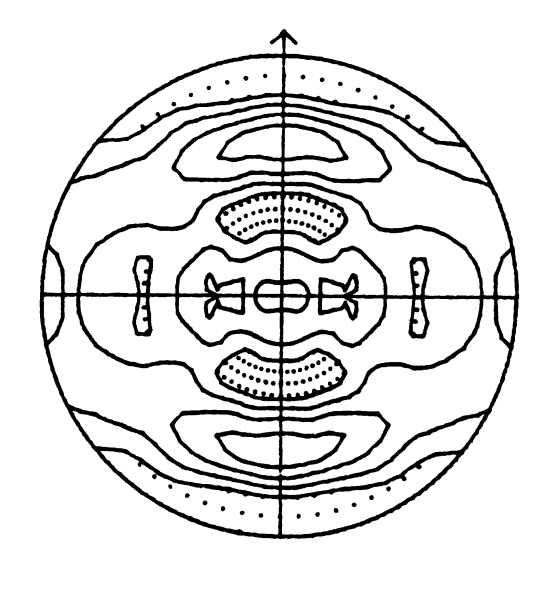
(a)  $\epsilon=0$ 



(111) pole figure
Contours at .5 1 1.5 2 2.5

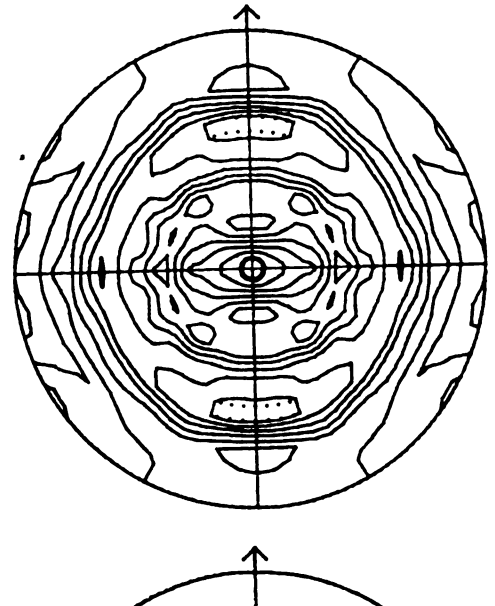


(200) pole figure
Contours at .5 1 1.5 2 2.5

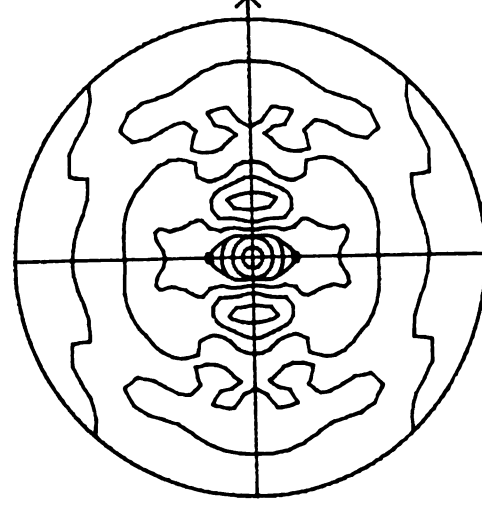


(220) pole figure
Contours at .5 1 1.5 2

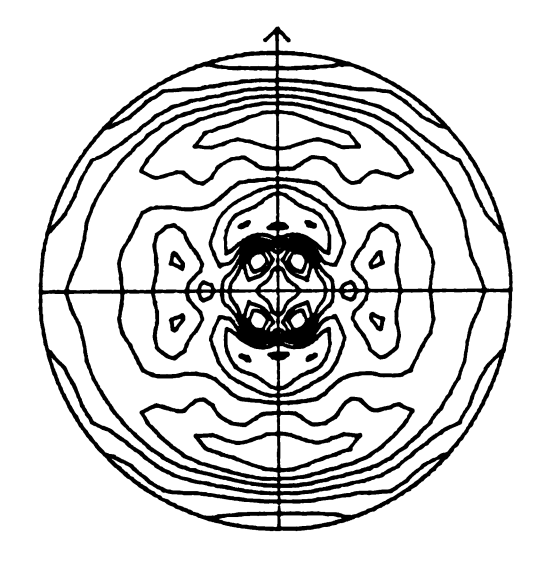
(b)  $\epsilon=1.1$ 



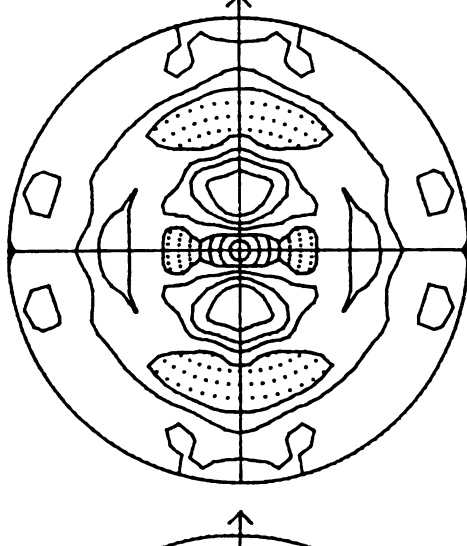
(111) pole figure
Contours at .5 1 1.5 2



(200) pole figure
Contours at .5 1 1.5 2

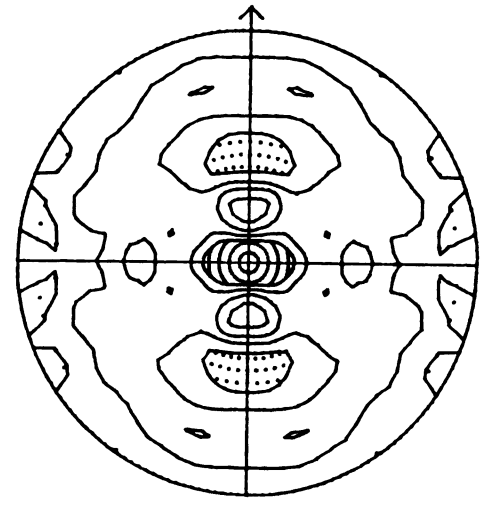


(220) pole figure
Contours at .5 1 1.5 2

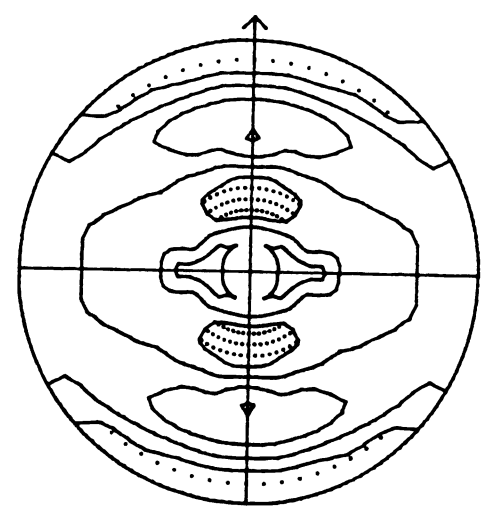


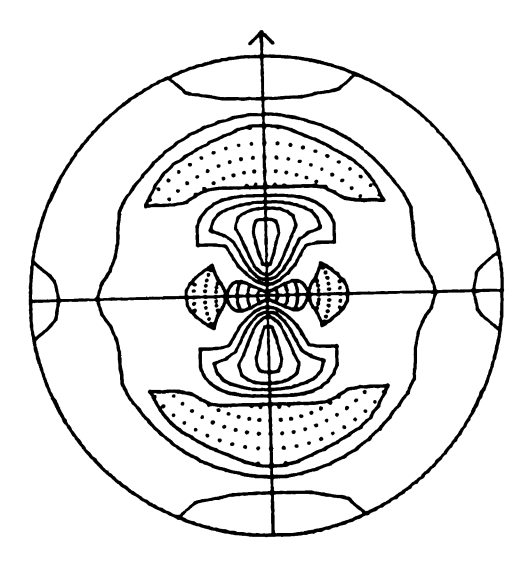
(111) pole figure

Conyours at .25 .5 .75 1
1.25 1.5

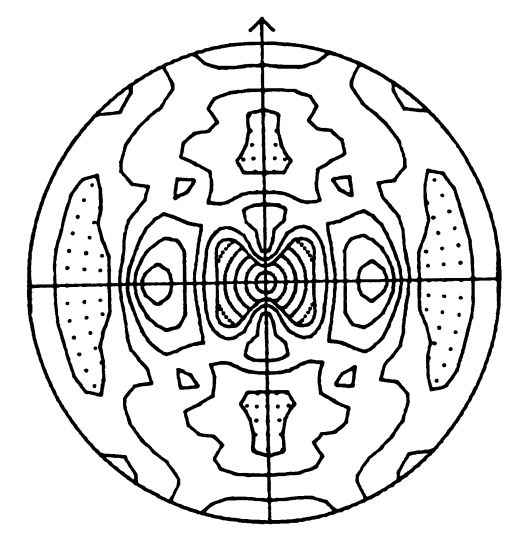


(200) pole figure
Contours at .5 1 1.5 2

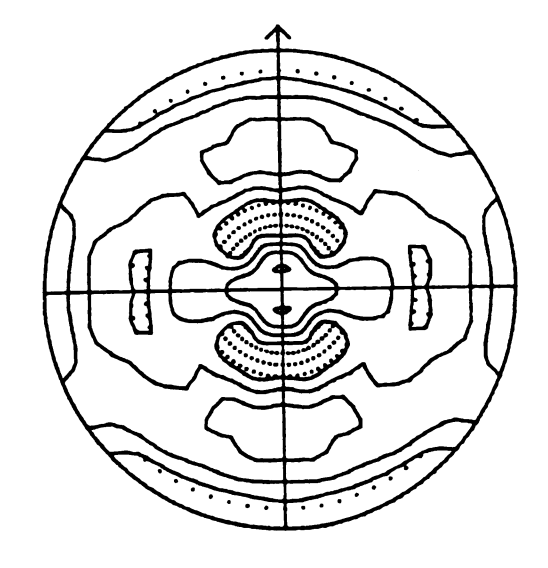




(111) pole figure
Contours at .5 1 1.5 2 2.5

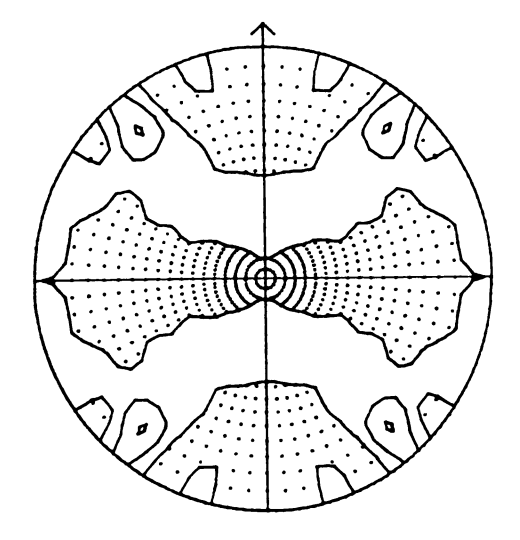


(200) pole figure
Contours at 1 2 3

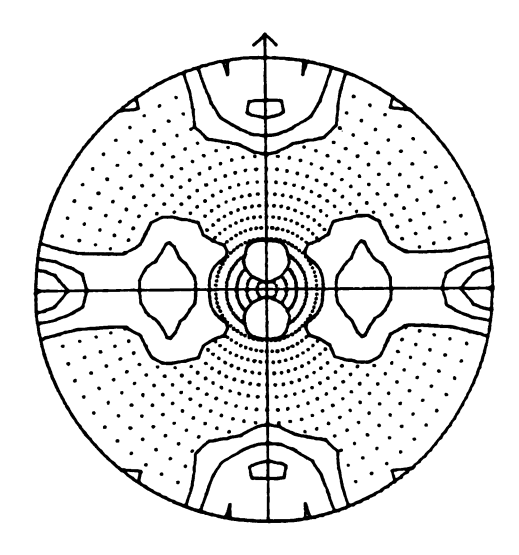


(220) pole figure
Contours at .5 1 1.5 2

(e)  $\epsilon = 2.6$ 



(111) pole figure
Contours at .5 1 1.5 2



(200) pole figure

Contours at .5 1 1.5 2 2.5



(220) pole figure
Contours at .5 1 1.5 2

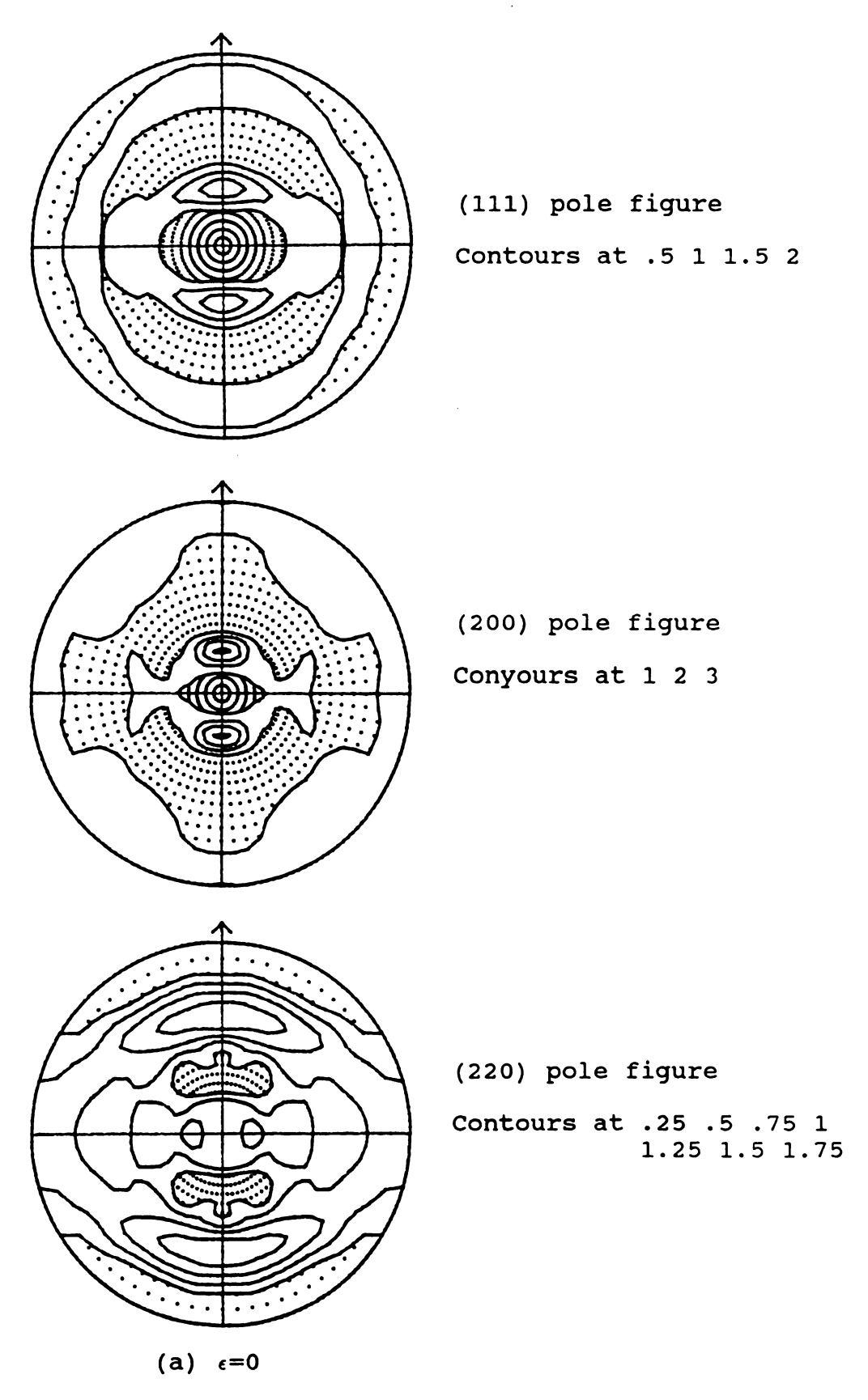
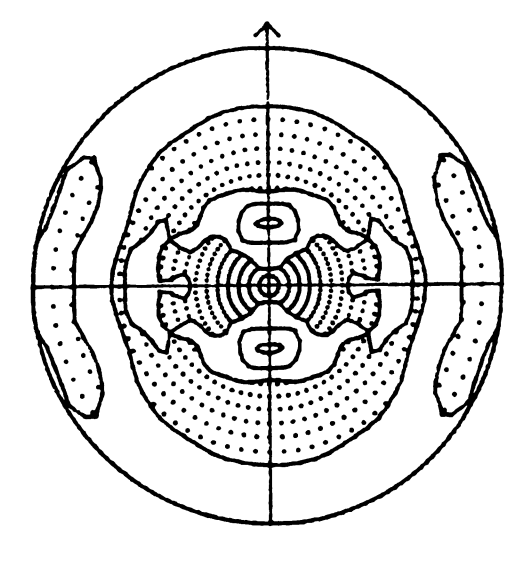
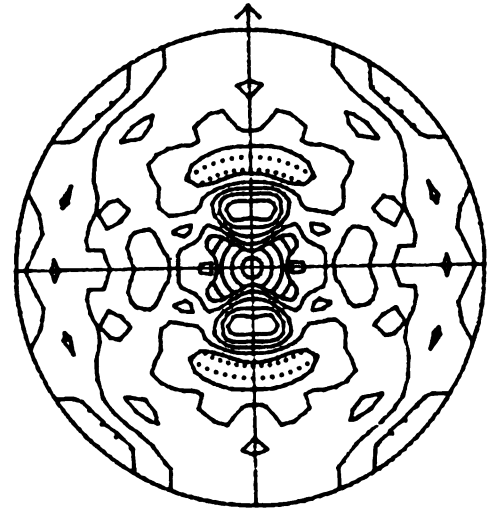


Fig.A.2 (111),(200),(220) Pole figures of specimen deformed at  $\dot{\epsilon}$ =77/sec and T=475°C. (a)-(e)



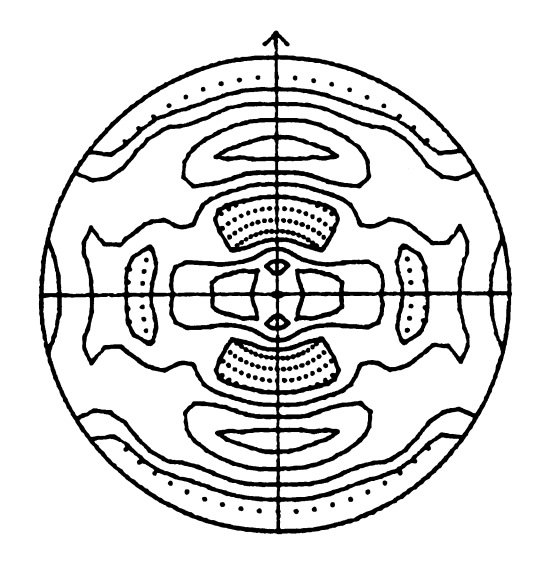
(111) pole figure

Contours at .25 .5 .75 1 1.25 1.5 1.75



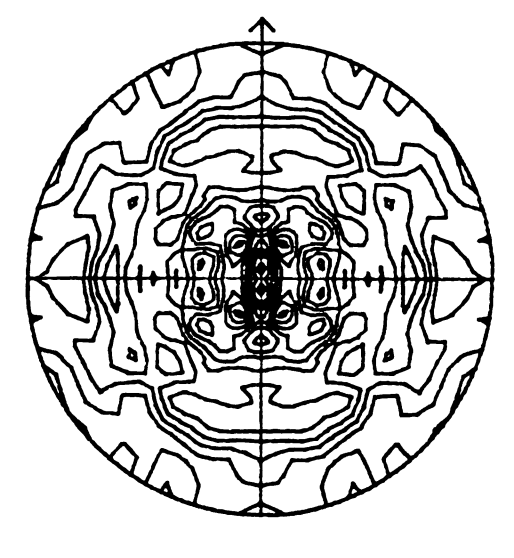
(200) pole figure

Contours at .25 .5 .75 1 1.25 1.5



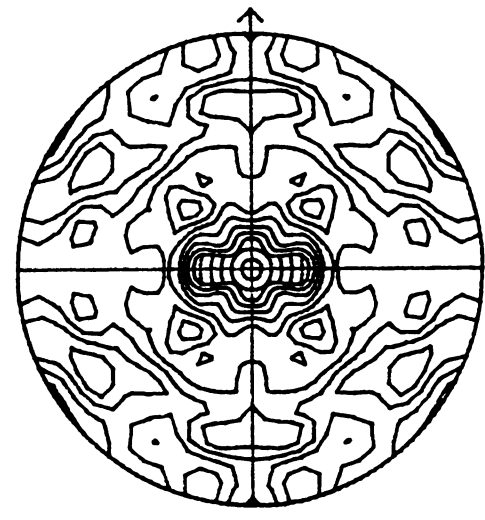
(220) pole figure

Conyours at .25 .5 .75 1 1.25 1.5



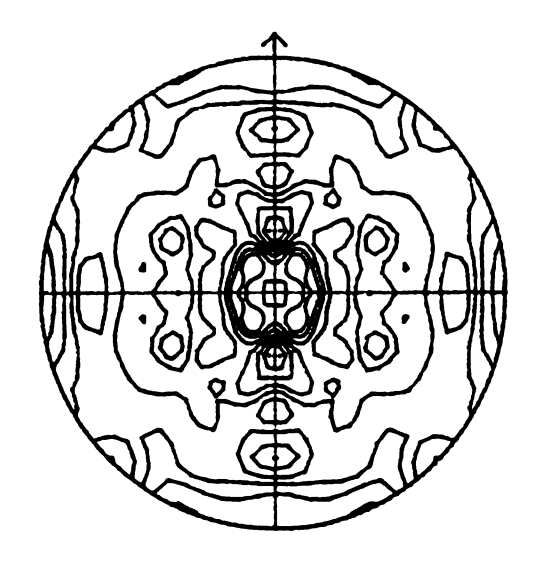
(111) pole figure

Contours at .25 .5 .75 1 1.25 1.5 1.75 2



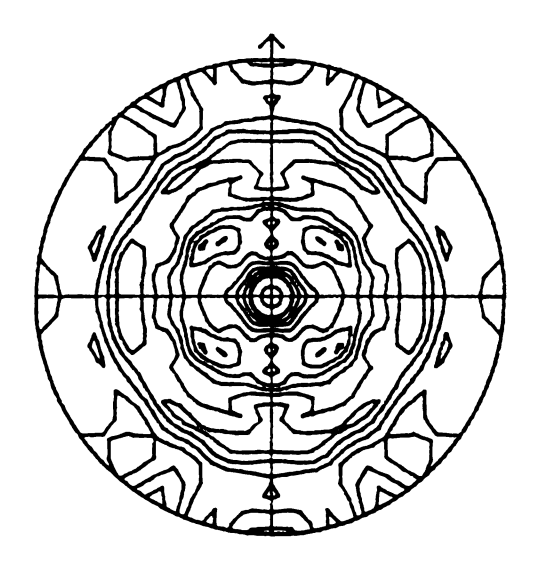
# (200) pole figure

Contours at .25 .5 .75 1 1.25 1.5 1.75

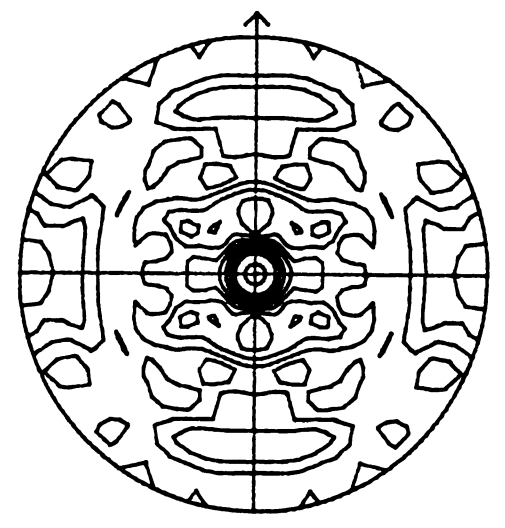


# (220) pole figure

Contours at .25 .5 .75 1 1.25 1.5 1.75



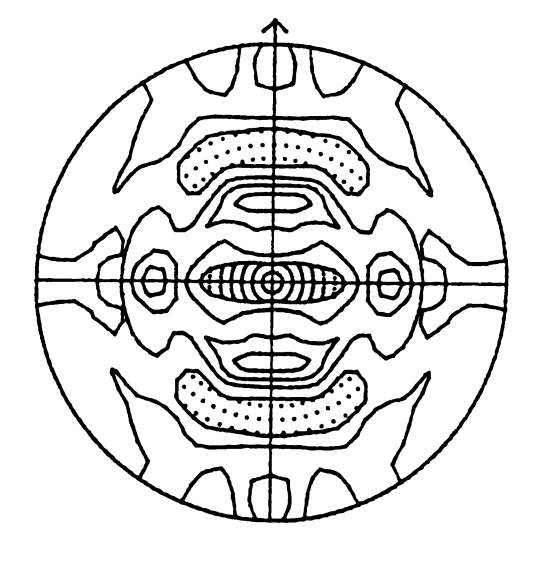
(111) pole figure
Contours at 1 2 3



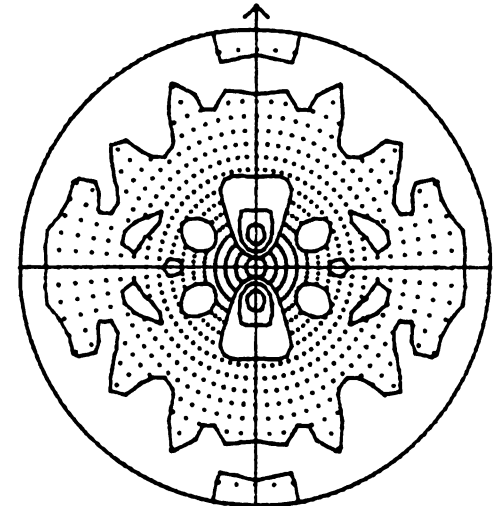
(200) pole figure
Contours at .5 1 1.5 2 2.5



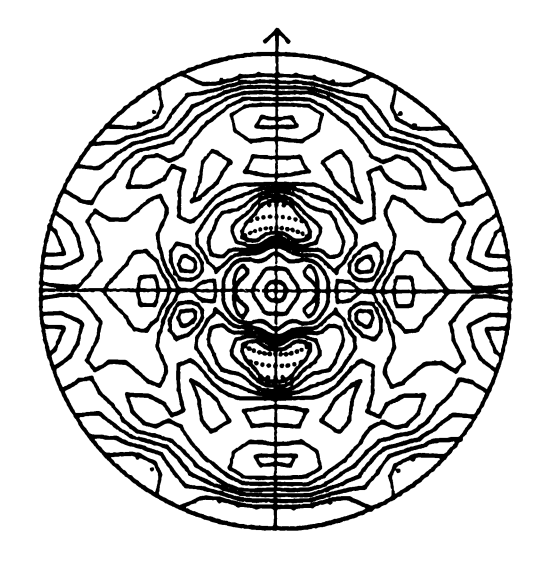
(220) pole figure
Contours at .5 1 1.5 2



(111) pole figure
Contours at 1 2 3



(200) pole figure
Contours at 1 2 3 4



(220) pole figure
Contours at .5 1 1.5 2

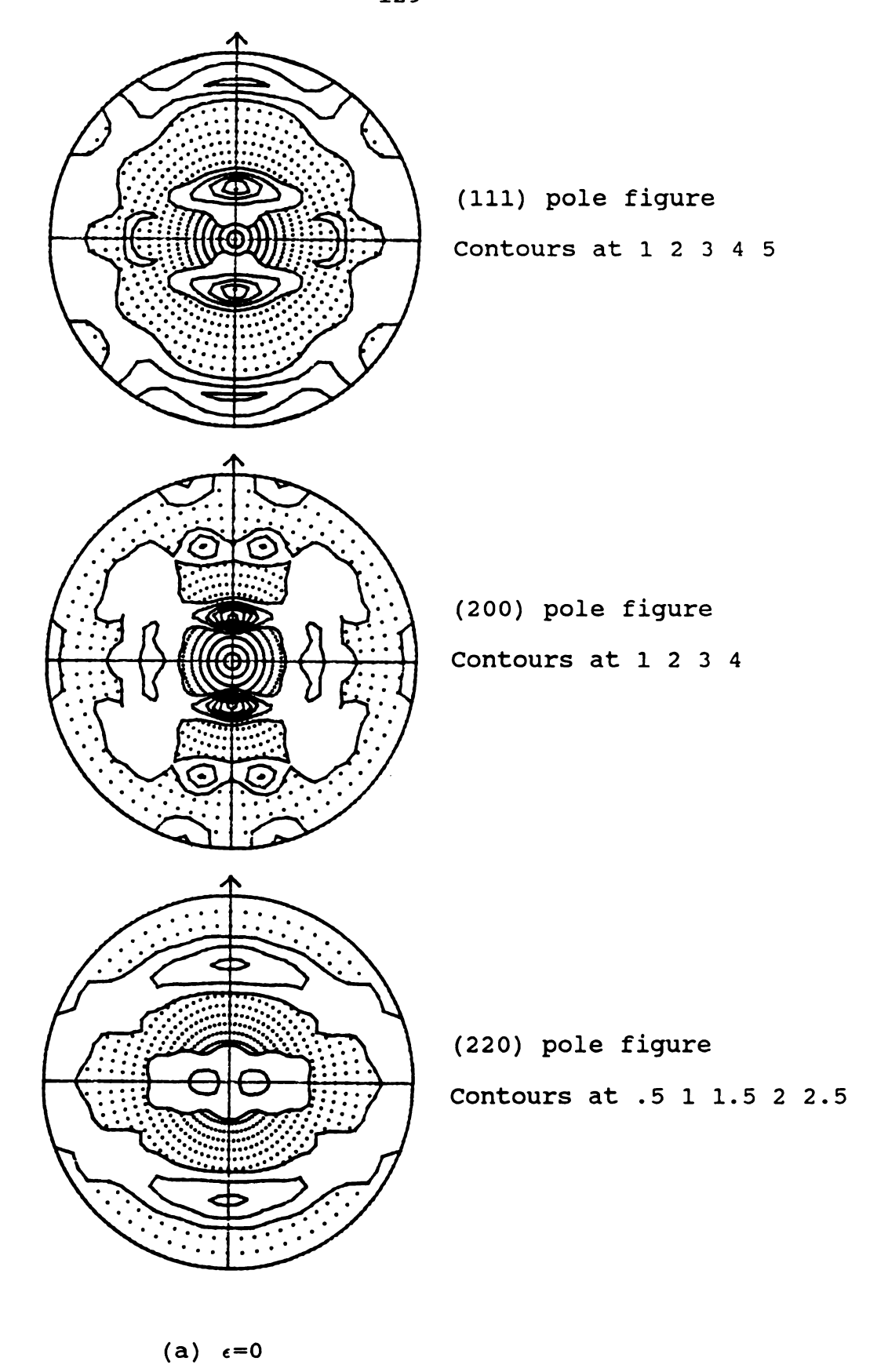
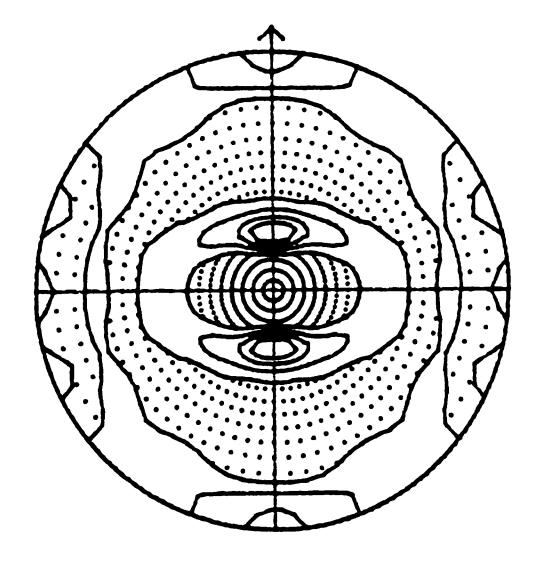
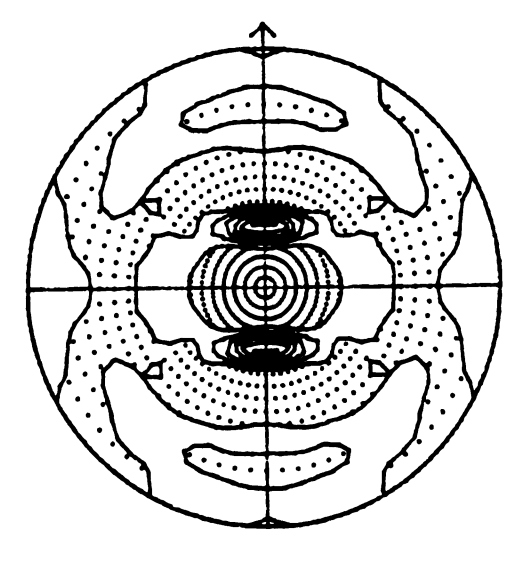


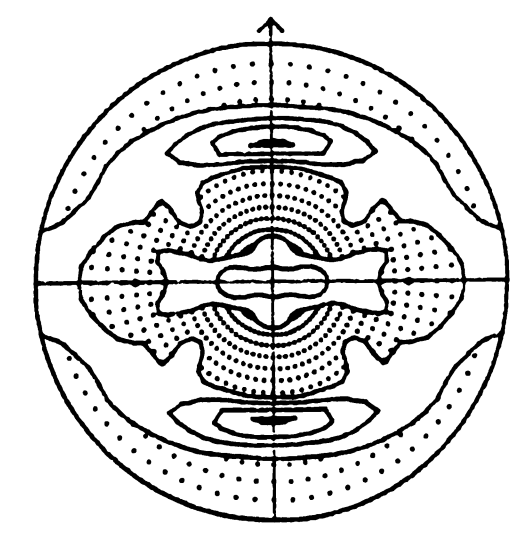
Fig.A.3 (111),(200),(220) pole figures of specimen deformed at  $\dot{\epsilon}$ =330/sec and T=475°C. (a)-(d)



(111) pole figure
Contours at 1 2 3 4 5 6 7

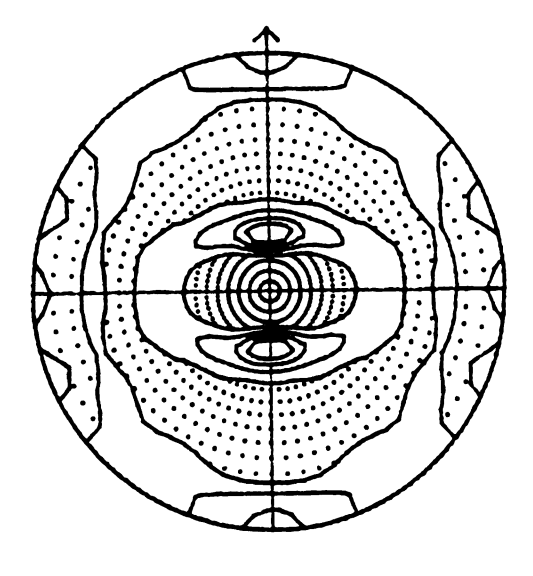


(200) pole figure
Contours at 1 2 3 4

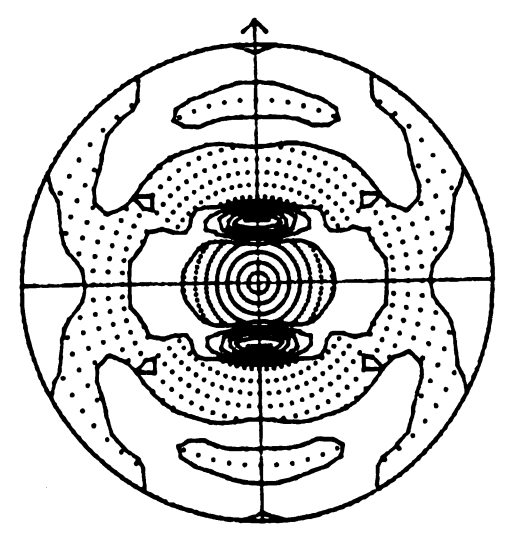


(220) pole figure
Contours at 1 2 3

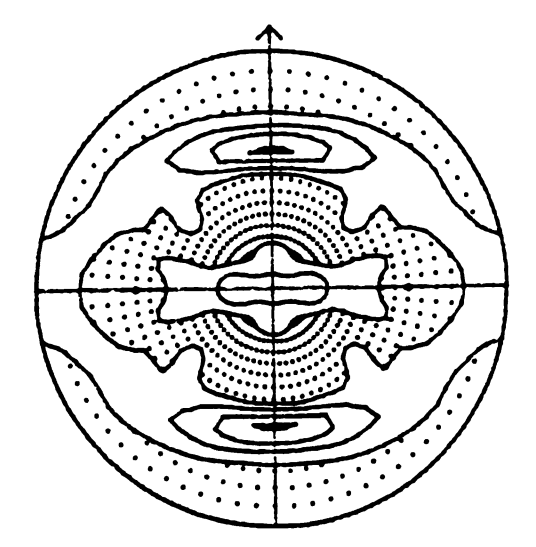
(b)  $\epsilon = 0.45$ 



(111) pole figure
Contours at 1 2 3 4 5 6 7

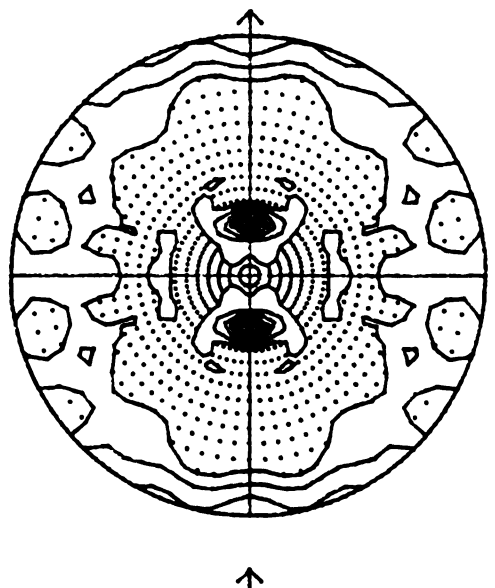


(200) pole figure
Contours at 1 2 3 4

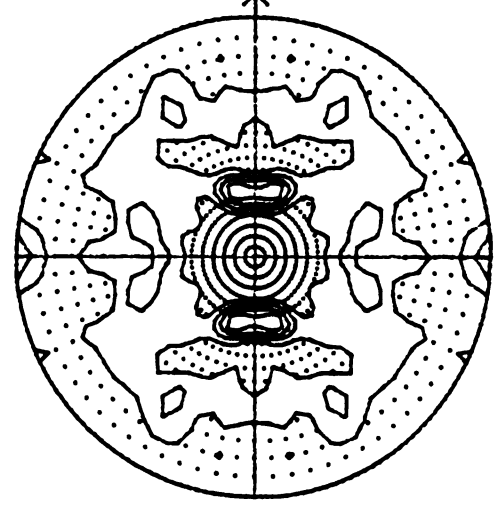


(220) pole figure
Contours at 1 2 3

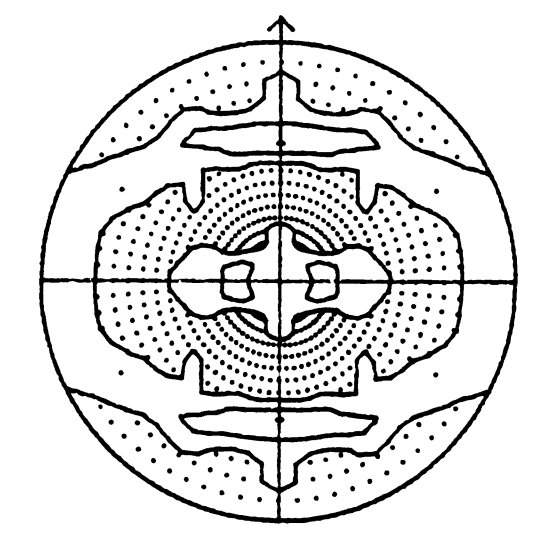
(b)  $\epsilon = 0.45$ 



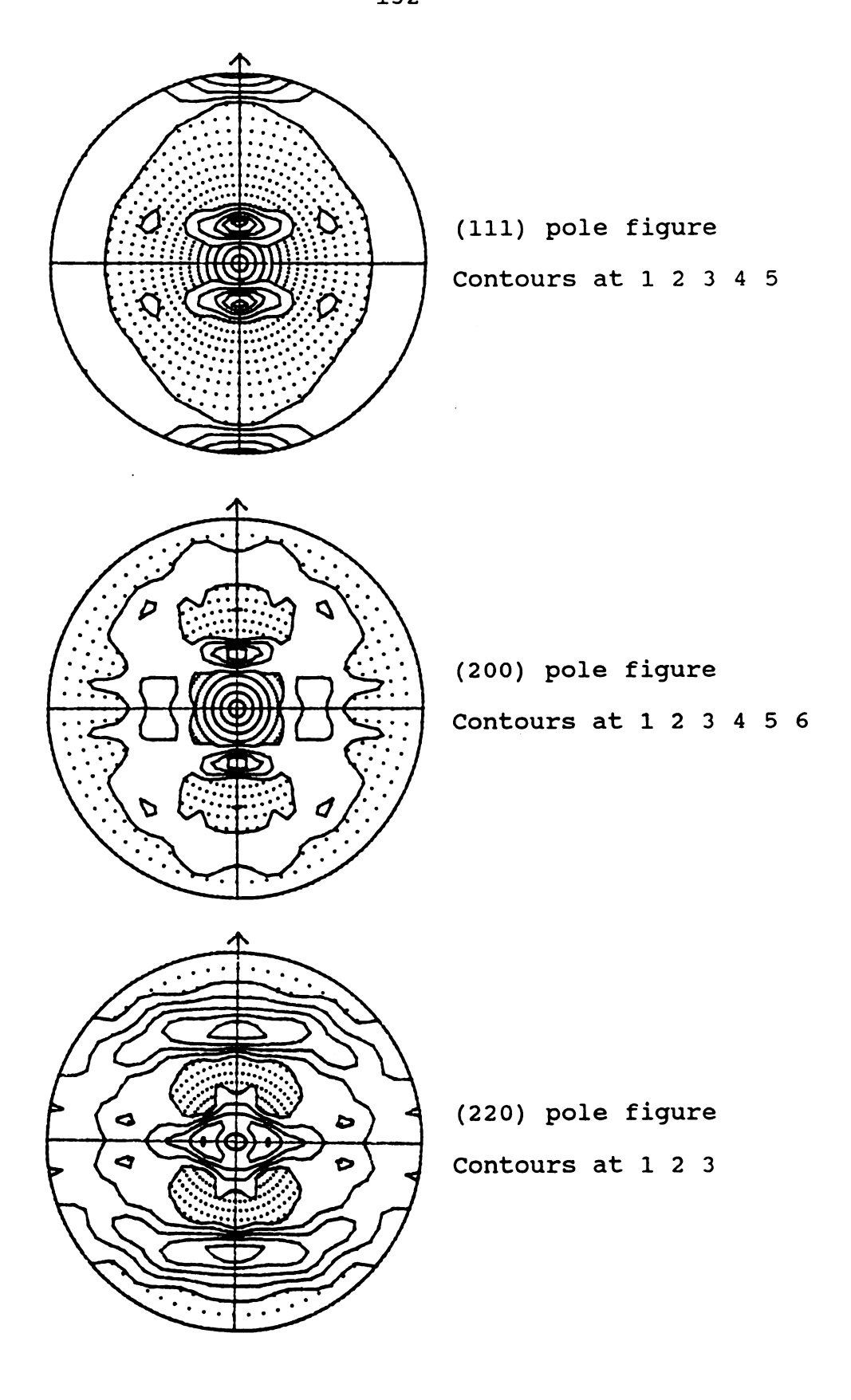
(111) pole figure
Contours at 1 2 3 4



(200) pole figure
Contours at 1 2 3 4 5 6

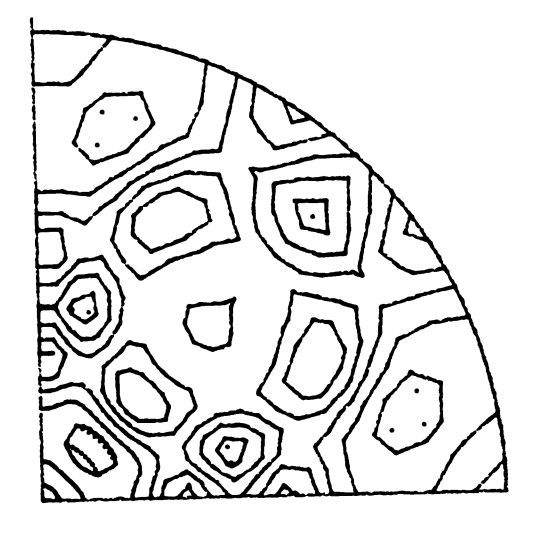


(220) pole figure
Contours at 1 2 3 4



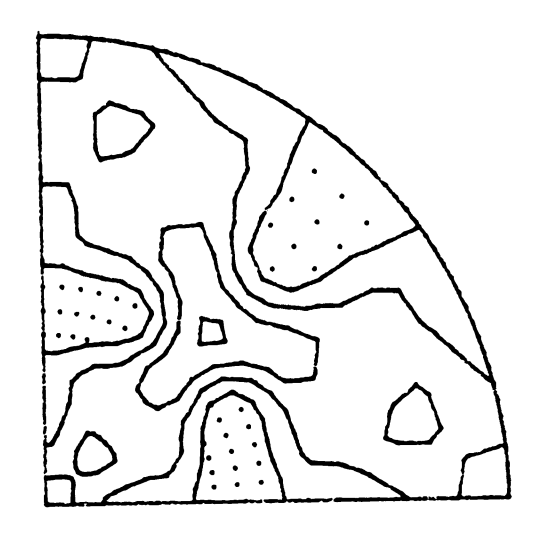
## APPENDIX B INVERSE POLE FIGURES OF IN90211

- Fig. B.1 Inverse pole figures of specimen deformed at  $\dot{\epsilon}=1/\text{sec}$  and T=425°C. (a)-(f)
- Fig. B.2 Inverse pole figures of specimen deformed at  $\dot{\epsilon}$ =77/sec and T=475°C. (a)-(e)
- Fig. B.3 Inverse pole figures of specimen deformed at  $\dot{\epsilon}$ =330/sec and T=475°C. (a)-(d)



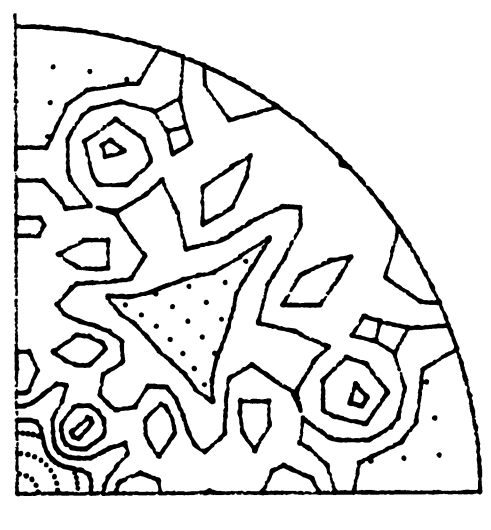
Inverse PF of RD

Contours at .5 .75 1 1.25
1.5



Inverse PF of TD

Contours at .5 1 1.5 2

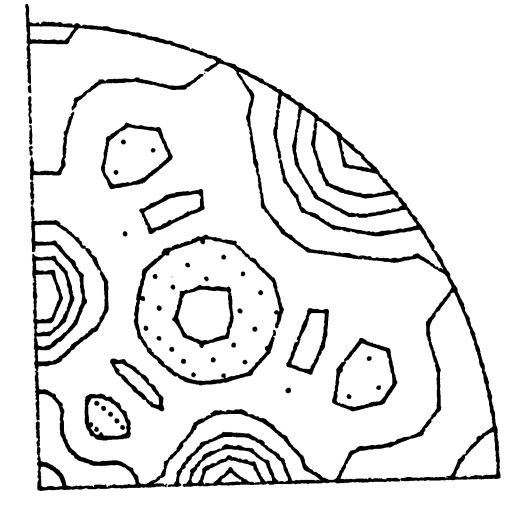


Inverse PF of ND

Contours at .5 1 1.5 2

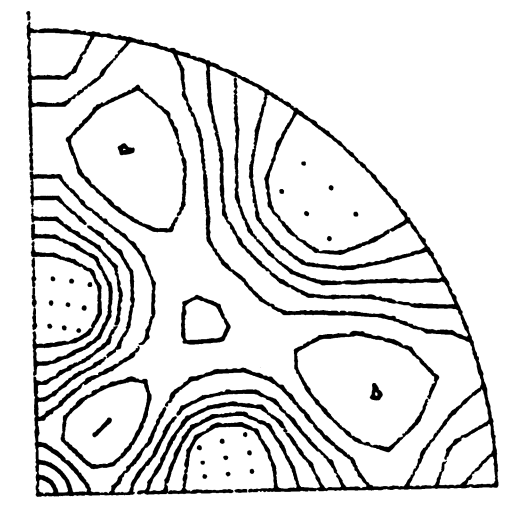
(a)  $\epsilon=0$ 

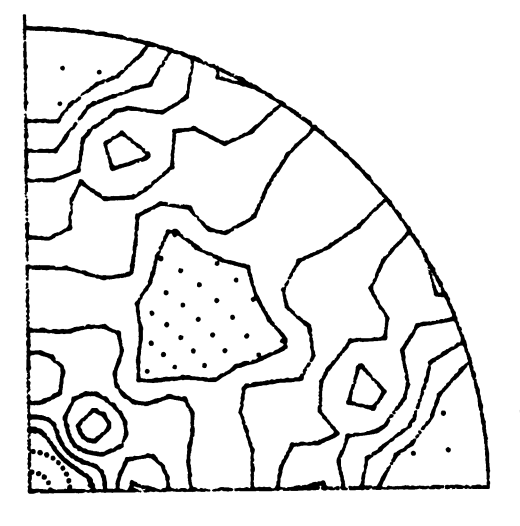
Fig. B.1 Inverse pole figures of specimen deformed at  $\dot{\epsilon}$ =1/sec and T=425°C. (a)-(f)



Inverse PF of RD

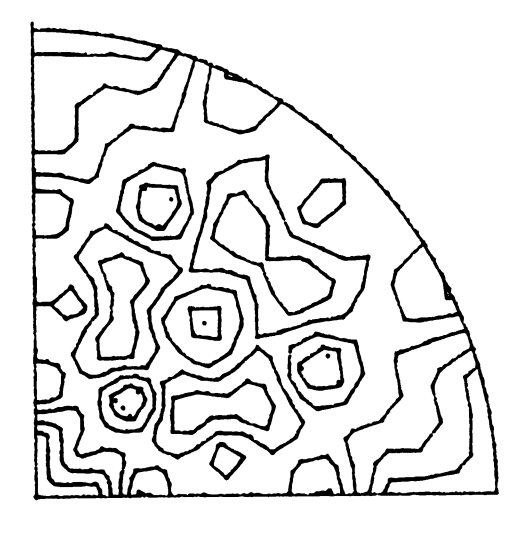
Contours at .8 1 1.2 1.4 1.6
1.8



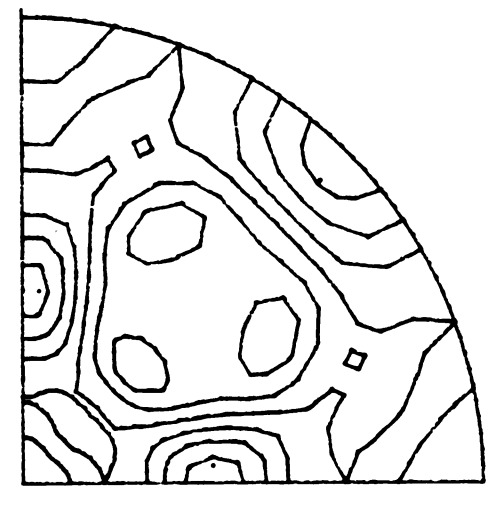


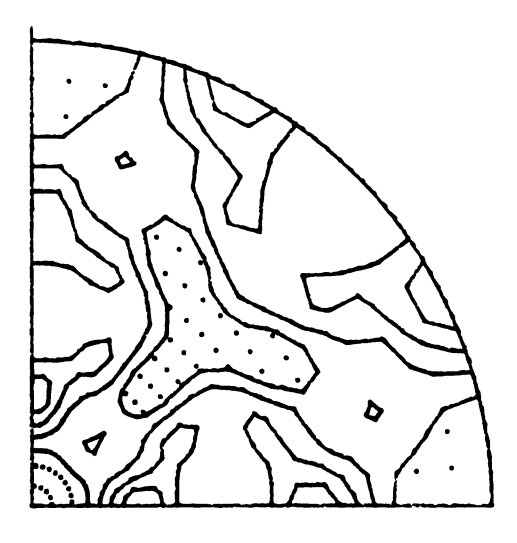
Inverse PF of ND

Contours at .5 1 1.5 2



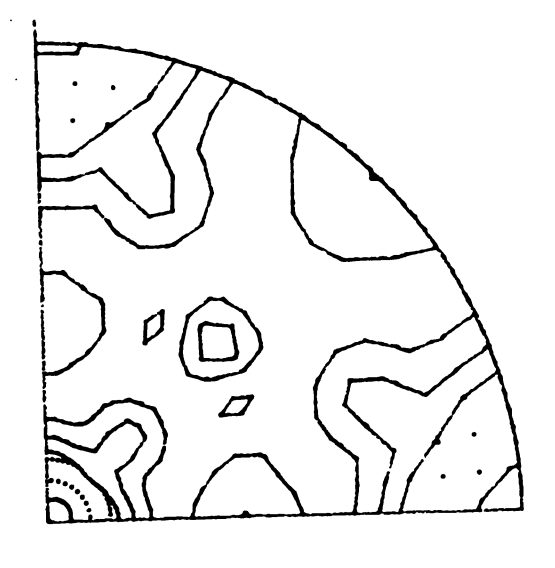
Inverse PF of RD
Contours at .8 .9 1 1.1 1.2





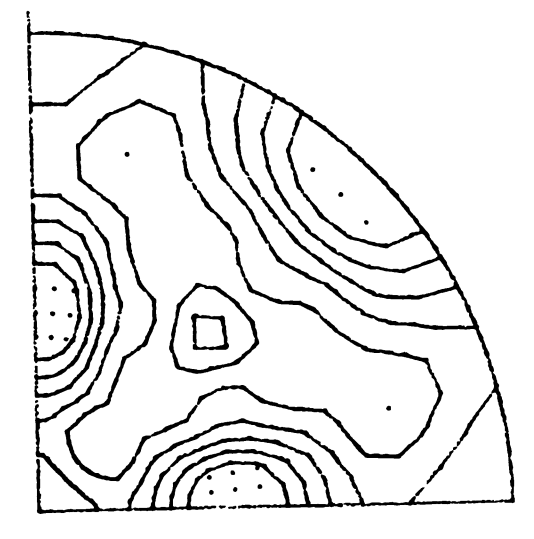
Inverse PF of ND

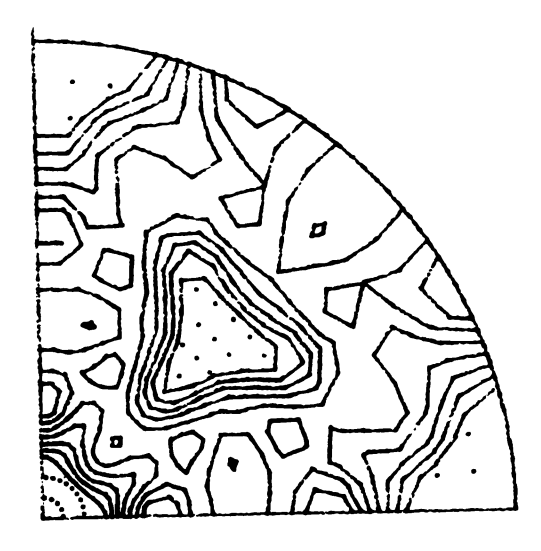
Contours at .5 1 1.5 2

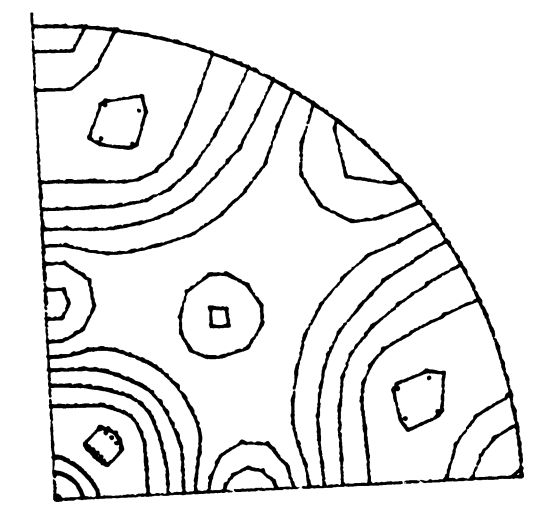


Inverse PF of RD

Contours at .6 .8 1 1.2 1.4

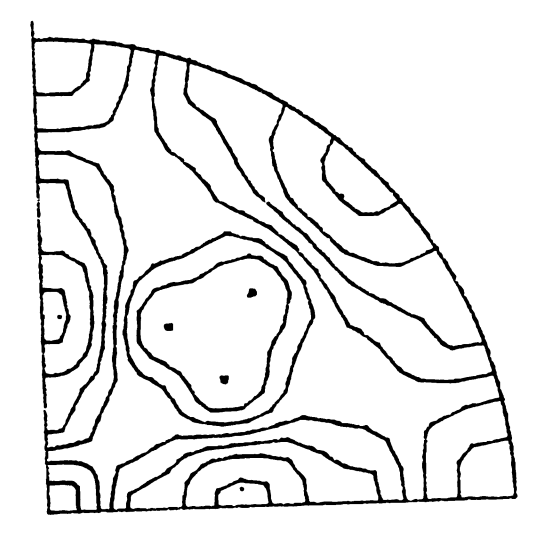






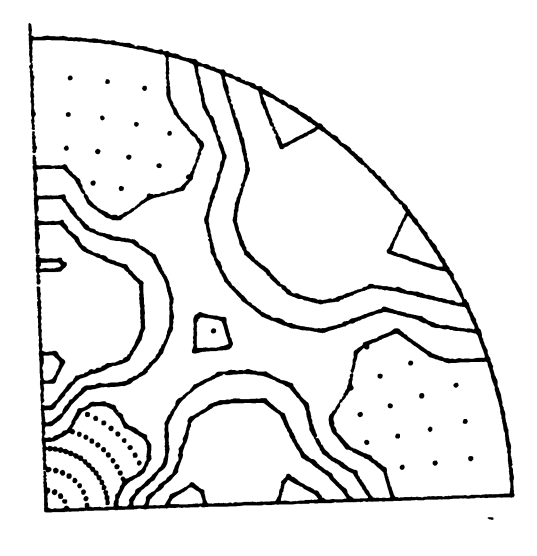
Inverse PF of RD

Contours at .25 .5 .75 1 1.25 1.5 1.75



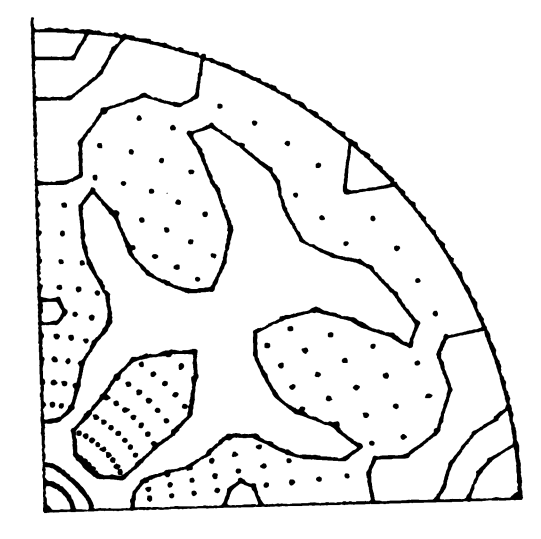
Inverse PF of TD

Contours at .25 .5 .75 1 1.25 1.5 1.75



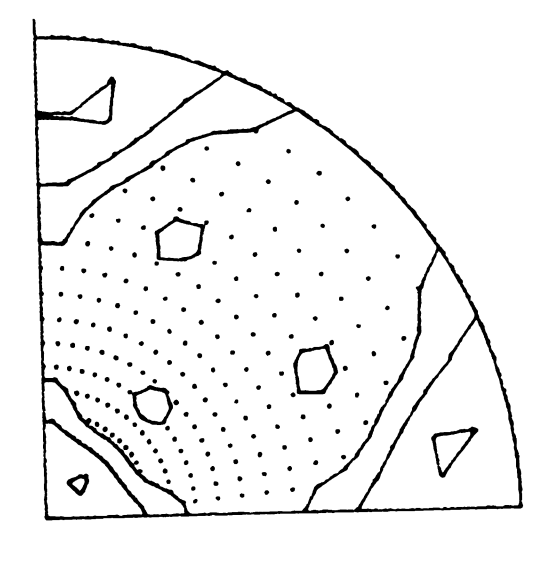
Inverse PF of ND

Contours at .5 1 1.5 2

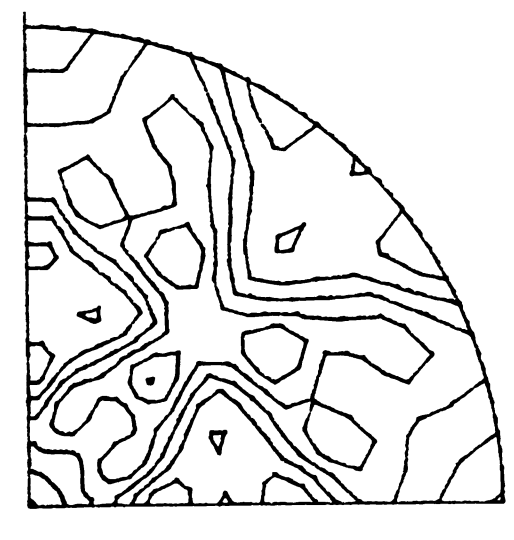


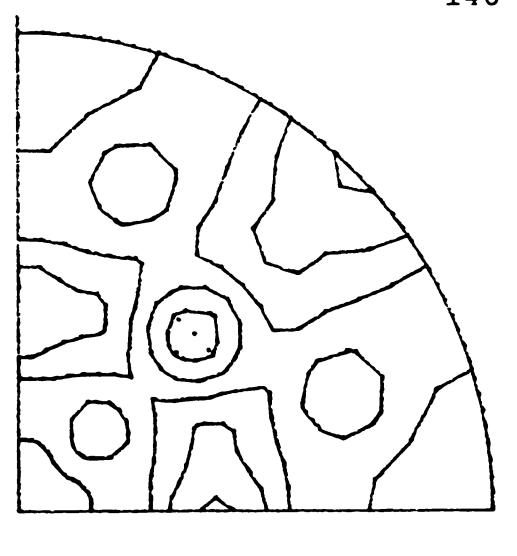
Inverse PF of RD

Contours at 1 2 3 4



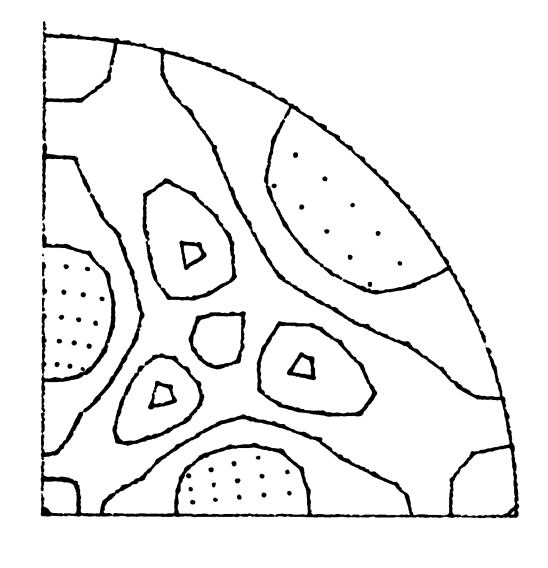
Inverse PF of TD
Contours at 1 2 3





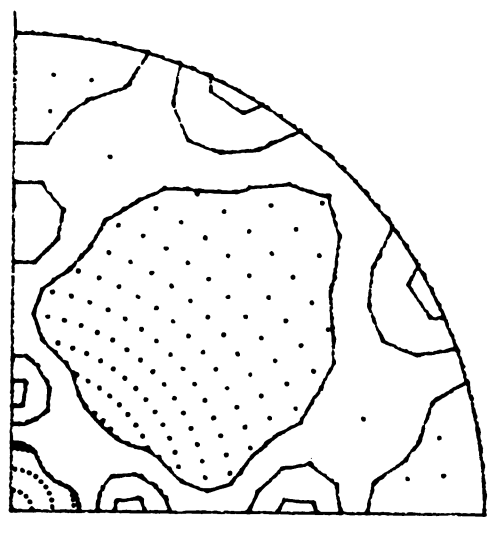
Inverse PF of RD

Contours at .6 .8 1 1.2 1.4



Inverse PF of TD

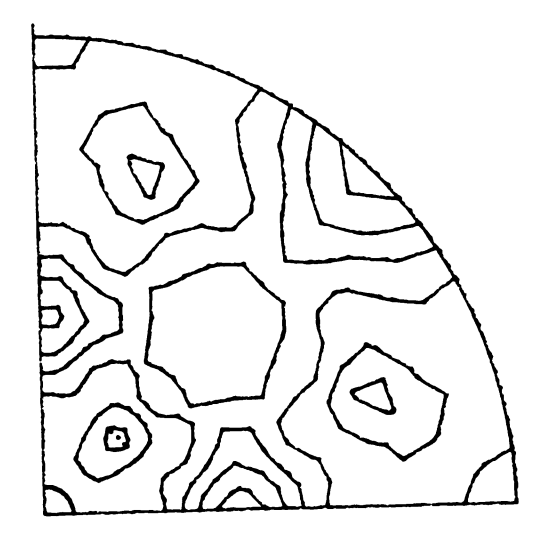
Contours at .5 1 1.5 2



Inverse PF of ND
Contours at 1 2 3

(a)  $\epsilon=0$ 

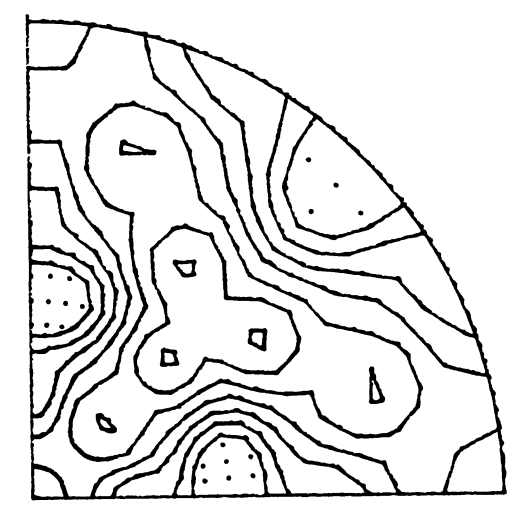
Figure B.2 Inverse pole figures of specimen deformed at  $\dot{\epsilon}$ =77/sec and T=475°C. (a)-(e)

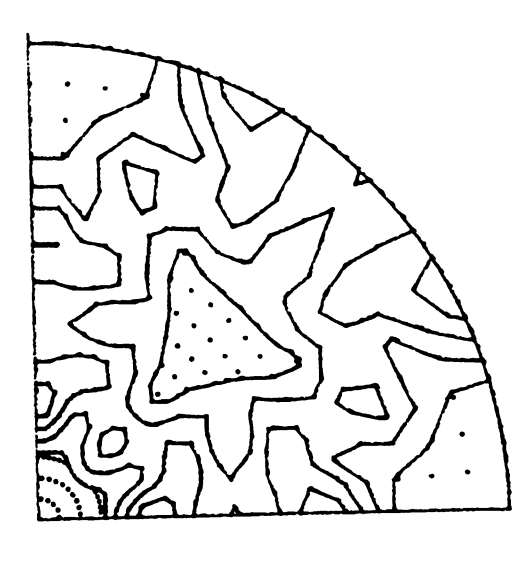


Inverse PF of RD

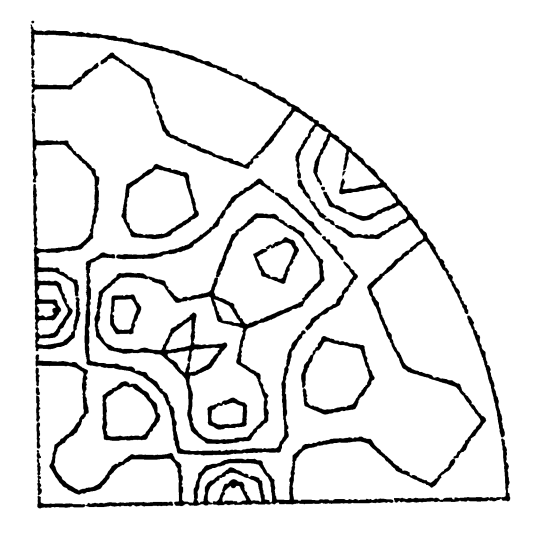
Coutours at .6 .8 1 1.2 1.4

1.6



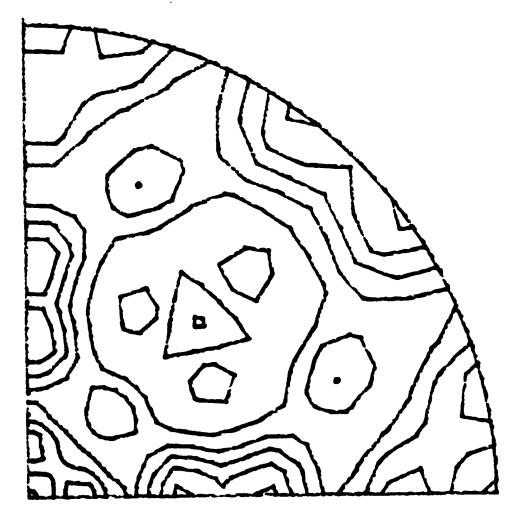


Inverse PF of ND
Contours at .5 1 1.5 2



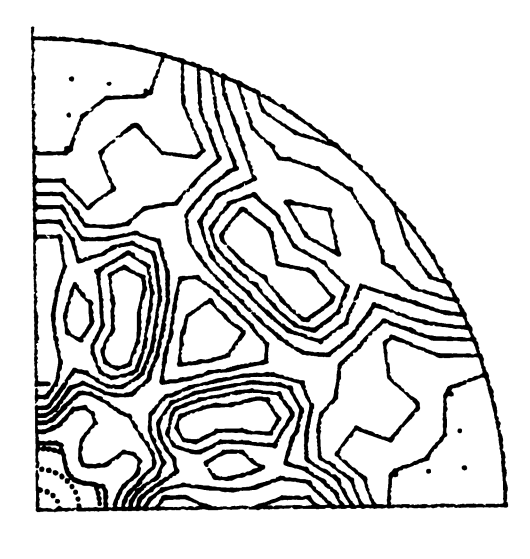
Inverse PF of RD

Contours at .6 .8 1 1.2 1.4

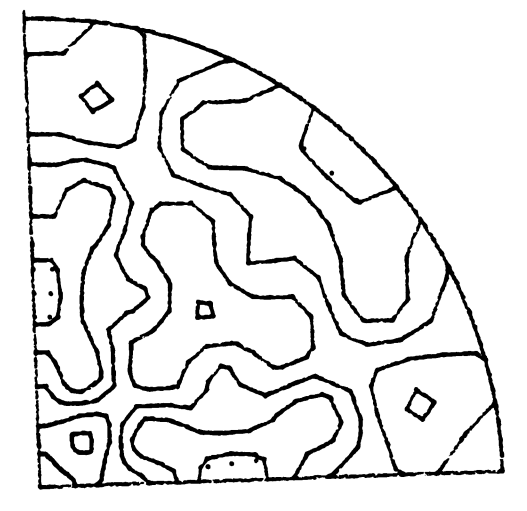


Inverse PF of TD

Contours at .5 .75 1 1.25
1.5

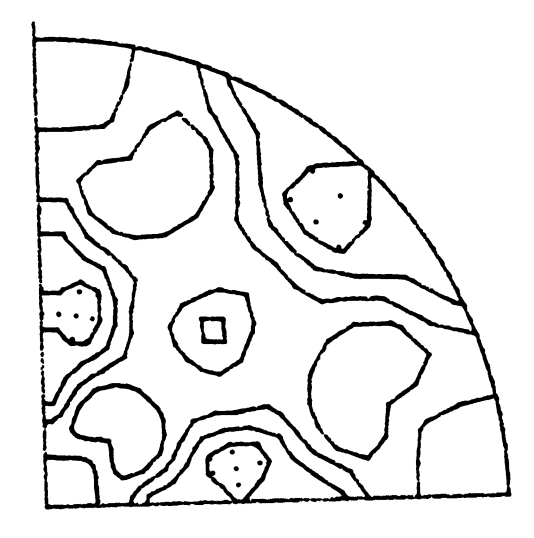


Inverse PF of ND
Contours at .5 1 1.5 2



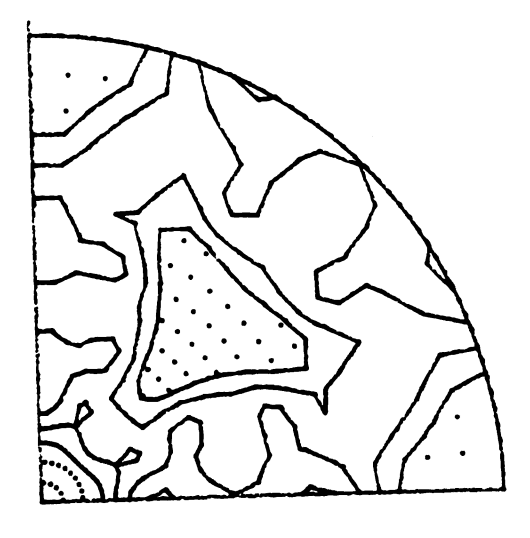
Inverse PF of RD

Contours at .4 .6 .8 1 1.2 1.4



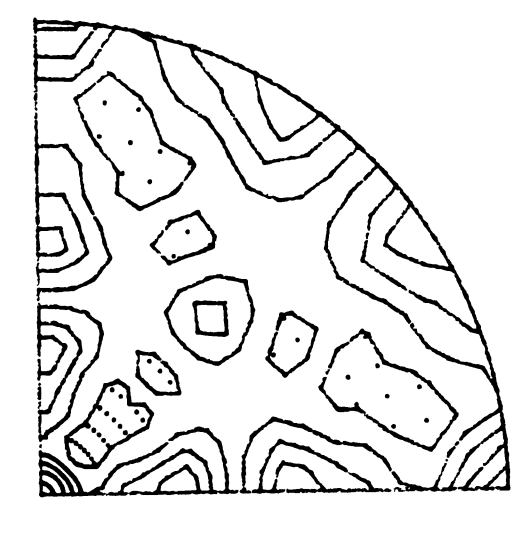
Inverse PF of TD

Contours at .4 .6 .8 1 1.2 1.4 1.6



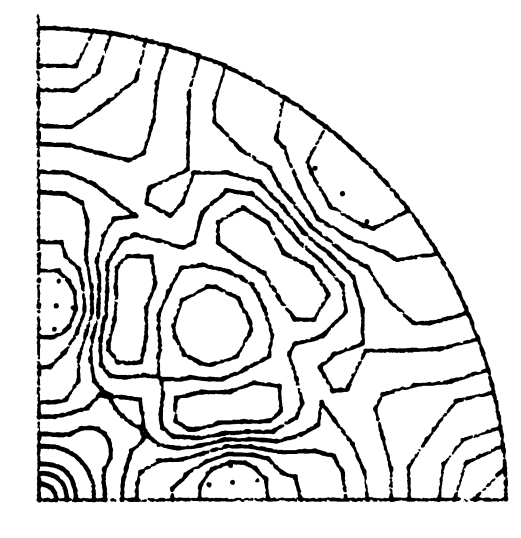
Inverse PF of ND

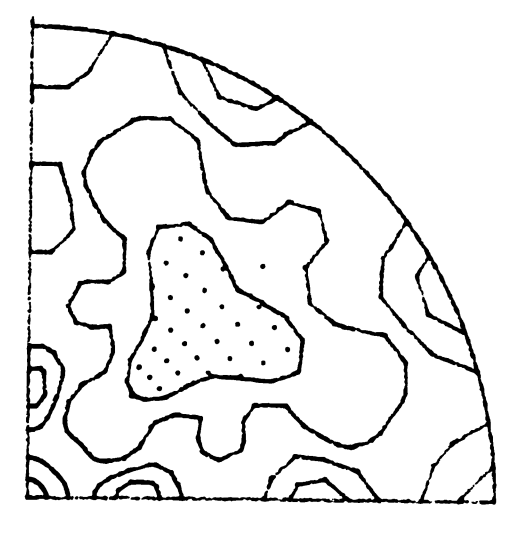
Contours at .25 .5 .75 1 1.25 1.5 1.75



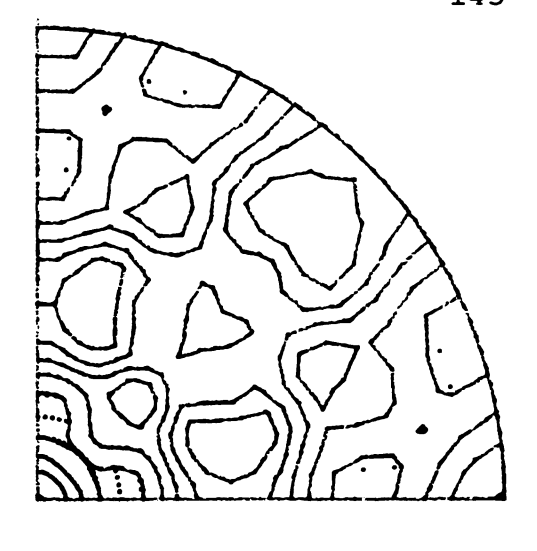
Inverse PF of RD

Contours at .75 1 1.25 1.5
1.75 2



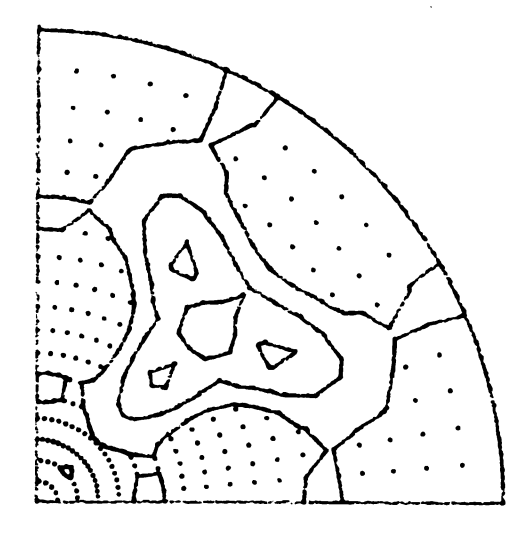


Inverse PF of ND
Contours at .5 1 1.5 2

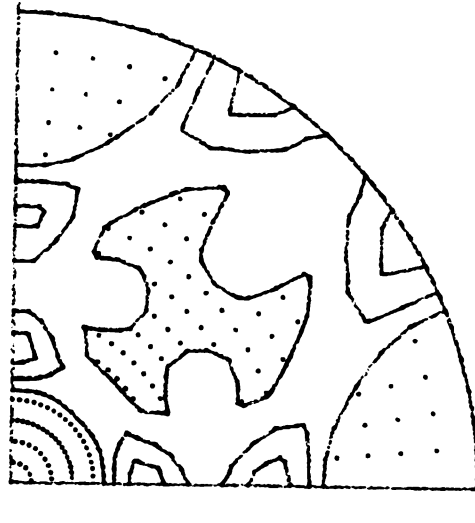


Inverse PF of RD

Contours at .5 .75 1 1.25
1.5



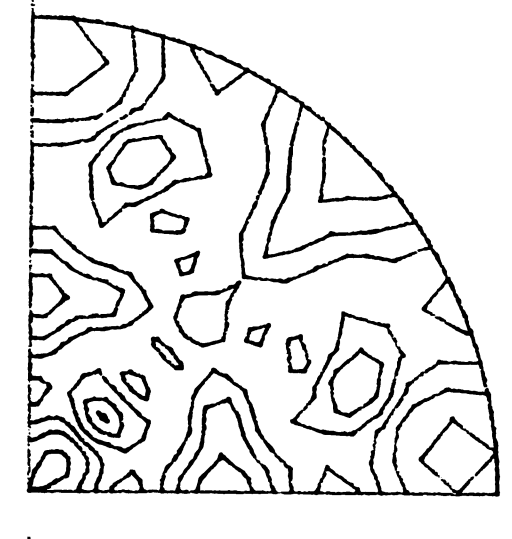
Inverse PF of TD
Contours at 1 2 3



Inverse PF of ND Contours at 1 2 3

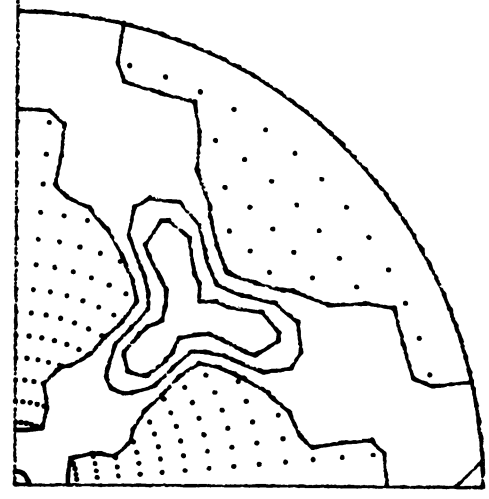
(a)  $\epsilon=0$ 

Fig.B.3 Inverse pole figures of specimen deformed at  $\dot{\epsilon}$ =330/sec and T=475°C. (a)-(d)

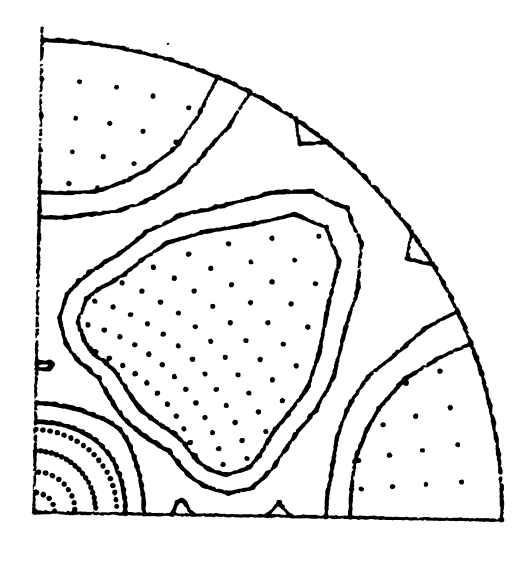


Inverse PF of RD

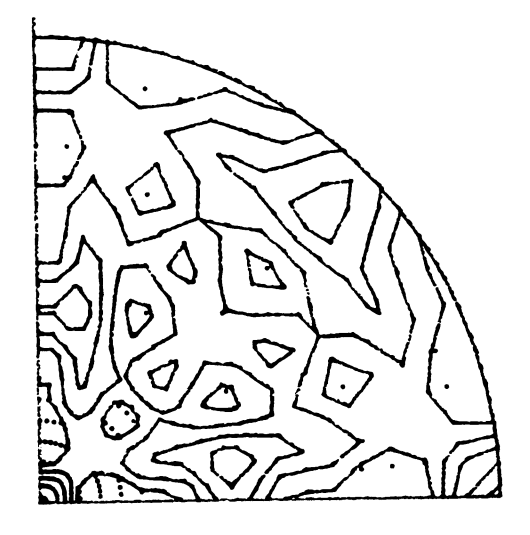
Contours at .4 .6 .8 1 1.2
1.4



Inverse PF of TD
Contours at 1 2 3

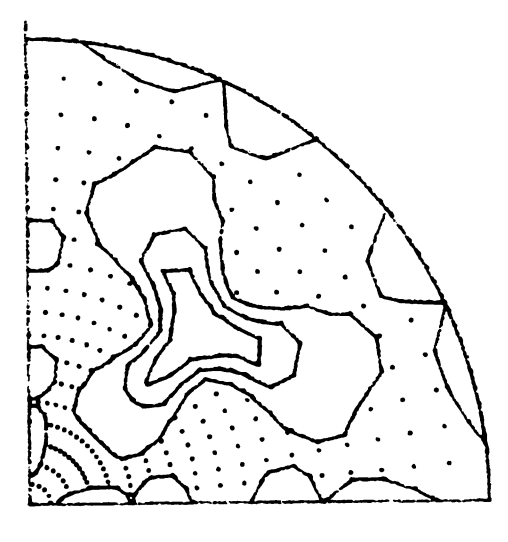


Inverse PF of ND Contours at 1 2 3

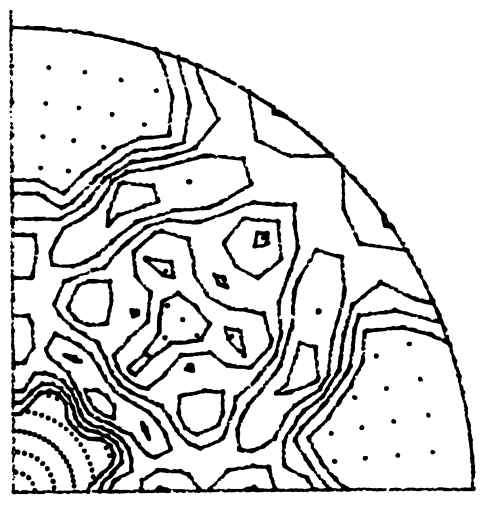


Inverse PF of RD

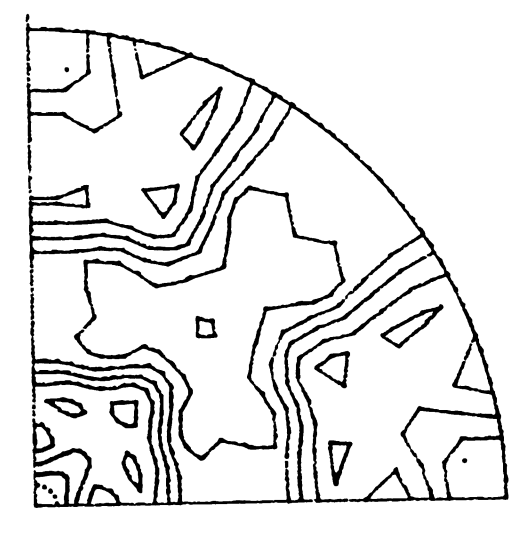
Contours at .5 1 1.5 2 2.5

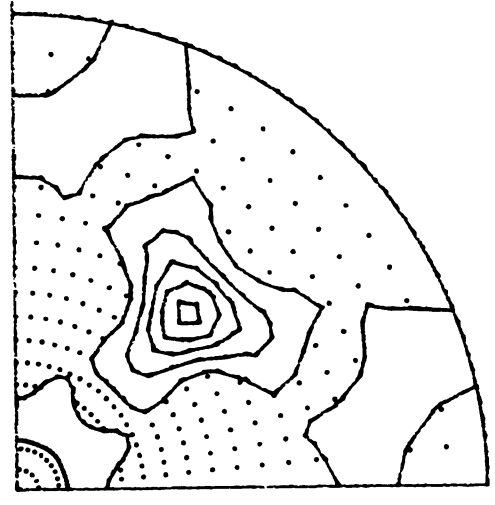


Inverse PF of TD
Contours at 1 2 3



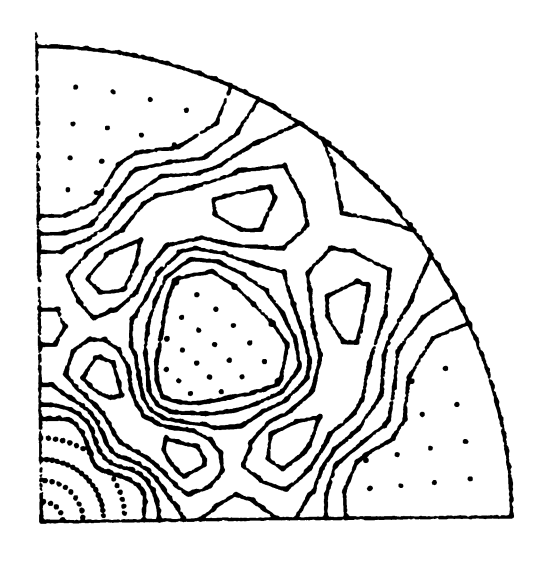
Inverse PF of ND
Contours at .5 1 1.5 2 2.5





Inverse PF of TD

Contours at 1 2 3 4 5



Inverse PF of ND
Contours at .5 1 1.5 2 2.5



## LIST OF REFERENCES

- [1] Metallurgical Reviews 10 (1965) 272
- [2] E.A.Calnan & C.J.B.Clews: Phil. Mag., 41(1950), 1085
- [3] J.F.W.Bishop: J.Mechanics Physics Solids 3(1954), 130
- [4] J.F.W.Bishop & R.Hill: Phil. Mag., 42(1951), 414, 1298
- [5] G.T. Taylor: J. Inst. Metals., 62(1938), 307
- [6] J.Grewen & G. Wassermann: Texture in Research &
   Practice, 1969,
- [7] R.E.Smallman: J.Inst. Metals., 84(1955-56),10
- [8] R.F.Braybrook & E.A.Calnan: J. Inst. Metals., 85(1956-57), 11.
- [9] R.E.Smallman & D.Green: Acta Met., 12(1964), 145
- [10] N.B.Brown: Trans. Met. Soc. AIME, 221(1961), 236
- [11] I.L.Dillamore & W.T.Roberts: Acta Met. 12(1964), 281
- [12] J.F.W.Bishop: J. Mech. Phys. Solids 3(1954), 130
- [13] E.A.Calnan: Acta Met. 2(1954), 865
- [14] B.Ramaswami, U.F.Kocks & B.Chalmers: Trans. Met. Soc. AIME 233(1965), 927
- [15] U.F.Kocks & T.J.Brown: Acta Met., 14(1966) 87
- [16] G.Y.Chin, W.F.Hosford & D.R.Mendorf: J. Inst. Met., 82(1953/54) 655
- [17] G.Y.Chin, W.L.Mammel & M.T, Dolan: Trans. Met. Soc.
  AIME, 240(1968)

- [18] G.Y.Chin, W.L.Mammel & M.T.Dolan: Trans. Met. Soc.
  AIME, 239(1967) 1854
- [19] G.Y.Chin & B.C.Wonsiewiez: Trans. Met. Soc. AIME, 240(1968),
- [20] G.E.Tucker: J. Inst. Met., 82(1953) 655
- [21] J.Hirsch, K.Lucke & M.Hatherly: Acta Metall., 36(1988), 2905
- [22] A.G.Grocker & J.S.Abell: Phil. Mag., 33(1976), 305
- [23] A.S.Malin & M.Hatherly: Metal Sci., 13(1979), 463
- [24] J.G.Sevillano, P.V.Houtte & E.Aernoudt: Prog. Meter. Sci., 25(1980),71
- [25] M.Hatherly & A.S.Malin: 18(1984),449
- [26] M.Hatherly: Strength of Metals & Alloys (ed.R.C.Gifkins, Pergamon, 1983), 1181
- [27] G.R.Canova, U.F.Kocks & M.G.Stont: Scripta Metall., 18(1984),437
- [28] I.L.Dillamore, J.G.Roberts & A.C.Bush: Metal Science, 13(1979),73
- [29] R.J.Clifton, et al: Scripta Metall., 18(1984),443
- [30] R.O.Williams: Trans. Met. Soc. AIME, 224(1962),129
- [31] P.A.Beck: Trans AIME, 191(1951),475
- [32] P.A.Beck: Acta Met., 1(1953)23
- [33] B.F.Peters: Met. Trans., 4(1973),757
- [34] B.F.Peters & D.C.Reid: Met. Trans., 4(1973)2859
- [35] I.L.Dillamore & H.Hatoh: Metal Sci., 8(1974),73
- [36] R.D.Doherty, et al: ICOTOM8, P563

- [37] K.Lucke & R.Rixen: Met. Trans. 1(1970),259
- [38] J.Hirsch & K.Lucke: Acta Metall., 33(1985),1927
- [39] K.Lucke, R.Rixen & M.Senna: Acta Metall., 24(1976), 103
- [40] Y.C.Liu: Trans. Amer. Inst. Min. Met. Eng., 209(1957),836
- [41] C.A. Verbraak: Acta Met., 8(1960)65
- [42] I.L.Dillamore & W.T.Roberts: Metall. Reviews 10(1965),271
- [43] P.A.Beck & H.Hu: Trans. AIME, 185(1949),185
- [44] M.L.Kronberg & F.H.Wilson: Trans. AIME, 185(1949),501
- [45] P.A.Beck & H.Hu: Trans. AIME, 194(1952),83
- [46] T.J.Koppenaal, M.N.Parthasarathi & P.A.Beck: Trans.
  AIME, 218(1960),98
- [47] R.Rixen, R.Musick, H.Goeker & K.Lucke: [22] in reference [9]
- [48] P.K.Koh & C.G.Dunn: Trans. AIME, 203(1955),401
- [49] P.K.Koh & C.G.Dunn: Trans. AIME, 206(1956),1017
- [50] H.Hu: Trans. AIME, 209(1957),1164
- [51] H.Hu: Trans. AMIE, 215(1959),320
- [52] W.C.Leslie: Trans AIME, 221(1961),752
- [53] C.G.Dunn: Acta Metall., 1(1953),163
- [54] W.G.Burgers & T.J.Tiedema: Acta Met., 1(1953),234
- [55] W.Bollmann: J. Inst. Metals, 87(1958),439
- [56] J.E.Bailey: Phil. Mag., 5(1960),833
- [57] I.L.Dillsmore & H.Katoh: Metal Science 8(1974),73
- [58] B.F.Peters: Met. Trans., 4(1973),757
- [59] B.F.Peters & D.C.Reid: Met. Trans., 4(1973),2851

- [60] I.L.Dillamore, C.J.E.Smith & T.W.Watson: Metal Sci.
  J., 1(1967),49
- [61] H.Takechi, H.Kato & S.Nagashima: Trans. Met. Soc. AIME, 242(1968),56
- [62] W.B.Hutchinson: International Metals Reviews, 29(1984),25
- [63] W.B.Hutchinson, at al: Texture in Research and
  Practice, ed. J. Grewen et al. P339 (1969)
  Berlin, Springer, Verlag
- [64] G.L.Ferran, R.D.Doherty & R.W.Cahn: Acta. Met., 19(1971),1019
- [65] H.Hu: Rrcovery & Recrystallization of Metals, ed.
  L.Himmel. P311,1963, New York
- [66] J.L.Walter & G.F.Koch: Acta Met., 11(1963),923

  I.L.Dillamore, et al: Proc.Roy.Soc. 329(A)(1972)405
- [67] G.I.Taylor: J.Inst.Metals 62(1938)307
- [68] P.R.Mould & P.Cotterill: J. Met. Sci., 2(1967),241
- [69] R.D.Doherty & J.W.Martin: Trans. Amer. Soc. Metals, 57(1964),874
- [70] P.R.Mould & J.M.Gray: Met. Trans., 3(1972),3121
- [71] J.T.Michalak & R.D.Schoone: Trans. Met. Soc. AIME, 242(1968),1149
- [72] E.Hornbogen & H.Kreye: in Ref.[33] 274
- [73] H.Ahlborn, E.Hornbogen & U.Koster: J. Met. Sci., 4(1969),944
- [74] H.Kreye & E.Hornbogen: ibid., 5(1970),89

- [75] G. Ibe & K. Lucke: "Recrystallization, Grain Growth & Textures" (ed. by H. Margolin) P. 434 1966. Metals

  Park, Ohio (Amer. Soc. Metals)
- [76] P.A.Beck & H.Hu: P393 of Ref.45
- [77] A.Merlini: Trans. Met. Soc. AIME, 206(1956),867
- [78] H.Hu: "Textures in Research & Practice" P200 (1969)

  Berlin, Springer-Verlag
- [79] W.H.Baldwin: Trans. Amer. Inst. Min. Met. Eng., 168(1946),591
- [80] S.T.Higgins: Metal Sci., 8(1974),143
- [81] M.Hillert: Acta Met., 13(1965),227
- [82] W.A.Backofen, I.R.Turner & D.H.Avery: Trans. ASM 57(1964), 980
- [83] G.E.Dieter: Mechanical Metallurgy, McGraw-Hill, New York, 1961 P55
- [84] A.Nadai & M.J.Manjoine: J. Appl. Mech., 77A(1941),84
- [85] D.S.Fields Jr. & W.A.Backofen: Trans. ASM 51(1959),946
- [86] C.Rossard: Rev. Met., 63(1966),225
- [87] E.W.Hart: Aeta Metall., 15(1967),351
- [88] J.D.Campbell: J. Mech. Phys. Sol: 15(1967),359
- [89] E.Orowan: Reports Progr. Physics, 12(1948-49),185
- [90] D.Oelschlagel & V. Weiss: Trans. ASM, 59(1966),143
- [91] R.Kot & V.Veiss: ibid, 60(1967),566
- [92] G.W.Greenwood & R.H.Johnson: Proc. Roy. Soc.,
  A283(1965),403
- [93] R.H.Johnson & E.C.Sykes: Nature, 209(1966),192
- [94] W.Edington: Met. Trans., 13A(1982),703

- [95] G.Rai & N.J.Grant: Metall. Trans., 6A(1975),385
- [96] M.L. Vaidya, K.L. Murty & J.E. Dorn: Acta Metall., 21(1973),1615
- [97] H.W.Hayden , R.C.Gibson, H.F.Merrick & J.H.Brophy:
  Trans. ASM, 60(1967),3
- [98] D.Lee & W.A.Backofen: ibid, 239(1967),1034
- [99] M.F.Ashby & R.A.Verrall: Acta Metall., 21(1973),149
- [100] M.Suery & B Baudelet: J. Mater. Sci., 10(1975),1028
- [101] R.H.Johnson: Metall. Rev., 15(1970),115
- [102] B.burton: Scr. Metall., 5(1971),669
- [103] J.H.Gittus: Trans. ASME, J. Eng. Mater. Tech., 7(1977),244
- [104] A.E.Geckinli & C.R.Barrett: Scr. Metall., 8(1974),115
- [105] F.A.Mohemed & T.G.Langdon: Phil. Mag., 32(1975),697
- [106] H.E.Cline & T.H.Alden: Trans. AIME, 239(1967),710
- [107] J.W.Edington, K.N.Melton & C.P.Cutler: Prog. Mater. Sci., 21(1976),61
- [108] D.H.Avery & W.A.Backofen: Trans. ASM, 58(1965),551
- [109] Idem: Acta Metall., 15(1967),469
- [110] C.M.Parker & O.D.Sherby: Trans. ASM, 60(1967),21
- [111] A.Ball & M.M.Hutchison: Metal Sci. J., 3(1969),1
- [112] D.L.Holt & W.A.Backofen: Trans. ASM, 59(1966),755
- [113] M.J.Stowell, J.L.Robertson & B.M.Watts: Metal Sci.
  J., 3(1969),41
- [114] R.Kossowsky & J.H.Bechtold: Trans. Met. Sco. AIME, 242(1968),716
- [115] H.W.Hayden & J.H.Brophy: ibid, 61(1968),542

- [116] D.Lee & W.A.Backofen: Acta Metall., 23(1975),117
- [117] F.A.Mohamed & T.G.Langdon: Acta Metall., 23(1975),117
- [118] H.W.Hayden & J.H.Brophy: Trans. ASM, 61(1968),542
- [119] R.C.Gifkins: Metall. Trans., 7A(1976),1225
- [120] T.G.Langdon & F.A.Mohamed: Scr. Metall., 11(1977),575
- [121] W.B.Morrison: ibid, 242(1968),2221
- [122] T.H.Alden: Acta metall., 15(1967),469
- [123] K.Matsuki, H.Morita, M.Yamada & Y.Murakami: Metal Sci., 11(1977),156
- [124] B.P.Kashyap. A.Arieli, A.K.Mukherjee: J.Mater. Sci., 20(1985),2661
- [125] W.Hatz, E.Ruedl & P.Shiller: ibid, 10(1975),2003
- [126] R.C.Gifkins: J. Mater. Sci., 13(1978),1926
- [127] B.P.Kashyap & G.S.Murty: ibid, 18(1983),2063
- [128] H.Haziri, R.Pearce, M.Henderson-Brown & K.F.Hake:
  Acta Metall., 28(1975),489
- [129] H.Haziri, R.Pearce, M.Henderson-Brown & K.F.Hake: J. Microsc., 97(1973),229
- [130] D.L.Holt: Trans. AIME, 242(1968),25
- [131] G.L.Dunlop & D.M.R.Taphin: J. Mater. Sci., 7(1972),87
- [132] L.C.A.Samuelsson, K.N.Melton & J.W.Edington: Acta Metall., 24(1976),1017
- [133] O.A.Kaibyshev, R.Z.Valiev & V.V.Astanin: Phys. Status. Solidi., 35a(1976),403

- [134] O.A.Kaibyshev, I.V.Kazachov & S.Y.A.Salikhov: Acta Metall., 26(1978),1887
- [135] A.Arieli & A.K.Mukherjee: Mater. Sci. Eng., 43(1980),47
- [136] C.M.Parker, R.H.Johnson & O.D.Sherby: Trans. AIME, 242(1968),2485
- [137] H.Haziri & R.Pearce: J. Inst. Metals, 98(1970),71
- [138] K.N.Melton, C.P.Cutler, J.S.Kallend & J.W.Edington:
  Acta Metall., 22(1974),165
- [139] C.P.Cutler. J.W.Edington, J.S.Kallend & K.N,Melton:
  Acta Metall., 22(1974),665
- [140] K.N.Melton & J.W.Edington: Scripta Metall., 8(1974),1141
- [141] K.Matsuki, Y.Uetani, M.Yamada & Y.Murakami: Met.Sci., 5(1976),235
- [142] R.Z.Valiev & O.A.Kaybyshev: Phys. Status Solidi., 44a(1977),477
- [143] A.K.Mukherjee: Met. Sci. Eng., 8(1971),83
- [144] K.N.Melton, C.P.Cutler & J.W.Edington: Scipta Metall., 9(1975),515
- [145] H.Naziri & R.Pearce: Scripta Metall., 3(1969),807
- [146] G.L Dunlop, J.D.Reid & D.M.R.Taplin: Met. Trans. 2(1971),2308
- [147] A.E.Geckinli & C.R.Barrett: J. Mater. Sci., 11(1976),510
- [148] U.F.Kocks: Metall. Trans., 1(1970),1121

- [149] I.L.Dillamore & W.T.Roberts: Metall. Rev., 10(1965),271
- [150] G.Y.Chin: Texture in Research & Practice, ed.

  G.Wassermann & J. Grewen, P51. Springer, Berlin, 1969
- [151] R.H.Bricknell & J.W.Edingon: Acta Metall., 27(1979),1303
- [152] K.A.Padmanabhan & K.Lucke: Z. Metallkde, 77(1986),765
- [153] H.Hu: Texture, 1(1974),233
- [154] T.R.Bieler, G.R.Goto, A.K.Mukherjee: J. of Meter. Sci., 25(1990),4125
- [155] C.P.Cutler, J.W.Edington, J.S.Kallend and K.N.Melton:

  Metal Sci. J., 5(1971),210
- [156] K.N.Melton, C.P.Cutler & J.W.Edington: Scripta Metall., 8(1974),1141
- [157] F.J.Humphreys: Acta Metall., 27(1979),1801
- [158] F.J.Humphreys: Acta Metall., 25(1977),1323
- [159] P.Herbst & J.Huber: Textures of Materials, ed.
  G.Gottstein & K.Lucke (Springer Verlag Berlin, 1978)
  P453
- [160] P.N.Kalu & F.J.Humphreys: Textures of Materials

  (Eighth Internntional Conference, Santa Fe, New

  Mexico) ed. J.S.Kallend & G.Gottstein, 1987, P511
- [161] D.Juul Jensen, N.Hansen & F.J.Humphreys: Eighth Internutional Conference on Textures of Materials, ed. J.S.Kallend & G.Gottstein, The Metallurgical Sceciety, 1987.P431

- [162] N.Hansen & D.Juul Jensen: Annealing Processes-Recovery, Recrystallization & Grain Growth. eds. N.Hansen et al., (Ris & National Laboratory, Roskilde, 1986), P337
- [163] R.Garvin-Salazar, M.Brabers & E.Aernoudt: Mat. Sci. & Eng., 26(1976),251
- [164] G.Bonissoni & M.Paganelli: Appl. Mat. Res., 4(1965),84
- [165] F.J.Humphreys & D.Juul Jensen: Annealing Processes-Recovery Recrystallization & Grain Growth, eds. N.Hansen et al., (Ris & National Laboratory, Roskilde, 1986) P93
- [166] N.Hansen & B.Bay: Acta Metall., 29(1981),65
- [167] N.Hansen & D.Juul Jensen: Met. Trans., 17A(1986),253

